

# Characterisation and Manipulation of Transition Metal Dichalcogenides *via* Atomic Force Microscopy



A THESIS PRESENTED

BY

KATIE O'NEILL

UNDER THE SUPERVISION OF

PROF. GEORG S. DUESBERG & PROF. JONATHAN N. COLEMAN

FOR THE DEGREE OF

DOCTOR OF PHILOSOPHY

IN THE SUBJECT OF

PHYSICS

TRINITY COLLEGE DUBLIN  
THE UNIVERSITY OF DUBLIN

MARCH 2022



©2021 – KATIE O'NEILL  
ALL RIGHTS RESERVED.

## Declaration

I declare that this thesis has not been submitted as an exercise for a degree at this or any other university and it is entirely my own work.

I agree to deposit this thesis in the University's open access institutional repository or allow the Library to do so on my behalf, subject to Irish Copyright Legislation and Trinity College Library conditions of use and acknowledgement.

I consent to the examiner retaining a copy of the thesis beyond the examining period, should they so wish (*EU GDPR May 2018*).

Elements of this work that have been carried out jointly with others or by collaborators have been duly acknowledged in the text wherever included.

---

Katie O'Neill  
BA *Mod.*

## Characterisation and Manipulation of Transition Metal Dichalcogenides *via* Atomic Force Microscopy

### ABSTRACT

Scanning probe microscopy (SPM) has revolutionised nanotechnology and allowed the study and manipulation of materials at the nanoscale, making it ideal for the study of solid-state physics and semiconductor technologies. Atomic force microscopy (AFM) and scanning probe lithography (SPL) can be used as a 'toolbox' for mechanical treatments of various surfaces including polymers, metals and semiconductors. In recent years, two-dimensional (2D) layered materials, such as graphene and transition metal dichalcogenides (TMDs), have been heavily studied due to their high potential for use in a wide range of future nanoelectronic devices. Some semiconducting TMDs, such as MoS<sub>2</sub>, are known to change their bandgap with decreasing layer thickness. Other TMDs, such as PtSe<sub>2</sub>, have been shown to develop a band gap, i.e. go from semi-metallic to semiconducting.

The first results chapter of this thesis details where one such 'tool', the technique of nanoshaving, where materials are selectively removed by an AFM tip, is employed to produce nanopatterns of self-assembled monolayers (SAMs) on 2D materials. The materials used are monolayers of TMDs, namely MoS<sub>2</sub> and WS<sub>2</sub> non-covalently functionalised with a perylene derivative, perylene diimide (PDI). The approach involves rastering an AFM probe across the surface at a controlled increased load in ambient conditions. Due to the strong bond between PDI SAM and TMD, it is found that loads in excess of 1  $\mu$ N are required to pattern the monolayer. Various pre-defined patterns including a grating pattern with feature sizes below 250 nm are demonstrated, showing the high precision of nanoshaving as an accurate and non-destructive lithographic technique for 2D materials. In addition, non-covalent co-functionalisation of MoS<sub>2</sub> is demonstrated using perylene-3,4,9,10-tetracarboxylic dianhydride (PTCDA) SAMs on previously nanoshaved areas. Work functions of the shaved heterostructures are also examined using Kelvin probe force microscopy, another SPM-based tool.

The second results chapter describes the use of SPL and SPM-based tools with the aim of producing a seamless, self-contacted device by way of suitable material, namely PtSe<sub>2</sub>. A technique for manipulating TMD layers is explored and developed *via* nanomachining using AFM, which is used to reduce and control the layer thickness of PtSe<sub>2</sub> in the form of thermally assisted converted (TAC) films and mechanically exfoliated (ME) flakes. AFM and SEM results reveal the nanomachining of TAC films to be quite difficult due to the roughness of the films post-selenisation when compared to exfoliated materials. Nevertheless nanomachining TAC films results in thinner, smoother films overall. Machining of pristine Pt channels allows more control over the quantity of nanomachining, and also quality. For comparison with TAC films, electrically contacted ME PtSe<sub>2</sub> flakes are nanomachined at loads of 0.8 – 2.7  $\mu\text{N}$ . Raman spectroscopy of the nanomachined area shows more defective/damage material in the remaining layers, which are more easily removed than pristine layers with successive passes of nanomachining at the same loads. This suggests a path for continuous monitoring of device performance with each layer removal down to the monolayer, starting with metallic multi-layers and thinning down to a semiconducting monolayer. This would enable the design of ‘self-contacted’ devices based on TMDs through the creation of a semiconducting channel *via* nanomachining with high mobility, low contact resistance and low power.

The research undertaken showed how AFM-based mechanical manipulation techniques, namely nanoshaving and nanomachining, can be used to examine and explore TMDs and TMD-based heterostructures, along with complementary spectroscopy techniques. In addition, this work has opened pathways to future studies on the capability of AFM as a toolbox for characterisation of 2D materials as well as SPL and 2D materials/heterostructures.

## List of Publications

1. **K. O'Neill**, R. Greig, R. Tilmann, L. Peters, C. P. Cullen, G. Cunningham, C. Bartlam, C. Ó Coileáin, N. McEvoy, & G. S. Duesberg. Patterning functionalised surfaces of 2D materials by nanoshaving.\* *Nanomanufacturing and Metrology*, accepted. (2021)  
\*BASIS FOR CHAPTER 4
2. D. Tyndall, S. Jaskaniec, B. Shortall, A. Roy, L. Gannon, **K. O'Neill**, M. P. Browne, J. Coelho, C. McGuinness, G. S. Duesberg, & V. Nicolosi. Post-Synthetic Treatment of Nickel-Iron Layered Double Hydroxides for the Optimum Catalysis of the Oxygen Evolution Reaction. *npj 2D Materials & Applications*, **5**, 73 (2021).
3. S. Bhattacharjee, E. Caruso, N. McEvoy, C. Ó Coileáin, **K. O'Neill**, L. Ansari, G. S. Duesberg, R. Nagle, K. Cherkaoui, F. Gity, & P. K. Hurley. Insights into Multilevel Resistive Switching in Monolayer MoS<sub>2</sub>. *ACS Applied Materials & Interfaces*, **12**, 5, 6022-6029 (2020).
4. P. V. Shvets, D. Caffrey, K. Fleischer, I. Shvets, **K. O'Neill**, G. S. Duesberg, A. N. Vinichenko, K. Yu. Maksimova & A. Yu. Goikhman. Suppression of the metal-insulator transition in magnetron sputtered Ti<sub>2</sub>O<sub>3</sub> films. *Thin Solid Films*, **694**, 137642 (2020).
5. E. Coleman, S. Monaghan, F. Gity, M. Schmidt, J. Connolly, J. Lin, L. Walsh, K. Cherkaoui, **K. O'Neill**, N. McEvoy, C. Ó Coileáin, D. Buckley, C. O'Dwyer, P. K. Hurley & G. S. Duesberg. Large Area Growth of MoS<sub>2</sub> By Chemical Vapour Deposition. *ECS Meeting Abstracts*, MA2018-02 708 (2018).
6. W. Kim, H. Kim, T. Hallam, N. McEvoy, R. Gatensby, H. C. Nerl, **K. O'Neill**, R. Siris, G.T. Kim & G. S. Duesberg. Field-Dependent Electrical and Thermal Transport in Polycrystalline WSe<sub>2</sub> *Adv. Mater. Interfaces*, **5**, 11, 1701161 (2018).

## List of Presentations

### ORAL

1. *Manipulation of Transition Metal Dichalcogenides: Nanomachining 2D PtSe<sub>2</sub> with AFM* – Third Year Talk, School of Physics, TCD, Ireland  
17th January 2020
2. *Manipulation of Transition Metal Dichalcogenides: Nanomachining 2D PtSe<sub>2</sub> with AFM* – Microscopy Society of Ireland (MSI) Symposium 2020, TBSI, TCD, Ireland  
8th-10th January 2020
3. *Manipulation of Transition Metal Dichalcogenides: Nanomachining 2D PtSe<sub>2</sub> with AFM* – #MapNan19 Symposium, nanoGe Fall Meeting19, Holiday Inn, Berlin, Germany  
3rd-8th November 2019
4. *Manipulation of Transition Metal Dichalcogenides: Nanomachining 2D PtSe<sub>2</sub> with AFM* – NanoApp Workshop, Universität des Bundeswehr, Munich, Germany  
17th - 18th July 2019
5. *Scratching the Way to Faster Computers* – SFI Thesis in 3 competition, TCD, Ireland  
29th September 2017

### POSTER

1. *Work function engineering by nanoshaving functionalised 2D materials* – Graphene 2021, Grenoble, France  
26th-29th October 2021
2. *Manipulation of Transition Metal Dichalcogenides: Nanomachining 2D PtSe<sub>2</sub> with AFM* – SFI Review of INVEST, Tyndall Institute, Cork, Ireland  
30th October 2019
3. *Manipulation of Transition Metal Dichalcogenides: Nanomachining 2D PtSe<sub>2</sub> with AFM* – Graphene 2019, Rome, Italy  
25th-28th June 2019
4. *Manipulation of Transition Metal Dichalcogenides: Nanomachining 2D PtSe<sub>2</sub> with AFM* – NanoApp Workshop, Universität des Bundeswehr, Munich, Germany  
19th-21st September 2018.



5. *Manipulation of Transition Metal Dichalcogenides: Nanomachining 2D PtSe<sub>2</sub> with AFM* – Graphene Week, San Sebastian, Spain  
10th-14th September 2018.
6. *Manipulation of Transition Metal Dichalcogenides: Nanomachining 2D PtSe<sub>2</sub> with AFM* – 32nd IWEPNM, Kirchberg, Tirol, Austria  
17th-24th March 2018.
7. *Atomic Force Microscopy Characterisation and Manipulation of 2D Transition Metal Dichalcogenides* – 9th Stuttgart Nanodays, Universität des Bundeswehr, Munich, Germany  
13th-15th September 2017.

# Acknowledgements

THEY SAY IT TAKES A VILLAGE TO RAISE A CHILD, but I have found it also takes a village to finish a PhD. There have been many people throughout without whom this PhD would not have been possible.

First and foremost, I would like to thank my supervisor, Prof. Georg Duesberg, for all his advice, support and encouragement to partake in scientific conferences and for allowing me the fantastic opportunity to work as part of the ASIN group.

I would also like to thank my co-supervisor, Prof. Jonathan Coleman, for allowing me carry out this research. I would like to acknowledge the financial support by the SFI under PI\_10/IN.1/I3030 and SFI/12/RC/2278 and the European Union under Graphene Flagship H2020 No. 785219. None of this work would have been possible without the help and encouragement of many people at Trinity College Dublin.

Firstly, it's been an honour and a pleasure to be a member of the ASIN group for the last number of years, effectively since my brief stint as a research assistant in 2015. A massive thanks to all members, past and present, for being so welcoming and supportive and for their time and patience in the training and assistance they provided on the many pieces of equipment needed to complete this research, especially John, Conor, Lianne, Graeme, Maria, Toby, Kay and Daniela.

I would like to especially thank Dr. Niall McEvoy for his constant support, guidance, knowledge, enthusiasm and endless patience throughout this research. I'm also very grateful to Dr. Cormac Ó Coileáin for his support, guidance, enthusiasm, not to mention his ever-expanding knowledge on just about anything and everything. I would like to thank Dr. Cian Bartlam of Universität des Bundeswehr for his support, encouragement and knowledge on PL, particularly during this last year.

Thanks to Dr. Lianne Peters, Dr. Emmet Sheerin, Dr. John McManus and Dr. Conor Cullen for their time in proofreading this report. Many thanks to all the collaborators both here in Ireland and abroad, especially the Duesberg group in Universität des Bundeswehr. In particular, I would like to thank Dr. Lianne Peters, Dr. Conor Cullen and Dr. Graeme Cunningham for their help with

regards CVD samples; Dr. Jason Kilpatrick and Adama Innovations Ltd. for the nanomachining training and tips; and Max Pechtl and Rahul Dangi of Universität des Bundeswehr for help with mechanical exfoliation and flake samples. Cheers as well to the my office peers, past and present, for always being there for the chats - Daragh, Oisín, Dan, Kuanysh, Ainur, and Sam. I would also like to extend thanks to the staff at CRANN, the AML and the School of Physics for all their help and assistance.

Finally, I would like to thank my family and friends for their love and endless support and patience, and without whom, I would not have been able to finish this thesis. Massive shoutout in particular to my past and current housemates; Tessa and Aoife for getting me through the first half of this PhD, and to Conor and Ella for seeing me through the second half (not to mention a global pandemic). To my fellow PhD amigos, Emmet and Simon, cheers for always being there for me, whether it was a 15 min coffee break or a two hour lunch. To Molly and John, thank you for letting me use your lovely gaf as a writing space. To my pals - Carla, Caoimhe, Ian, Liam, Alana, Sam and Pa, and the list goes on - thank you for always being there for the chats and laughs and of course pints.

A massive thanks in particular to my brother, Jack, whose training, particularly during lockdowns, kept me physically in shape when my brain wasn't, and finally to the Gers, for their never-ending love, support and encouragement.

# Contents

<b>1</b>	<b>INTRODUCTION</b>	<b>I</b>
1.1	Introduction . . . . .	1
1.2	Thesis Overview . . . . .	5
1.3	Statement of Collaboration . . . . .	6
<b>2</b>	<b>THEORY &amp; BACKGROUND</b>	<b>7</b>
2.1	Atomic Force Microscopy . . . . .	7
2.1.1	Contact (Static) Mode . . . . .	9
2.1.2	Tapping/Non-contact (Dynamic) Mode . . . . .	9
2.1.3	Lennard-Jones Potential . . . . .	10
2.1.4	Spring Constant Calibration . . . . .	13
2.1.5	Contact Mode Force Calibration (Lever Sensitivity) . . . . .	14
2.1.6	Conductive AFM (C-AFM/PF-TUNA) . . . . .	17
2.1.7	Kelvin Probe Force Microscopy (KPFM) . . . . .	20
2.1.8	Nanomachining & Nanoshaving . . . . .	24
2.2	Introduction to 2D Materials . . . . .	27
2.3	2D Material Fabrication and Synthesis . . . . .	32
2.4	Self-Assembled Monolayers (SAMs) . . . . .	34
2.5	Layer-by-layer thinning methods . . . . .	36
2.6	Device Fabrication . . . . .	40
2.6.1	Schottky vs. Ohmic Contacts . . . . .	42
2.6.2	Heterojunctions . . . . .	44
2.6.3	Contact Resistance & Interface Geometries . . . . .	45
2.7	Raman Spectroscopy . . . . .	47
2.7.1	Classical Raman Theory . . . . .	48
2.7.2	Raman of TMDs . . . . .	50
2.8	Photoluminescence . . . . .	52
<b>3</b>	<b>EXPERIMENTAL METHODS</b>	<b>55</b>
3.1	General Materials . . . . .	56
3.2	Material Synthesis . . . . .	56
3.2.1	Vapour Phase Deposition . . . . .	56
3.2.2	Metal Deposition . . . . .	57

3.2.3	Thermally Assisted Conversion (TAC)	58
3.2.4	Chemical Vapour Deposition (CVD)	59
3.2.5	Mechanical Exfoliation	61
3.3	Lithographic Techniques	63
3.3.1	Photo & Electron Beam Lithography	63
3.4	Microscopic Techniques	65
3.4.1	Atomic Force Microscopy (AFM)	65
3.4.2	Nanoshaving/Nanomachining	65
3.4.3	Kelvin Probe Force Microscopy (KPFM)	67
3.4.4	Conductive AFM	69
3.4.5	Scanning Electron Microscopy	70
3.5	Spectroscopic Techniques	71
3.5.1	Raman Spectroscopy	71
3.5.2	Photoluminescence	71
3.6	Electrical Characterisation	72
<b>4</b>	<b>PATTERNING 2D SURFACES BY NANOSHAVING</b>	<b>73</b>
4.1	Introduction	73
4.2	Experimental Methods	79
4.2.1	CVD of TMDs	79
4.2.2	Surface Functionalisation of TMDs by SAMs	79
4.2.3	AFM Characterisation & Manipulation	79
4.3	Results & Discussion	80
4.3.1	Nanoshaving Pristine MoS <sub>2</sub>	81
4.3.2	Nanoshaving PDI on MoS <sub>2</sub>	83
4.3.3	Further PL Analysis of Nanoshaved MoS <sub>2</sub> & PDI on MoS <sub>2</sub>	85
4.3.4	Patterning PDI on MoS <sub>2</sub> <i>via</i> Nanoshaving	88
4.3.5	Co-functionalisation of MoS <sub>2</sub>	89
4.3.6	Change in Work Functions with Nanoshaving & Functionalisation	92
4.3.7	Nanoshaving PDI on WS <sub>2</sub>	94
4.4	Conclusions	95
<b>5</b>	<b>NANOMACHINING PtSe<sub>2</sub></b>	<b>97</b>
5.1	Introduction	97
5.2	Experimental Methods	102
5.2.1	Thermally Assisted Conversion (TAC) Devices	102
5.2.2	Mechanically Exfoliated (ME) Devices	103
5.2.3	Characterisation & Manipulation	104
5.3	Results and Analysis	105
5.3.1	Nanomachining TAC PtSe <sub>2</sub>	105
5.3.2	Nanomachining Pt Pre-Selenisation	109

5.3.3	Nanomachining Mechanically Exfoliated PtSe <sub>2</sub> Flake Devices . . . . .	112
5.4	Conclusion . . . . .	121
6	CONCLUSIONS & FUTURE WORK	<b>123</b>
	APPENDIX A NANOSHAVING RAMAN SPECTRA	<b>127</b>
	REFERENCES	<b>152</b>

## List of Acronyms

<b>2D</b>	Two-dimensional
<b>AC</b>	Alternating current
<b>AFM</b>	Atomic force microscopy
<b>AM-KPFM</b>	Amplitude modulated Kelvin probe force microscopy
<b>BL</b>	Bilayer
<b>BP</b>	Black phosphorus
<b>C-AFM</b>	Conductive AFM
<b>CB</b>	Conduction band
<b>CBM</b>	Conduction band minimum
<b>CMOS</b>	Complementary metal-oxide-semiconductor
<b>CPD</b>	Contact potential difference
<b>CVD</b>	Chemical vapour deposition
<b>DC</b>	Direct current
<b>DFT</b>	Density functional theory
<b>DOS</b>	Density of states
<b>EBL</b>	Electron beam lithography
<b>FET</b>	Field effect transistor
<b>FM-KPFM</b>	Frequency modulated Kelvin probe force microscopy
<b>HOMO</b>	Highest occupied molecular orbital
<b>HOPG</b>	Highly oriented pyrolytic graphite
<b>IPA</b>	Isopropanol
<b>InvOLS</b>	Inverse optical lever sensitivity
<b>KPFM</b>	Kelvin probe force microscopy
<b>LED</b>	Light emitting diode
<b>LJ</b>	Lennard-Jones
<b>LPE</b>	Liquid phase exfoliation
<b>LUMO</b>	Lowest unoccupied molecular orbital
<b>MBE</b>	Molecular beam epitaxy
<b>ME</b>	Mechanical exfoliation/mechanically exfoliated
<b>MESFET</b>	Metal-semiconductor field effect transistor
<b>ML</b>	Monolayer
<b>MOSFET</b>	Metal-oxide field effect transistor
<b>NTMD</b>	Noble transition metal dichalcogenide
<b>PF-TUNA</b>	PeakForce tunneling AFM
<b>PL</b>	Photoluminescence
<b>PSPD</b>	Position-sensitive photodetector

<b>RMS</b>	Root mean square
<b>SC</b>	Semiconductor
<b>SEM</b>	Scanning electron microscopy
<b>SPM</b>	Scanning probe microscopy
<b>STM</b>	Scanning tunneling microscopy
<b>SiO<sub>2</sub>/Si</b>	300 nm silicon oxide on silicon
<b>TAC</b>	Thermally assisted conversion
<b>TMD</b>	Transition metal dichalcogenide
<b>UHV</b>	Ultra-high vacuum
<b>UVL</b>	Ultraviolet photolithography
<b>VB</b>	Valence band
<b>VBM</b>	Valence band maximum
<b>vdW</b>	van der Waals



# Listing of figures

1.1	Summary of Microscopy techniques . . . . .	3
2.1	Schematic of AFM in tapping mode . . . . .	8
2.2	Illustration of PeakForce tapping cycle . . . . .	11
2.3	Illustration of Lennard-Jones potential . . . . .	12
2.4	Illustrations of force curves and cantilever motion . . . . .	15
2.5	Schematics of PF-TUNA . . . . .	18
2.6	Schematic of parallel plate capacitor setup used by Lord Kelvin . . . . .	20
2.7	Schematics of nanomachining & nanoshaving . . . . .	25
2.8	Periodic Table with TMDs highlighted . . . . .	28
2.9	3D Schematics of TMD structures . . . . .	29
2.10	Electronic band structure of MoS <sub>2</sub> . . . . .	30
2.11	Electronic band structure of PtSe <sub>2</sub> . . . . .	31
2.12	Schematic of 2D material fabrication methods . . . . .	33
2.13	Functionalisation of 2D TMDs by SAMs . . . . .	35
2.14	C-AFM patterning of BP . . . . .	37
2.15	Selective chemical etching of MoS <sub>2</sub> . . . . .	37
2.16	Thinning of MoTe <sub>2</sub> <i>via</i> laser irradiation . . . . .	39
2.17	Diagram of MOSFET . . . . .	41
2.18	Schottky junctions for p and n-type semiconductors . . . . .	42
2.19	Heterojunction types . . . . .	44
2.20	Schematic of contact geometry on 2D materials . . . . .	46
2.21	Schematic of types of Raman scattering . . . . .	49
2.22	Raman active vibrational modes of TMDs . . . . .	51
2.23	Direct-gap exciton transitions of MoS <sub>2</sub> . . . . .	53
3.1	Photos of S & Se VPD furnaces . . . . .	57
3.2	Schematic of two-zone furnace for TMD synthesis . . . . .	60
3.3	Schematic of CVD synthesis & microreactor . . . . .	61
3.4	Photo of custom-built ME transfer apparatus . . . . .	62
3.5	Photos of maskless UV lithography IMP . . . . .	64

3.6	Photos of the Bruker Multimode 8 AFM . . . . .	66
3.7	KPFM calibration under different biases . . . . .	68
3.8	KPFM of nanomachined pristine MoS <sub>2</sub> & calibrated probe work functions . . . . .	69
3.9	Photograph of WITec Alpha 300R spectrometer . . . . .	71
4.1	Chemical structures of perylene derivatives . . . . .	75
4.2	Type-II band alignments for PTCDA/MoS <sub>2</sub> . . . . .	78
4.3	Nanoshaving of pristine MoS <sub>2</sub> flakes . . . . .	82
4.4	Nanoshaving PDI on MoS <sub>2</sub> . . . . .	83
4.5	Fitted PL spectra of nanoshaved MoS <sub>2</sub> & PDI on MoS <sub>2</sub> . . . . .	86
4.6	Nanoshaving grating pattern into PDI on MoS <sub>2</sub> . . . . .	88
4.7	KPFM of co-functionalised MoS <sub>2</sub> . . . . .	89
4.8	Raman & PL of co-functionalised MoS <sub>2</sub> . . . . .	91
4.9	KPFM work function ranges . . . . .	93
4.10	Nanoshaving PDI on WS <sub>2</sub> . . . . .	94
5.1	Summary of applications, properties & synthesis of PtSe <sub>2</sub> . . . . .	98
5.2	Schematic of PtSe <sub>2</sub> diode . . . . .	101
5.3	Schematic of furnace for TAC PtSe <sub>2</sub> . . . . .	103
5.4	AFM images of nanomachining PtSe <sub>2</sub> TAC films . . . . .	106
5.5	AFM images of nanomachining PtSe <sub>2</sub> EBL TAC devices . . . . .	107
5.6	AFM images of nanomachining PtSe <sub>2</sub> TAC devices . . . . .	108
5.7	AFM images of nanomachining Pt films before selenisation . . . . .	110
5.8	Topographical profiles of machined Pt films before selenisation . . . . .	111
5.9	AFM images of MBE-deposited Pt films pre & post selenisation . . . . .	111
5.10	AFM & Raman of ME PtSe <sub>2</sub> flakes . . . . .	114
5.11	Optical & AFM images of contacted ME PtSe <sub>2</sub> flakes <i>via</i> maskless UVL . . . . .	115
5.12	AFM images of contacted ME PtSe <sub>2</sub> flake post-machining (multiple passes) . . . . .	116
5.13	AFM line profiles of nanomachined ME PtSe <sub>2</sub> flake (multiple passes) . . . . .	117
5.14	Optical & AFM images of contacted ME PtSe <sub>2</sub> flake post-machining . . . . .	118
5.15	Contacted ME PtSe <sub>2</sub> flake post-machining (varying loads) . . . . .	120
5.16	AFM line profiles of nanomachined ME PtSe <sub>2</sub> flake (multiple passes) . . . . .	121
A.1	Nanoshaved MoS <sub>2</sub> Raman . . . . .	128
A.2	Nanoshaved PDI/MoS <sub>2</sub> Raman . . . . .	128
A.3	PDI Raman/PL signal . . . . .	129
A.4	Nanoshaved PDI/WS <sub>2</sub> Raman . . . . .	129

*For a research worker, the unforgotten moments of their life are those rare ones which come after years of plodding work, when the veil over nature's secret seems suddenly to lift, and when what was dark and chaotic appears in a clear and beautiful light and pattern.*

Gerty Cori, biochemist & Nobel Prize winner

# 1

## Introduction

### 1.1 INTRODUCTION

FROM THE EARLIEST TIMES, humans have been interested in the world of the small. From ancient Greek philosophers, such as Democritus - who proposed the concept of minute elements given the Greek word *atomos* meaning 'indivisible'<sup>1</sup> - to modern day particle physics, humans have been trying

to determine the building blocks of the universe. The question is, how do you visualise the world that is too small to see?

In 1967, anatomist and optical and electron microscopist, Savile Bradbury, noted the symbolic power of the microscope: 'Of all the instruments used by the scientist, the microscope is perhaps the one which most aptly symbolises this profession to the non-scientist.'<sup>2</sup> First coined in 1624 in Italy by the original Accademia Dei Lincei (which included Galileo),<sup>3</sup> the term 'microscope' itself is derived from the Latin *microscopium* - literally 'an instrument for viewing what is small.'<sup>4</sup> One of the earliest important works on microscopy was physicist Robert Hooke's (of Hooke's Law) *Micrographia* in 1665, containing large-scale finely detailed illustrations of specimens viewed under an optical microscope.<sup>5</sup>

For over 400 years, the optical microscope has primarily dominated the field. Nevertheless, microscopy has come a long way since the compound microscopes of the 17th century that Hooke used whereby two convex lenses produced a magnified image. As well as optical microscopy, other types of microscopy techniques based on electrons and atomic forces have come to the fore in the last century. Modern microscopy can be divided into three basic types: optical, electron (or ion) and scanning probe.

The optical microscope as we know it was developed in the mid-19th century. It uses visible light (wavelengths of  $\sim 380 - 700$  nm) and transparent lenses to view objects on the micrometer scale ( $10^{-6}$  m), making it ideal for red blood cells, human hair, etc. However, the fundamental limitations of light microscopy led to the development of the electron microscope in the 1931. Instead of light, electron microscopes use a beam of negatively charged particles (electrons) and electromagnetic or electrostatic lenses to view particles on the nanometer scale ( $10^{-9}$  m), e.g. atoms. It was not until some 50 years later that scanning probe microscopy was developed and from that the atomic force microscope (AFM) was born. AFM produces images by 'feeling' the surface with a very sharp needle-like probe, instead of using light, electrons or lenses. SPM has revolutionised nanotechnology

and allowed the study and manipulation of materials on the nanoscale, making it ideal for the study of solid-state physics and semiconductor technologies.

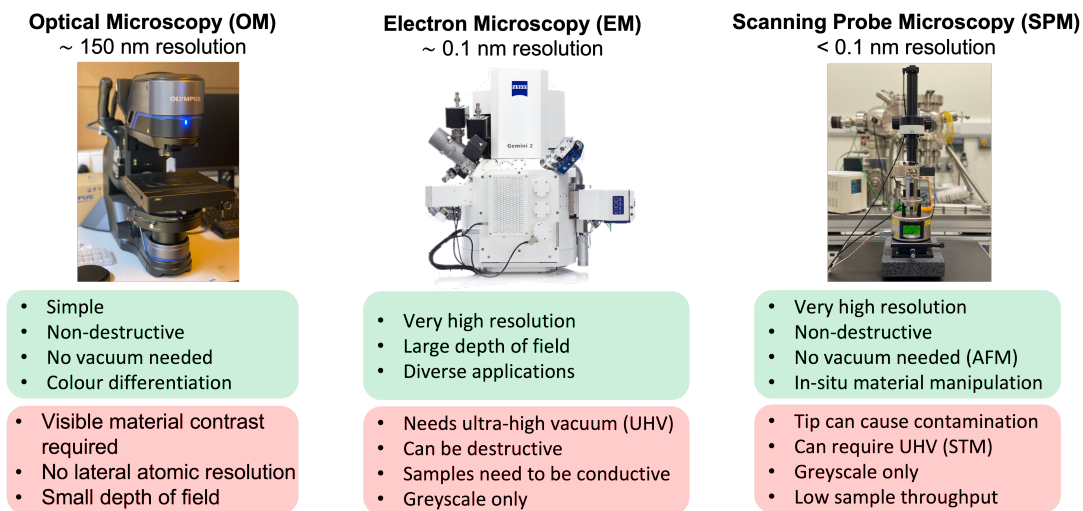


**Figure 1.1:** Summary of common pros and cons of the three main techniques of microscopy.

The use of semiconductor (SC) technology has exploded after the development of the transistor,<sup>6</sup> followed by the integrated circuit (IC) and the microchip. As a result, SCs have become ubiquitous in our everyday lives due to their highly economical miniaturisation and reliability, from transistors and diodes to microwave generators, solar cells and lasers, to name a few.

In 1965, Gordon Moore stated that the number of components per chip would approximately double every 2 years.<sup>7</sup> Since the 1970's, the semiconductor industry has been able to maintain Moore's law through the implementation of increasingly complex manufacturing of silicon (Si) based transistors. This is despite its end being prophesied numerous times through quantum effects resulting in leakage currents at the nanoscale. Conventional silicon-based transistors with a channel width as small as 3 nm have been demonstrated,<sup>8</sup> with a report on the possibility of even single atom transistors, representing the ultimate physical limit of Moore's law.<sup>9</sup> However, large scale integration

of these devices presents numerous challenges. Given current architectures, the devices would require major heat dissipation caused by contact resistance and leakage currents.

One way of potentially continuing Moore's Law is to utilise two dimensional (2D) materials, where there has been increasing interest in recent years thanks to modern advances in exfoliation techniques and particularly vapour-phase growth. These layered materials encompass semimetals, insulators, superconductors and semiconductors (SCs) such as graphene, hexagonal boron nitride (h-BN), transition metal dichalcogenides (TMDs), black phosphorus (BP), respectively, and many more. These materials all share a layered structure in common, whereby they can exist from a single layer of sub-nanometer thickness with significantly larger lateral sheet dimensions, to a bulk crystal consisting of countless layers held together by weak, out-of-plane Van der Waals (vdW) forces. Since Geim and Novoselov first isolated graphene from graphite in 2004,<sup>10</sup> 2D materials have been consistently in the research spotlight for applications in future nanoelectronics due to their fascinating optical<sup>11-15</sup>, electrical<sup>16-18</sup> and chemical/gas-sensing properties,<sup>19,20</sup> as well as ultrathin body and absence of dangling bonds.

As previously mentioned, SPM has revolutionised nanotechnology and allowed the study and manipulation of materials on the nanoscale, making it ideal for the study of 2D materials. However, for AFM in particular, little study has been carried on the use of its multitude of modes as a SPM-based 'toolbox' for the characterisation and manipulation of 2D materials. With AFM's ability to provide a whole host of tools *in-situ* to measure the mechanical and electrical properties as well as manipulation, 2D materials can be explored and characterised in a variety of ways that were previously not possible at the nanoscale.

## 1.2 THESIS OVERVIEW

The aim of this work is to take steps towards expanding the understanding of 2D materials and heterostructures through characterisation and manipulation using atomic force microscopy as the primary toolbox.

In **Chapter 1 Introduction**, the motivation behind this research is introduced and laid out, followed by an overview of this thesis. Thereafter is **Chapter 2 Theory & Background** involving the theoretical background of various AFM modes, i.e. the ‘tools’, including the manipulative techniques of nanoshaving and nanomachining, as well as the complementary Raman and photoluminescence spectroscopies. In addition, an overview of 2D materials, synthesis and device structures is discussed alongside a literature review of thinning processes.

Following the background and theory is **Chapter 3** pertaining to the experimental details for the synthesis and fabrication methods of the TMDs used in this work. In addition, characterisation techniques are introduced and discussed here.

The experimental results and discussion of this thesis are divided into two chapters. **Chapter 4 Patterning 2D Surfaces by Nanoshaving** explores the novel SPM technique of nanoshaving in patterning self-assembled monolayers (SAMs) on 2D group 6 TMDs. These organic-inorganic heterostructures are characterised further using Kelvin probe force microscopy (KPFM) and spectroscopic techniques such as Raman and photoluminescence (PL).

In **Chapter 5 Nanomachining PtSe<sub>2</sub>**\* the less studied group 10 TMD, PtSe<sub>2</sub>, is synthesised and fabricated into 2D devices. These layers are then removed mechanically by way of nanomachining, another SPM technique, with the aim of creating a semiconducting recess channel. These devices are characterised further with the complementary microscopic methods of conductive AFM, KPFM,

---

\*A small note on the structure of this thesis: to preserve the flow of the narrative, the results chapters, i.e. 4 and 5, are ordered chronologically in reverse.

SEM and Raman spectroscopy.

This thesis concludes with **Chapter 6** by reviewing the main findings, while subsequently suggesting directions for future investigations.

### 1.3 STATEMENT OF COLLABORATION

Some of the CVD MoS<sub>2</sub> samples shown in Chapter 4 were grown by Dr. Conor Cullen and Dr. Lianne Peters in Trinity College Dublin. CVD WS<sub>2</sub> samples were grown by Dr. Graeme Cunningham in Trinity College Dublin. Some mechanically exfoliated samples shown in Chapter 5 were prepared by Max Precht and Rahul Dangi in the Universität des Bundeswehr in Neubiberg, Germany.



*Young people, especially young women, often ask me for advice. Here it is, valeat quantum. Do not undertake a scientific career in quest of fame or money. There are easier and better ways to reach them. Undertake it only if nothing else will satisfy you; for nothing else is probably what you will receive. Your reward will be the widening of the horizon as you climb. And if you achieve that reward you will ask no other.*

Cecilia Payne-Gaposchkin, astronomer & astrophysicist

# 2

## Theory & Background

### 2.1 ATOMIC FORCE MICROSCOPY

The atomic force microscope (AFM) was developed in 1986 by Quate, Gerber and Binnig, the latter of whom was one half of the team behind the Nobel winning scanning tunneling microscope (STM), which revolutionised surface science. AFM is a very high resolution scanning technique and one of the foremost tools for imaging, measuring, and manipulating matter at the nanoscale. It is

primarily used to acquire spatially resolved data on surface features, such as the topography of the surface atomic layer, and also to measure forces at the surface. This information is gathered by exploring the specimen surface with a sharp tip (probe) on the end of a cantilever. Piezoelectric elements facilitate tiny but accurate and precise movements on electronic command and this enables high resolution scanning. Electric potentials of samples can also be measured using conducting cantilevers.<sup>21</sup>

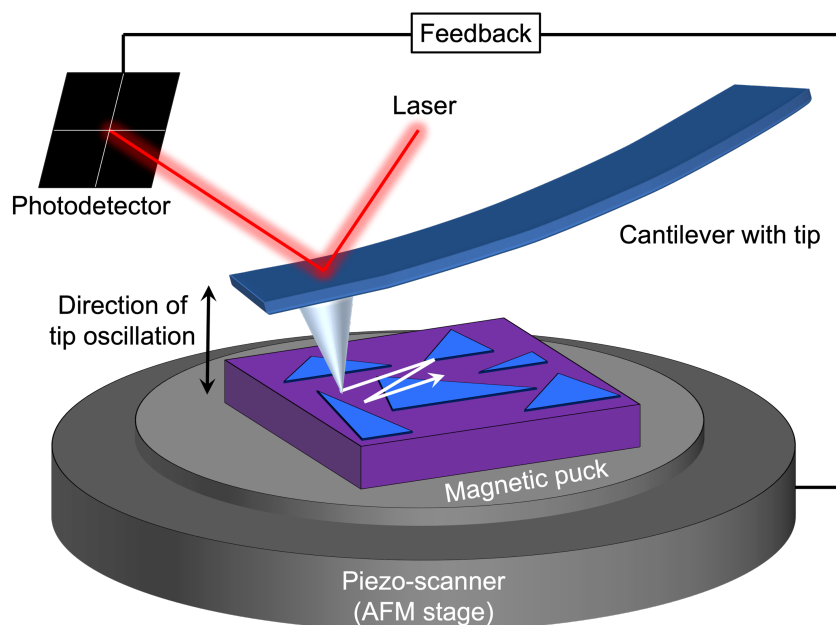


**Figure 2.1:** Schematic of typical atomic force microscope (AFM) in tapping mode. The white arrow indicates rastering direction.

The following sections contain content adapted from the Bruker MultiMode 8-HR User Guide.<sup>22</sup>

The key operating principle behind the AFM is detection of the bending of the cantilever spring in response to external forces. This is clearly shown in Figure 2.1. When the tip is brought within close proximity of a sample surface, forces between the tip and the sample lead to a deflection of the

cantilever. This deflection follows Hooke's Law (for small deflections) where the force applied to bend the cantilever is proportional to the cantilever displacement. By fixing the force/setpoint, the topographical data is measured by multiplying the measured displacement by the cantilever's spring constant. Typically, this deflection is measured using a laser spot reflected from the top surface of the cantilever into an array of photodiodes (see Figure 2.1).

Cantilevers are typically made of silicon or silicon nitride. The tip radius of curvature is on the order of nanometers and can be coated in a variety of materials depending on function, including diamond. In addition, tips can be terminated with other molecules to increase sharpness and sensitivity such as carbon nanotubes<sup>23</sup> and carbon monoxide.<sup>24</sup> The two primary modes of operation of an AFM are: contact and tapping/non-contact.

#### 2.1.1 CONTACT (STATIC) MODE

This is the simplest mode and consists of the cantilever tip being dragged across the surface of the sample. The contours of the surface are measured directly using the deflection of the cantilever. It is essential that it be done in contact where the overall force is repulsive, as the strong attractive forces at the surface can cause the tip to crash into the sample. The feedback mechanism keeps the force between the tip and the sample surface constant during scanning by maintaining a constant deflection. This method, however, is prone to noise due to the static signal and can damage delicate surfaces, as well as the tip itself, when the tip is dragged across.

#### 2.1.2 TAPPING/NON-CONTACT (DYNAMIC) MODE

An oscillating input signal is applied to make the cantilever (supporting a sharp tip at its end) vibrate up and down near its fundamental resonance frequency. This is done by a small piezoelectric transducer mounted in the AFM tip holder. The actual movement of the probe will depend on its

interaction with the specimen surface when brought into close proximity. Changes in the vibrating frequency due to tip-sample interaction are used to maintain a constant distance from the surface while rastering across the sample. Images are produced by imaging the force of the intermittent contact of the tip with the sample surface while maintaining a constant force or force gradient by a feedback loop. The short-range interaction is usually described by the empirical Lennard-Jones type interaction potential. This method of ‘tapping’ lessens the lateral forces and consequently the damage done to the surface and the tip, compared with contact mode. This makes tapping mode useful for examining delicate samples. However in ambient conditions, most samples develop a liquid meniscus layer. Because of this, keeping the probe tip close enough to the sample for short-range forces to become detectable while preventing the tip from sticking to the surface presents a major problem to dynamic mode operations.<sup>25</sup>

In this work, the primary mode used for topographical measurements was ScanAsyst-Air, a Bruker proprietary tapping mode. It utilises Bruker’s trademarked PeakForce Tapping mechanism (Fig. 2.2) which, though similar to standard tapping mode, decouples cantilever response from resonance dynamics, to automatically adjust all critical imaging parameters. This means it operates in a non-resonant mode, with gain and setpoint constantly being re-adjusted automatically through a sophisticated real-time feedback loop allowing optimal data to be collected whilst minimising noise. Force data between the tip and the surface is acquired at each pixel.

### 2.1.3 LENNARD-JONES POTENTIAL

Proposed by Sir John Edward Lennard-Jones in 1924, the Lennard-Jones (LJ) potential describes the potential energy of interaction between two non-bonding atoms or molecules based on their distance of separation.<sup>26</sup> It consists of two parts; a steep repulsive term representing Pauli repulsion, and a

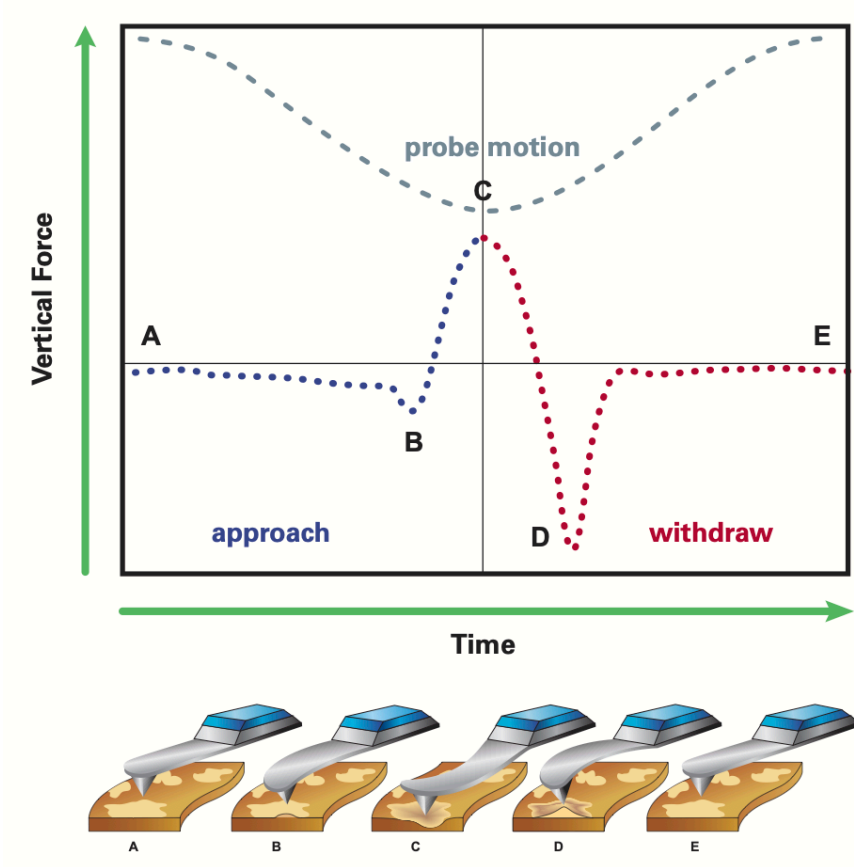


**Figure 2.2:** Illustration of PeakForce tapping cycle in ScanAsyst-Air mode with probe motion and vertical force as a function of time. Blue indicates tip approach while red indicates retract. Below the graph are illustrations of the AFM probe as it approaches and interacts with a sample surface. Each image corresponds to the labelled portion of the force curve.<sup>22</sup>

smoother attractive term, representing London dispersion forces, as illustrated in Fig. 2.3.

The LJ potential frequently forms the base of many computational models and is given by:

$$V(r) = 4\varepsilon \left[ \left( \frac{\sigma}{r} \right)^{12} - \left( \frac{\sigma}{r} \right)^6 \right] \quad (2.1)$$

which is sometimes expressed as:

$$V(r) = \frac{A}{r^{12}} - \frac{B}{r^6} \quad (2.2)$$

where  $V$  is the intermolecular potential between the two atoms or molecules,  $\varepsilon$  is the well depth and a measure of the strength of attraction between the two particles,  $\sigma$  is the distance at which the intermolecular potential between the two particles is zero,  $r$  is the distance of separation between both particles (as measured from their centers) and  $A = 4\varepsilon\sigma^{12}$ ,  $B = 4\varepsilon\sigma^6$ . In addition,  $\sigma$  gives the van der Waals radius, which is equal to half of the internuclear distance between the two particles. In the case of AFM, the two interacting particles represent the tip-sample interactions.<sup>27</sup>

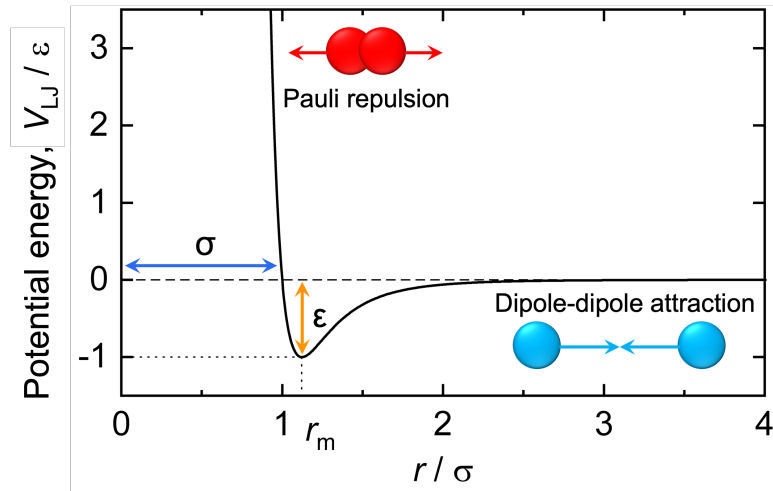


Figure 2.3: Illustration of Lennard-Jones potential which is used to describe the tip-sample interaction in AFM.

#### 2.1.4 SPRING CONSTANT CALIBRATION

The spring constant of the majority of AFM probes is calibrated *via* the thermal tune method. This was first proposed by Hutter and Bechhoefer who noted that the spring constant of a cantilever could be related to its thermal energy when the law of equipartition is applied to the fundamental mode of the cantilever, resulting in:<sup>28-30</sup>

$$\frac{1}{2}k_0\langle z_c^2 \rangle = \frac{1}{2}k_B T \quad (2.3)$$

where  $k$  is the spring constant of the cantilever,  $\langle z_c^2 \rangle$  is the mean square deflection of the cantilever's thermal motion,  $k_B$  is the Boltzmann constant and  $T$  is the absolute temperature. This equation assumes that the cantilever acts as a perfect simple harmonic oscillator. To compensate for the fact that cantilevers do not act like these, Butt and Jaschke added a small correction to Eqn. 2.3:<sup>31</sup>

$$k = \frac{0.971k_B T}{\langle z_c^2 \rangle} \quad (2.4)$$

Butt and Jaschke also recognised that the optical lever deflection detection scheme detects cantilever inclination rather than true displacement, resulting in an additional error.<sup>31</sup> This correction combined with an additional correction\* necessary if the cantilever is mounted at an angle  $\alpha$  off horizontal<sup>33</sup> (as is wont to happen in AFM) results in the final formula:<sup>34</sup>

$$k = \frac{0.817k_B T \cos^2 \alpha}{\langle z_c^{*2} \rangle} \quad (2.5)$$

where the asterisk in  $\langle z_c^{*2} \rangle$  designates the 'virtual' deflection measured by the optical lever.

The thermal vibrations of the mounted tip (once the laser is aligned and tip is lowered near the sample surface) are recorded by the photodetector, which has a finite bandwidth up to 2 MHz. The

---

\*These corrections assume a rectangular cantilever. Different corrections are needed when applied to v-shaped cantilevers, e.g. ScanAsyst-Air.<sup>32</sup>

original displacement time-series is Fourier transformed to segregate other broadband noise contributions from the narrowband thermal noise around resonance.<sup>22</sup> Using Eqn. 2.5 to calculate the spring constant, the software automatically fits the resonance peak in the filtered data with a Lorentzian distribution for use in air:<sup>22</sup>

$$A(\nu) = A_0 + \frac{C_1}{(\nu - \nu_0)^2 + C_2} \quad (2.6)$$

where  $A(\nu)$  is the amplitude as a function of frequency  $\nu$ ,  $A_0$  is the baseline amplitude,  $\nu_0$  is the centre frequency of the resonant peak,  $C_1$  and  $C_2$  are Lorentzian fit parameters. With the spring constant calibrated, typical tapping mode operation can be carried out using amplitude modulation detection with a lock-in amplifier.

#### 2.1.5 CONTACT MODE FORCE CALIBRATION (LEVER SENSITIVITY)

To calculate the contact force between the tip and sample during Contact AFM, it is imperative to calibrate the contact force on a hard sample surface, i.e. negligible surface deformation should occur with the cantilever deflecting while the probe pushes against the surface. The sample surface must also be clean as contamination can result in force dissipation instead of the cantilever bending. Most commercial AFMs use an optical method to detect the deflection of the cantilever, i.e. topography is measured from the photodetector voltage and the inverse optical lever sensitivity (InvOLS), whereas the force is the product of the displacement in nm and the spring constant.

As previously described, a laser spot reflects from the back side of the cantilever onto a position-sensitive photodetector (PSPD), which yields a signal corresponding to tip/surface interactions. The deflection sensitivity allows conversion from the raw photodiode signal (in volts) to the deflection of the cantilever (in nm), which must be calibrated before accurate deflection data



can be obtained. This sensitivity is equal to the inverse of the force curve slope while the cantilever is in contact with the hard sample surface.

If the sensitivity is calibrated on a material much stiffer than the cantilever, the inverse value of the AFM's optical lever sensitivity (InvOLS, nm/V) is measured, i.e. how many volts of deflection signal are produced by a given deflection of the cantilever tip. To calibrate, the deflection error (nm) is plotted against height, Z (nm) to give the force-versus-distance curves (force curves for brevity), which are a graphical representation of the deflection error compared to Z piezo position. Deflection error is a comparison to the separation between the probe tip and the sample surface.

A force plot is an observation of tip-sample interaction that provides information regarding the sample and tip. In SPM, by combining force curves at regularly spaced intervals across a sample, a force map of the sample's electronic properties, elastic modulus and chemical bonding strengths can be obtained.<sup>35</sup>

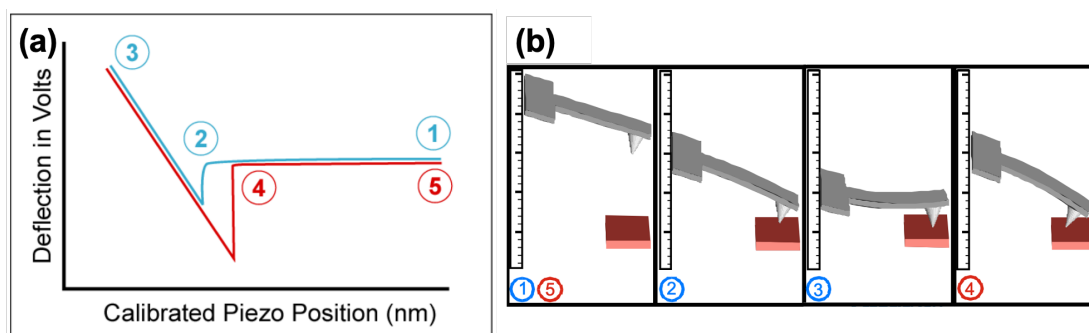


**Figure 2.4:** (a) The force curve represents the deflection signal for a complete extension-retraction cycle of the Z-piezo. (b) Illustrations of a cantilever probe as it approaches and interacts with a sample surface.<sup>22</sup> Each numbered image corresponds to the numbered portion of the force curve.

Probes with lower spring constants are very sensitive to attractive and repulsive forces. In Fig. 2.4, the force curve represents the typical deflection signal for a complete extension-retraction cycle of the Z piezo. The numbers on the graph highlight each stage, which correspond to the numbered

illustrations describing the cantilever motion. The horizontal axis plots the tip movement relative to the sample with the vertical axis plotting the cantilever deflection.

1. The piezo extends and the probe descends towards the sample surface. There is no contact between the tip and the sample surface yet.
2. Attractive forces near the sample surface pull the tip down, i.e. snaps into contact.
3. As the tip presses into the surface, the cantilever deflects upward.
4. The piezo retracts and the probe ascends until the retraction forces are in equilibrium with the surface forces. The cantilever relaxes downwards until it is no longer deflected. The piezo continues to retract and the probe ascends further. The cantilever bends downward as the surface attraction holds onto the tip.
5. As the piezo continues retracting the probe continues to ascend. With no further contact with the sample surface, the tip is now free of the sample, thus the cantilever is neither deflected upward or bent downward.

Using the slope of the force curve, we get:

$$InvOLS = \Delta D = \frac{\Delta z}{\Delta V} \Delta V \quad (2.7)$$

The inverse of the optical lever sensitivity (InvOLS) comes from requiring the slope of the hard contact region to be equal to 1, as on a hard surface (eg. sapphire), only the cantilever deforms during indentation ( $\Delta z = \Delta D$ , where  $z$  is the position of the piezo in the axial dimension and  $D$  is the deflection of the cantilever).<sup>36</sup> The drawback of this method is that InvOLS is dependent on a wide variety of factors including laser spot size/shape,<sup>37</sup> position/optical geometry,<sup>38</sup> cantilever length, backside reflectivity,<sup>39</sup> possible cantilever twist/rotation due to lateral forces,<sup>36</sup> etc. Typical InvOLS

values range from 1 – 100 nm/V.

#### 2.1.6 CONDUCTIVE AFM (C-AFM/PF-TUNA)

In conductive modes of AFM, a stationary (DC) voltage bias is applied between the tip and sample and the corresponding DC electric current flow is measured, from which the conductance of the sample can be mapped locally. In addition, at specific locations on the sample, the dependence of conductivity on the applied bias can be measured by performing DC voltage sweeps. The applied voltage can be modulated slowly, enabling the differential conductance  $\frac{dI}{dV}$  to be measured. With the Bruker Multimode 8, two modes of conductive AFM were used:

##### C-AFM

Conductive AFM (C-AFM) is suited to imaging samples spanning a wide range of conductivity. While scanning in contact mode, a linear amplifier with a range of 1 pA – 1  $\mu$ A senses the current passing through the sample. By maintaining a constant force between the tip and sample, topographic and current images are generated simultaneously, enabling the direct correlation of local topography with local electrical properties. However, the use of contact mode for topography has proven to be a major limiting factor, particularly for samples that require low imaging forces in either/both vertical or lateral directions, e.g. conductive polymers, loosely bound nanowires, etc.

##### PF-TUNA

Another conductive mode is PeakForce tunneling AFM (PF-TUNA), a Bruker proprietary mode combining PeakForce Tapping mode with a high-bandwidth, low-noise current amplifier. It is suitable for highly resistive samples as it can sense sub-pA tip/sample currents using a linear amplifier

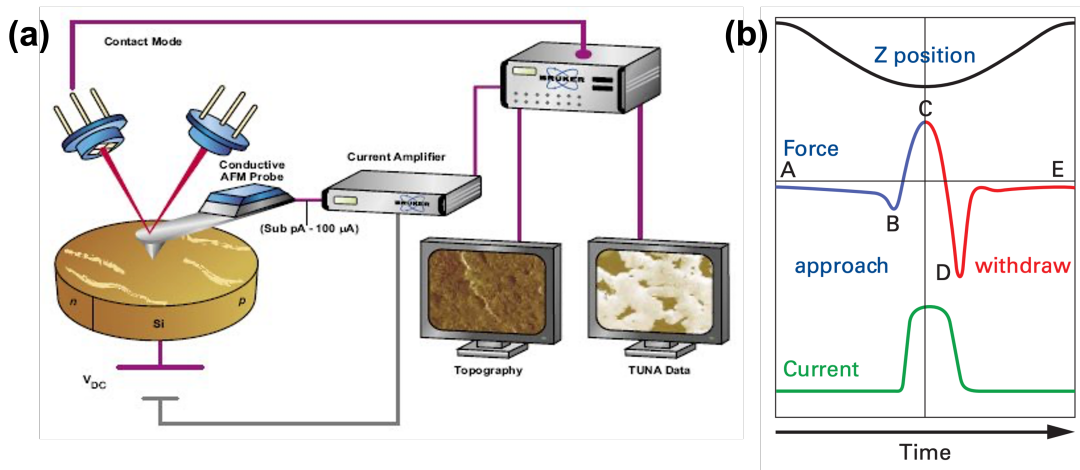


Figure 2.5: (a) Schematic of PF-TUNA setup.<sup>22</sup> (b) Diagram of a PF-TUNA tapping cycle with Z position, force and current as a function of time. Blue indicates tip approach while red indicates retract.<sup>22</sup>

with a range of 80 fA – 120 pA. PF-TUNA also largely eliminates lateral forces that tend to damage the tip and/or sample during imaging in contact mode and allows high resolution nanomechanical information to be collected simultaneously with correlated nanoelectrical properties. A force curve is performed at every pixel and the corresponding graph of Force vs. Time is referred to as the ‘heartbeat’ (see Fig. 2.5(b)). From the force curves, mechanical properties of the sample such as adhesion, modulus and deformation can be determined.

Fig. 2.5(b) illustrates what happens when the periodically modulated PeakForce Tapping probe interacts with the surface. The top line represents the Z-position of the cantilever base, as a function of time, as it goes through one period. The middle line represents the force measured by the probe during the approach (blue) and withdraw (red) of the tip to the sample. The bottom line (green) represents the detected current passing through the sample. Since the modulation frequency is about 1 kHz, the time from point A to point E is about 1 ms. From the current-time plot, such as in Fig. 2.5(b), PF-TUNA extracts 3 measurements:

- **Peak current** is the instantaneous current at point C, coinciding with the peak force. It is

usually the maximum current measured.

- **TUNA current** is the average current over a full tapping cycle, from point **A** to point **E**. It includes both the current measured while the tip is in contact and off surface.
- **Contact current** is the average current only when the tip is in contact with the surface, from the snap-on at point **B** to the pull-off at point **D**.

### 2.1.7 KELVIN PROBE FORCE MICROSCOPY (KPFM)

Kelvin probe force microscopy (KPFM), a relatively new technique, was first developed by Nonnenmacher *et al.*<sup>41</sup>, with the name originating from the macroscopic method developed by Lord Kelvin in 1898 using a vibrating parallel plate capacitor setup (see Fig. 2.6).<sup>40</sup> While employing the same principle, KPFM is based on non-contact AFM (nc-AFM) and the electrostatic interaction is continuously minimised between the scanning tip and the surface. KPFM is a powerful tool used to investigate the local surface potential and work function of samples with high spatial and energy resolution.<sup>42</sup> While similar to electrostatic force microscopy (EFM) which also measures electrostatic properties, these force contributions are compensated in KPFM by applying a DC-bias voltage between the tip and sample. The contact potential difference (CPD) is determined for metals and SCs, which is related to the sample's work function ( $\phi$ ), while for insulators, information about local charges and dipoles is obtained.

There are two main operating modes in KPFM:<sup>42</sup>

#### AMPLITUDE MODULATION (AM-KPFM)

Amplitude modulation KPFM (AM-KPFM) is a two-pass procedure where the surface topography is collected in a tapping mode on the first pass and the surface potential is measured on the second, in

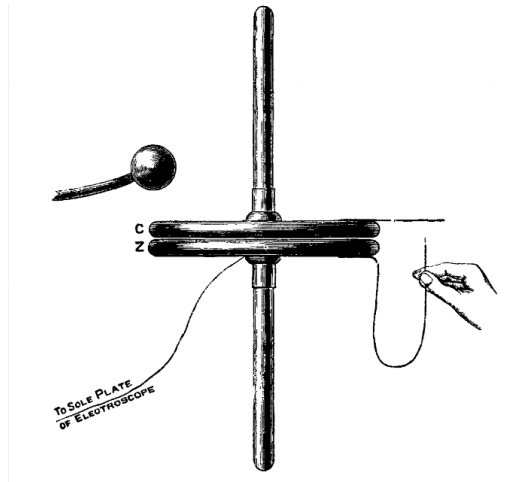


**Figure 2.6:** Schematic of vibrating parallel plate capacitor, consisting of copper and zinc plates, developed by Lord Kelvin in 1898 - the macroscopic method which modern Kelvin probe techniques are based on.<sup>40</sup>

a lift mode.<sup>†</sup> The amplitude of the cantilever oscillation at the AC-frequency  $\omega_{ac}$  is measured, which is proportional to and induced by the electrostatic force. If the tip and sample are at the same DC voltage, there is no force on the cantilever at  $\omega_{ac}$  and the cantilever amplitude will go to zero. Local surface potential is determined by adjusting the DC voltage on the tip  $V_{tip}$  or sample  $V_{sample}$  until the oscillation amplitude goes to zero and  $V_{tip}$  or  $V_{sample}$  is equal to the surface potential. The voltage bias applied  $V_{DC}$  is recorded to construct a voltage map of the surface.

The limiting factor in this mode are large AC voltages can potentially induce band-bending at the surface of SCs, leading to an inaccurate determination of  $\phi$ .<sup>43</sup>

### FREQUENCY MODULATION (FM-KPFM)

Frequency modulation (FM-KPFM) is a tapping mode single-pass technique and does not use a lift mode, in contrast to AM-KPFM. It has a higher spatial resolution than AM-KPFM but a lower signal-to-noise ratio. An AC voltage with amplitude  $V_{AC}$  and frequency  $f_{AC}$  (angular frequency  $\omega_{AC}$ ) superimposed on a DC voltage  $V_{DC}$  is applied between the tip and sample. In the case of AFM, the most significant contribution is due to the forces perpendicular to the sample surface ( $z$  direction). The resulting electrostatic force is given by:

$$F_d = -\frac{1}{2} \frac{\partial C}{\partial z} (\Delta V)^2 \quad (2.8)$$

where  $C$  is the capacitance and  $\Delta V$  is the total voltage:

$$\Delta V = V_{DC} - \frac{\Delta\phi}{e} + V_{AC} \sin(\omega_m t) \quad (2.9)$$

---

<sup>†</sup>A lift mode is defined as when the tip rasters at a set height above the surface, following the surface contours to maintain constant separation.

and  $\Delta\phi$  is the CPD between the probe and sample.

Combining these wxpressions, Eqn. 2.8 can be separated into three terms:

$$F_{cl} = -\frac{1}{2} \frac{\partial C}{\partial z} \left[ \left( V_{DC} - \frac{\Delta\phi}{e} \right)^2 \right] + \frac{\partial C}{\partial z} \left[ V_{DC} - \frac{\Delta\phi}{e} \right] V_{AC} \sin(\omega_m t) + \frac{1}{4} \frac{\partial C}{\partial z} V_{AC}^2 \cos(2\omega_m t) \quad (2.10)$$

The electric field gradient is given by:

$$\frac{\partial F_{cl}}{\partial z} = -\frac{1}{2} \frac{\partial^2 C}{\partial z^2} \left[ \left( V_{DC} - \frac{\Delta\phi}{e} \right)^2 \right] + \frac{\partial^2 C}{\partial z^2} \left[ V_{DC} - \frac{\Delta\phi}{e} \right] V_{AC} \sin(\omega_m t) + \frac{1}{4} \frac{\partial^2 C}{\partial z^2} V_{AC}^2 \cos(2\omega_m t) \quad (2.11)$$

The applied AC voltage modulates the force and force gradient at frequencies  $\omega_m$  and  $2\omega_m$ .

With regards modulating frequency, Hooke's Law states:

$$F = k(z - z_0) \quad (2.12)$$

Taking the derivative, gives:

$$\frac{\partial F}{\partial z} = k \quad (2.13)$$

Thus the force gradient and spring constant are seen to be equivalent. The electrostatic force shifts the resonant frequency of a cantilever with effective mass  $m^*$  as follows:

$$\omega'_0 = \sqrt{\frac{k - \frac{\partial F}{\partial z}}{m^*}} \quad (2.14)$$

The applied AC voltage modulates  $F_{cl}$  and  $\frac{\partial F_{cl}}{\partial z}$  according to Eqn. 2.11.

In this work, using a Bruker Multimode 8, the mode used was PeakForce KPFM (PF-KPFM), a two-pass mode that is a combination of Bruker's proprietary PeakForce tapping mode and standard FM-KPFM. It measures surface potential/work function using a lift mode (like in AM-KPFM)



variation of FM-KPFM imaging while simultaneously measuring nanomechanical properties. This translates as the first pass in a standard PeakForce tapping mode trace and retrace with the tip in the second pass lifted to a specified height above the sample surface (non-contact) and measuring the surface potential. The two measurements are interleaved - that is, they are each acquired one line at a time sequentially with both images displaying simultaneously in real time.

#### DETERMINATION OF WORK FUNCTION ( $\phi$ ) WITH SYSTEM BIAS

In this work, the bias was applied through the sample as the CPD images of higher potential translate to higher work function, and vice versa. For a sample-biased system, the work functions,  $\phi$ , can be determined from the CPD as such:<sup>42</sup>

$$\begin{aligned}
 CPD &= V_{probe} = \frac{\phi_{sample} - \phi_{probe}}{|e|} \\
 \phi_{probe} &= \phi_{Au} - |e|CPD_{Au} \\
 \phi_{sample} &= \phi_{probe} + |e|CPD_{sample}
 \end{aligned} \tag{2.15}$$

Where  $e$  is the elementary charge. Equivalently, a bias can be applied to the tip, resulting in the following equations for work functions:<sup>42</sup>

$$\begin{aligned}
 CPD &= V_{probe} = \frac{\phi_{probe} - \phi_{sample}}{|e|} \\
 \phi_{probe} &= \phi_{Au} + |e|CPD_{Au} \\
 \phi_{sample} &= \phi_{probe} - |e|CPD_{sample}
 \end{aligned} \tag{2.16}$$

Using a calibrated tip with a known  $\phi$ , the work function of the sample can be calculated from the CPD using Eqn. 2.15. However, as the work function is highly sensitive to surface cleanliness,<sup>41</sup> tip

shape and wear,<sup>44,45</sup> sample quality and grounding and experimental conditions, operation under ultra-high vacuum (UHV) conditions is preferred for absolute work function values.<sup>46</sup>

#### 2.1.1.8 NANOMACHINING & NANOSHAVING

Scanning probe microscopy (SPM) techniques have been widely employed in the fabrication of nanostructures on a wide variety of surfaces.<sup>47-49</sup> Though their throughput is limited, the nanoscale control and resolution afforded by scanning probe microscopy has prompted the development of a wide variety of scanning-probe-based patterning methods,<sup>47</sup> with some outperforming other lithography techniques. In addition, the ability of *in-situ* imaging gives AFM nanomachining and nanolithography an advantage over other lithographic techniques. Nanomachining uses the mechanical force exerted by the AFM tip to selectively remove material from a surface. It has been successfully applied to modify solid substrates, polymers and self-assembled monolayers.<sup>47</sup>

Like nanomachining, nanoshaving is when an SPM tip is used to scratch a surface mechanically or electrochemically with a required normal force.<sup>50</sup> It differs from nanomachining as its purpose is to selectively remove surfactants rather than penetrating the sample surface.<sup>51</sup> Mechanical displacement, or nanoshaving of self-assembled monolayers (SAMs) by an AFM probe is a relatively inexpensive technique, ideal for fundamental studies.<sup>50</sup> The ability of *in-situ* imaging also gives AFM nanomachining/shaving an advantage over other lithographic techniques.

Whether nanoshaving or nanomachining, the contact force between the tip and the sample can be calculated once the spring constant and the deflection sensitivity is known. Using the cantilever spring constant,  $k$ , and Hooke's Law, the contact force is defined as:

$$F_{tip} = kd \tag{2.17}$$

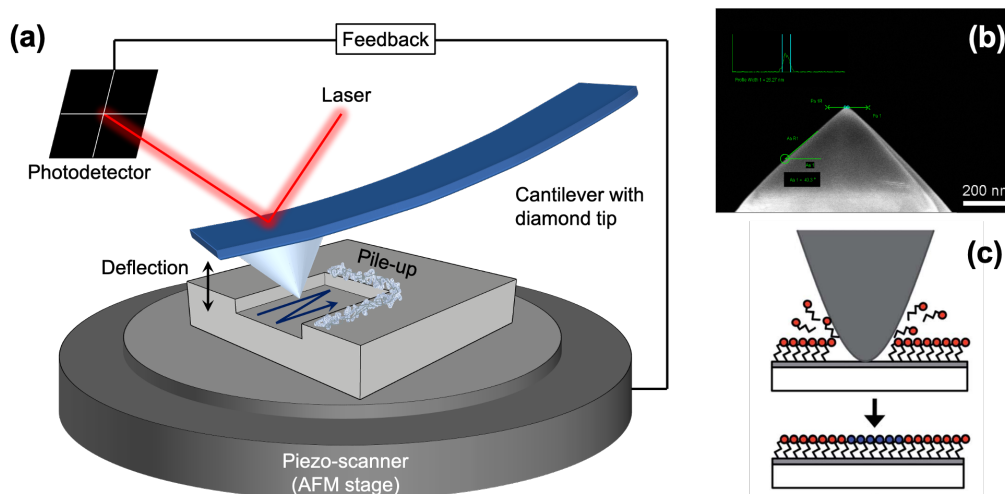


**Figure 2.7:** (a) Schematic of AFM setup for nanomachining/shaving. (b) SEM image of wide-angle diamond cone tip used in nanomachining & nanoshaving (courtesy of Adama Innovations Ltd.). (c) Schematic of typical nanoshaving process. The adsorbed SAM is selectively removed from the aluminium oxide surface.<sup>50</sup>

where  $d = \text{deflection sensitivity (nm/V)} \times \text{deflection setpoint (V)}$ .

Despite being highly researched materials for a wide range of applications, to date, there has been little exploration of the nanopatterning of SAMs on 2D materials using AFM. These versatile material removal applications of AFM make it an excellent candidate for investigating noncovalently functionalised 2D systems and offer advantages over established techniques such as bottom-up approaches and focused ion beam (FIB) milling.<sup>52</sup>

The stability of the tip can be the limiting factor in creating reproducible patterns as tips are prone to deformation and contamination from debris of removed materials. A solution to the problem for this study was to use wear-resistant diamond tips with broad cone angles (see Fig. 2.7(b), courtesy of Adama Innovations Ltd.), the contact size can be well characterised and stays constant during repeated patterning.

The mechanical nature of the nanomachining/shaving process is the root of its most significant limitations. The parameters must be carefully tuned to ensure controllable and reducible material

removal or thinning. In the case of nanoshaving, the SAM adsorbates (resist) should be selectively removed without substantially damaging the underlying 2D material. Different factors such as sample material, tip speed, applied force, tip angle, sliding direction, humidity and sample orientation affect the mechanism by which the material is removed, as well as the quality and quantity of removal.<sup>53</sup> Furthermore, AFM-based mechanical nanomachining/shaving has the disadvantage of ridge formation or the accumulation, so-called 'pile-up', of materials around the features.<sup>54</sup>

## 2.2 INTRODUCTION TO 2D MATERIALS

Graphene initially sparked huge interest for 2D materials to be used for logic electronic applications. However, graphene's lack of band gap has meant that it is very difficult to implement in logic devices, particularly field effect transistors (FETs), despite its other extraordinary properties.<sup>11,55</sup> TMDs are a class of layered materials with the general formula of  $\text{MX}_2$ , where M is a transition metal (eg. Mo, W, Pt) and X is a chalcogen (eg. S, Se, Te). Considerable interest has developed in the most popular TMDs (group VI), where  $\text{MoS}_2$  in particular is expected to substitute silicon for certain applications in the electronics industry.<sup>56-59</sup> Research into the dichalcogenides of Mo and W in particular has exploded, due to their excellent physical properties such as thickness-dependent semiconducting/metallic behaviours,<sup>11</sup> tuneable band gaps,<sup>60</sup>  $\sim 250 \text{ cm}^2\text{V}^{-1}\text{s}^{-1}$  carrier mobility at RT<sup>11</sup> and outstanding on/off ratio in FETs ( $\sim 10^8$ ).<sup>61</sup> At present, there are over 40 TMDs known.<sup>62</sup> The electrical properties of 2D TMDs have been shown to be dramatically modulated by thickness, structural phase transitions, strain-engineering and heterostacking. Also, by changing the chalcogen species, the electronic structure is affected more profoundly than the substitution of metal atoms. However a trend can still be observed whereby the  $d$  bands broaden with increasing atomic number of the chalcogen, resulting in a decrease in band gap. For example, the band gaps of  $\text{MoS}_2 > \text{MoSe}_2 > \text{MoTe}_2$ , from 1.3 to 1.0 eV respectively.<sup>63</sup>

In TMDs, each metal atom is covalently bound to 6 chalcogen atoms (six-fold coordinated) and each chalcogen is covalently bound to 3 metal atoms (three-fold coordinated) in either a trigonal prismatic, octahedral or distorted octahedral configuration. These then form monolayer structures referred to as 2H, 1T and 1T' respectively,<sup>63</sup> which are held together by weak van der Waals forces.<sup>11,16</sup> Monolayer (ML)  $\text{MoS}_2$  forms a stable 2D trigonal prismatic 2H structure.<sup>64</sup> This lattice configuration results in a  $D_{6h}$  point-group symmetry with three atoms in a unit cell, which can be seen in Fig. 2.9. Group VI

**Periodic Table of the Elements**

1 IA 1A	2 IIA 2A											13 IIIA 3A	14 IVA 4A	15 VA 5A	16 VIA 6A	17 VIIA 7A	18 VIIIA 8A												
1 H Hydrogen 1.008	2 He Helium 4.003											5 B Boron 10.811	6 C Carbon 12.011	7 N Nitrogen 14.007	8 O Oxygen 15.999	9 F Fluorine 18.998	10 Ne Neon 20.180												
3 Li Lithium 6.941	4 Be Beryllium 9.012											11 Na Sodium 22.990	12 Mg Magnesium 24.305											13 Al Aluminum 26.982	14 Si Silicon 28.086	15 P Phosphorus 30.974	16 S Sulfur 32.06	17 Cl Chlorine 35.453	18 Ar Argon 39.948
19 K Potassium 39.098	20 Ca Calcium 40.078	21 Sc Scandium 44.956	22 Ti Titanium 47.88	23 V Vanadium 50.942	24 Cr Chromium 51.996	25 Mn Manganese 54.938	26 Fe Iron 55.845	27 Co Cobalt 58.933	28 Ni Nickel 58.693	29 Cu Copper 63.546	30 Zn Zinc 65.39	31 Ga Gallium 69.723	32 Ge Germanium 72.61	33 As Arsenic 74.922	34 Se Selenium 78.96	35 Br Bromine 79.904	36 Kr Krypton 83.80												
37 Rb Rubidium 84.468	38 Sr Strontium 87.62	39 Y Yttrium 88.906	40 Zr Zirconium 91.224	41 Nb Niobium 92.906	42 Mo Molybdenum 95.94	43 Tc Technetium 98.907	44 Ru Ruthenium 101.07	45 Rh Rhodium 102.905	46 Pd Palladium 106.42	47 Ag Silver 107.868	48 Cd Cadmium 112.411	49 In Indium 114.818	50 Sn Tin 118.71	51 Sb Antimony 121.760	52 Te Tellurium 127.6	53 I Iodine 126.904	54 Xe Xenon 131.29												
55 Cs Cesium 132.905	56 Ba Barium 137.327	57-71 Lanthanide Series La Ce Pr Nd Pm Sm Eu Gd Tb Dy Ho Er Tm Yb Lu	72 Hf Hafnium 178.49	73 Ta Tantalum 180.948	74 W Tungsten 183.85	75 Re Rhenium 186.207	76 Os Osmium 190.23	77 Ir Iridium 192.22	78 Pt Platinum 195.08	79 Au Gold 196.967	80 Hg Mercury 200.59	81 Tl Thallium 204.383	82 Pb Lead 207.2	83 Bi Bismuth 208.980	84 Po Polonium [209]	85 At Astatine 209	86 Rn Radon 222.018												
87 Fr Francium 223.028	88 Ra Radium 226.025	89-103 Actinide Series Ac Th Pa U Np Pu Am Cm Bk Cf Es Fm Md No Lr	104 Rf Rutherfordium [261]	105 Db Dubnium [262]	106 Sg Seaborgium [266]	107 Bh Bohrium [264]	108 Hs Hassium [265]	109 Mt Meitnerium [268]	110 Ds Darmstadtium [269]	111 Rg Roentgenium [272]	112 Cn Copernicium [277]	113 Nh Nihonium [278]	114 Fl Flerovium [285]	115 Uup Ununpentium [286]	116 Lv Livermorium [293]	117 Uus Ununseptium [294]	118 Uuo Ununoctium [294]												

**Figure 2.8:** The periodic table of elements with transition metals (TM) and chalcogens (C) for layered TMDs highlighted. Elements outlined in red are the TMDs studied in this work.

TMDs tend to be most stable in the 2H phase, whereas those with a group X TM centre are more stable in the 1T octahedral configuration.<sup>65</sup> The 2H-phase TMDs tend to be semiconducting while many of the TMDs in the 1T phase tend to be metallic or semimetallic in the bulk.

While bulk MoS<sub>2</sub> and WS<sub>2</sub> in the 2H phase are indirect bandgap SCs, the MLs of these materials show direct and wide bandgaps.<sup>16</sup> In the bulk, MoS<sub>2</sub> and WS<sub>2</sub> have a bandgap of 1.2 and 1.3 eV, and these become direct bandgaps in the ML of 1.8 and 2.1 eV, respectively.<sup>66–69</sup>

Fig. 2.10 shows the calculated electronic bandstructure of 2H-MoS<sub>2</sub>. The indirect bandgap in bulk MoS<sub>2</sub> (Fig. 2.10(a)) results in the direct excitonic transitions occurring at high energies at the K point. With reduced layer thickness, the indirect bandgap becomes larger, while the direct excitonic transition barely changes. For ML MoS<sub>2</sub> in Fig. 2.10(d), it becomes a direct bandgap semiconductor. This dramatic change of electronic structure in ML MoS<sub>2</sub> can explain the observed jump in ML photoluminescence efficiency.<sup>66</sup>

Like MoS<sub>2</sub>, ML WS<sub>2</sub> also forms a stable trigonal prismatic 2H structure, resulting in a D<sub>6h</sub> point-group symmetry.<sup>70</sup> Similarly, in the ML, the conduction band minimum (CBM) and the

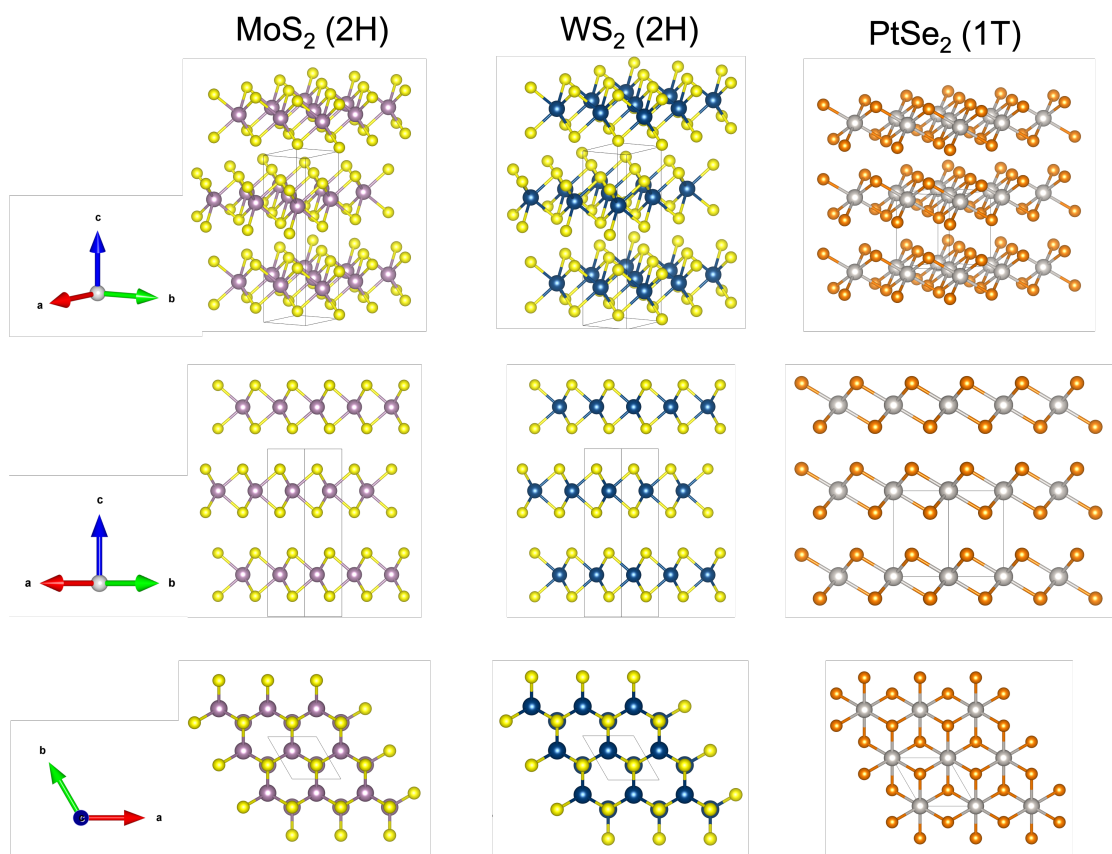


**Figure 2.9:** Three-dimensional schematic representation of the layered structures studied in this thesis of 2H-MoS<sub>2</sub>, 2H-WS<sub>2</sub> and 1T-PtSe<sub>2</sub> (1T) along with their associated stacking configurations and unit cells. The crystallographic directions are indicated. The metal atoms, Mo, W and Pt, are shown in lilac, navy and silver respectively, with chalcogens S as yellow and Se as orange.

valence band maximum (VBM) are located at the K point. When the layer number increases, the VBM shifts towards the  $\Gamma$  point while the CBM moves to between the K and  $\Gamma$  point.<sup>71</sup>

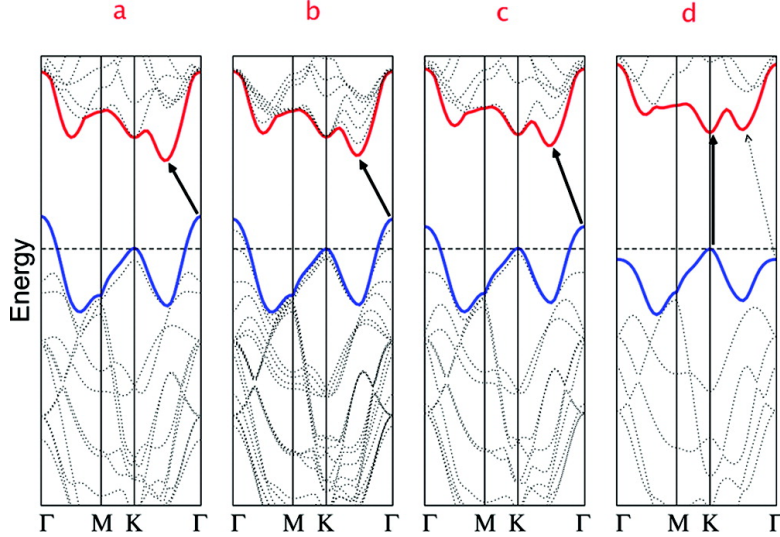


**Figure 2.10:** Calculated electronic band structures of (a) bulk MoS<sub>2</sub>, (b) quadrilayer MoS<sub>2</sub>, (c) bilayer MoS<sub>2</sub>, and (d) monolayer MoS<sub>2</sub>.<sup>66</sup> The solid arrows indicate the lowest energy transitions.

A layered material less studied than group 6 TMDs is PtSe<sub>2</sub>, which has been shown to develop a band gap (i.e. go from semi-metallic in the bulk phase to semiconducting in a single layer) with decreasing thickness of films.<sup>72,73</sup> Unlike the more commonly examined Mo or W dichalcogenides, PtSe<sub>2</sub> differs in crystal (Fig. 2.9) and band structure (Fig. 2.11). ML PtSe<sub>2</sub> forms a dynamically stable 2D octahedral 1T structure, more commonly known as the CdI<sub>2</sub> crystal group, which also comprises of other TMDs such as HfS<sub>2</sub> and SnS<sub>2</sub>.<sup>74,75</sup> This CdI<sub>2</sub> lattice type configuration of PtSe<sub>2</sub> has a  $D_{3d}$  point-group symmetry with three atoms in a unit cell. The ML and bilayer (BL) have been reported as having indirect band gaps of 1.2 – 1.6 eV and  $\sim$  0.8 eV, respectively.<sup>75-78</sup> While ML and BL 1T-PtSe<sub>2</sub> are indirect SCs, bulk and few layer 1T-PtSe<sub>2</sub> are semi-metallic in nature, making it a very interesting candidate for the possibility of ‘self-contacting’ FETs. Zhao *et al.* reported that few-layer PtSe<sub>2</sub> FETs exhibit high electron mobility at room temperature (RT) ( $\sim$  210 cm<sup>2</sup>V<sup>-1</sup>s<sup>-1</sup>)



on SiO<sub>2</sub>/Si substrate.<sup>79</sup> Nevertheless calculations predict significantly higher mobilities of  $\sim 4000$  cm<sup>2</sup>V<sup>-1</sup>s<sup>-1</sup> for PtSe<sub>2</sub> at RT.<sup>78</sup>

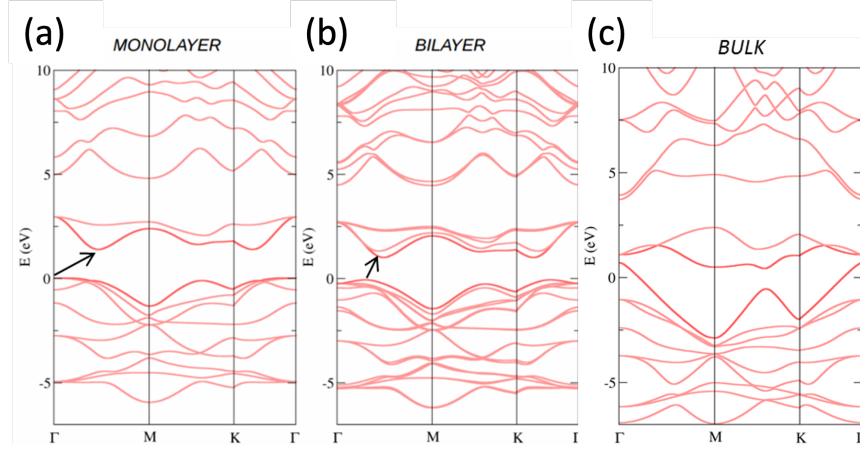


**Figure 2.11:** Calculated electronic band structure curves of (a) monolayer PtSe<sub>2</sub>, (b) bilayer PtSe<sub>2</sub> and (c) bulk PtSe<sub>2</sub>.<sup>76</sup> The arrows indicate the lowest energy transitions.

ML PtSe<sub>2</sub> is relatively robust in nature as its structure changes negligibly under biaxial tensile deformation,<sup>75</sup> making it a suitable candidate for nanomachining. However, it exhibits an extraordinarily strong interlayer interaction, which is significantly stronger than other TMDs (e.g. MoSe<sub>2</sub>, WSe<sub>2</sub>), presenting a challenge in its use.<sup>80</sup> This is due to it being rich with *d* electrons (eg. Group 10), which are prone to *d*<sup>2</sup>*sp*<sup>3</sup> hybridisation, forming the 1T phase.<sup>62,81</sup> Other TMDs, like MoS<sub>2</sub> and WS<sub>2</sub>, tend to form *d*<sup>4</sup>*sp* hybridisation, resulting in the 2H-phase. The intralayer hybridization between the *d* band of the transition metal and the *p*<sub>z</sub> band of the chalcogen atom in TMDs is weak in *d*<sup>2</sup>*sp*<sup>3</sup> but strong in the *d*<sup>4</sup>*sp* configuration. The relatively weak hybridisation of *d*<sup>2</sup>*sp*<sup>3</sup> results in stronger coupling between the two *p*<sub>z</sub> bands of two intermolecular Se atoms, in the case of PtSe<sub>2</sub>. This then leads to the extraordinarily strong interlayer interactions with nearly isotropic in-plane and out-of-plane mechanical interlayer coupling.<sup>81</sup>

### 2.3 2D MATERIAL FABRICATION AND SYNTHESIS

There are several commonly used methods for fabricating and synthesising 2D materials, each with associated advantages and disadvantages depending on the intended application, which are summarised in Fig. 2.12. These techniques can be generally categorised into three main classifications: mechanical exfoliation (ME), liquid phase exfoliation (LPE) and chemical vapour deposition (CVD).

Most pristine ML TMDs were initially achieved *via* mechanical exfoliation (ME), inspired by Novoselov and Geim's success with graphene.<sup>10,82</sup> A relatively simple and straight-forward technique, ME uses adhesive forces through Scotch tape to peel highly crystalline weakly-bonded vdW layers apart repeatedly.<sup>83,84</sup> Through this method, high-quality, pristine and macroscopic flakes of 2D materials can be produced, which are ideal for fundamental studies exploring properties. However, the disadvantages to this method are its low, unreliable throughput and tedious nature, particularly if the layered material has quite strong interlayer attraction. ME is completely inapplicable for production on an industrial scale. Nonetheless, it is invaluable in allowing new ideas and concepts for 2D materials to be explored.

On the opposite end of the scalability spectrum there is liquid phase exfoliation (LPE). As the name would suggest, this exfoliation method involves dispersing the bulk material in a liquid, primarily through sonication or shear mixing with an appropriate solvent.<sup>86-89</sup> Through either method, large amounts of few-layer sheets of varying size and thickness can be produced. These few-layer flake dispersions are very suitable for production on an industrial scale, particularly for printable inks<sup>90</sup> and composites.<sup>91</sup> Nevertheless, due to the large distribution in size and thickness, 2D materials made in this fashion are not suitable for high-quality electronic applications. In addition, problems can emerge due to re-aggregation of MLs upon drying and increased contact resistance between the flakes.

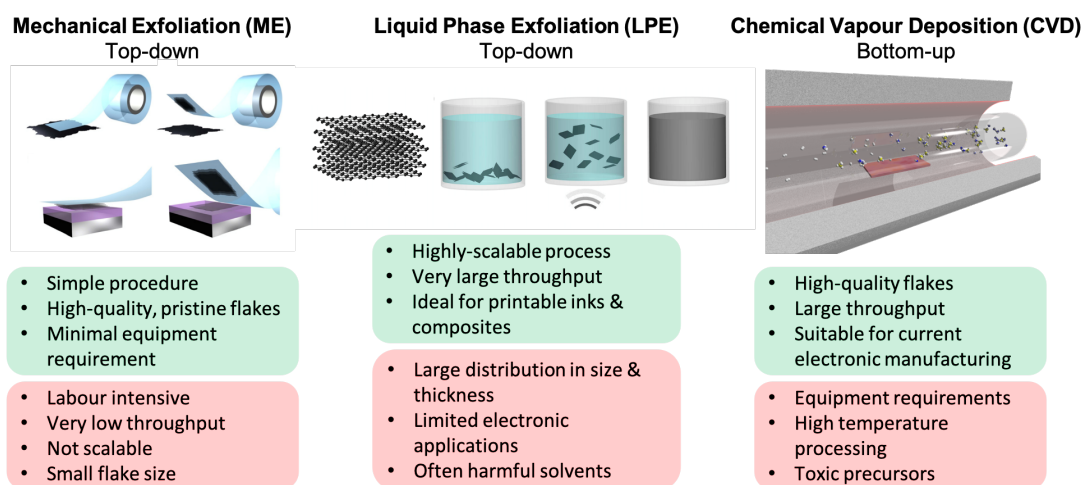


**Figure 2.12:** Schematic representation and summary of common pros and cons of the three main methods of 2D material fabrication.<sup>13,85</sup> (CVD image courtesy of Dr. Christian Wirtz)

Both ME and LPE are *top-down* approaches for fabrication of TMDs. A *bottom-up* synthesis is chemical vapour deposition (CVD). This technique generally involves flowing a precursor gas/gases into a chamber to interact with one or more heated substrates.<sup>92</sup> Rather than being reduced to few-layer or ML from bulk crystal, the TMD layer is synthesised from its base components. CVD-grown TMD films are generally of high-quality and can be deposited over large areas in ML ( $> 500 \mu\text{m}^2$ ) or few-layers. Compared to ME and LPE, CVD is most suited to the current electronic manufacturing and is used extensively in the production of electronic devices.<sup>93,94</sup> However, the caveat is that CVD can involve high temperatures ( $\sim 400 - 1000 \text{ }^\circ\text{C}$ ) that may not be compatible with the thermal budget of SC fabrication processes, as well as often toxic by-products. Another variant of CVD is thermally assisted conversion (TAC) or thermally assisted chalcogenisation, where a gas phase precursor is reacted with a solid phase, pre-deposited metal or oxide film.<sup>74,94,95</sup> In the case of TMDs this would be a reaction of its components, a transition metal film with a gaseous chalcogen, to form the corresponding TMD, eg. a Pt film and Se forming  $\text{PtSe}_2$ . TAC is a simple process with the thickness of the resulting material easily controlled by the deposited

thickness of the metal film. Metal films can be deposited in several ways including sputtering and evaporation. The conversion process results in the production of large-scale polycrystalline TMD with grains of few- to multilayer thicknesses on the order of 10 – 100 nm.<sup>94</sup> Device geometry can be determined pre-conversion as TAC is highly compatible with lithographic techniques, such as photolithography and electron beam lithography for patterning. In addition, like CVD, TAC can be readily translated to current electronic manufacturing, though its applications are limited due to the high polycrystallinity in the converted films.<sup>72,96</sup>

#### 2.4 SELF-ASSEMBLED MONOLAYERS (SAMs)

Chemical functionalisation of layered 2D materials, such as graphene or transition metal dichalcogenides (TMDs), is essential in modifying their properties and expanding their capabilities and applications.<sup>97</sup> Exploiting the functionalisation of TMDs is seen as a route to their widespread application of TMDs in photonics, energy storage and conversion, drug delivery and medical devices.<sup>98,99</sup> TMD surfaces tend to be rather inert to chemical functionalisation, due to saturation of basal plane chalcogen atoms.<sup>98,100</sup> Possible routes to functionalisation of TMDs include the physisorption of molecules from vapour phase or solution-cast molecular assemblies.<sup>101,102</sup> Self-assembled monolayers (SAMs), i.e. dense 2D monolayers comprised of organic molecules packed together and chemically adsorbed onto a surface,<sup>103</sup> have been in the scientific spotlight in recent years in various areas of research such as nano-functionalisation, biosensors and molecular electronics as active materials or insulators,<sup>101,104-106</sup> and are a well-known technique for creating highly functional nanostructures on 2D surfaces.

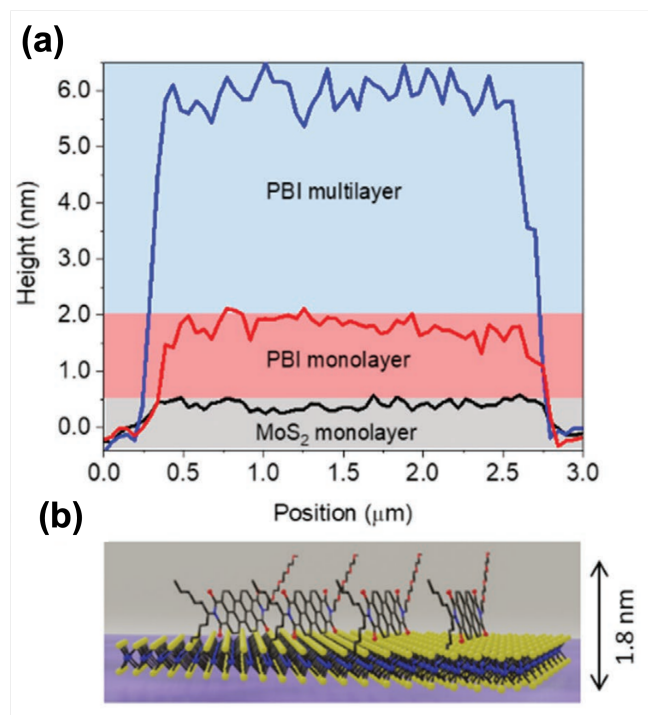


**Figure 2.13:** Functionalisation of 2D TMDs by perylene-based SAMs: (a) AFM height profiles of the TMD/PBI heterostructures with coloured regions for the PBI multilayer (blue), PBI monolayer (red) and MoS<sub>2</sub> monolayer before functionalisation. (b) Schematic of a PBI SAM deposited on a MoS<sub>2</sub> monolayer.<sup>102</sup>

Lee et al. demonstrated the tuning of graphene's electrical properties through the growth of a stable SAM of alkylsilane on top.<sup>106</sup> Kawanago et al. also applied SAM-based gate dielectrics to fabricate MoS<sub>2</sub> field-effect transistors.<sup>107</sup> Most recently, Tilmann et al. showed the non-covalent functionalisation of layered 2D materials through the selective formation of perylene-based SAMs on TMDs directly on the growth substrate (see Fig. 2.13),<sup>102</sup> opening up a pathway to controllable and versatile functionalisation of 2D materials.

## 2.5 LAYER-BY-LAYER THINNING METHODS

As the electronic properties of 2D materials are thickness dependent, the ability to control the layer thickness affords control over the properties. Since 2D materials have become a significant topic of interest, many thinning methods have been proposed, such as plasma etching, surface oxidation, scanning probe lithography/machining and laser irradiation.

Though the throughput is limited, the nanoscale control and resolution and the ability of *in-situ* imaging gives AFM nanolithography an advantage over other lithographic techniques. One of the earliest instances of nanomachining 2D materials was by Lieber and Kim<sup>108</sup>, whereby MoO<sub>3</sub> ( $\geq 5$  nm) grown on MoS<sub>2</sub> was selectively machined leaving the MoS<sub>2</sub> layer underneath relatively intact, as the MoS<sub>2</sub> layer does not wear under the same conditions as MoO<sub>3</sub>. Using a variant of this method, Hong *et al.* mechanically exfoliated Bi<sub>2</sub>Se<sub>3</sub> nanoribbons ( $> 50$  ML thickness) down to a single ML by drawing an AFM tip horizontally across the nanoribbons.<sup>109,110</sup> Through the tip force applied parallel to the layers, the Bi<sub>2</sub>Se<sub>3</sub> breaks along the vdW bonds, leaving some residual layers intact on the substrate.

Similar to nanomachining, oxidation-scanning probe lithography (o-SPL)<sup>47</sup> is another high-resolution technique. Rather than using mechanical force to etch the layers, it is based on the spatial confinement of an anodic oxidation reaction between the tip and the sample surface. For example, Liu *et al.* took advantage of the high spatial resolution of SPL and the tendency of black phosphorus (BP) to oxidise readily in ambient conditions to perform layer-by-layer thinning using conductive AFM (C-AFM), which was achieved via through DC local anodic oxidation (LAO).<sup>111</sup> By controlling the amplitude of the bias voltage during C-AFM (contact mode) scanning, patterns were created on a freshly exfoliated BP crystal, resulting in an oxidised byproduct easily removed by rinsing in water (see Fig. 2.14).

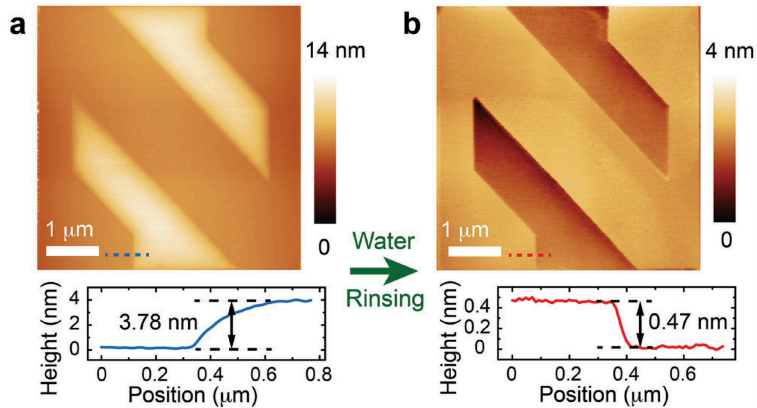


**Figure 2.14:** Tapping mode AFM images of patterned letter 'N' (a) after DC C-AFM patterning of BP and (b) after water rinsing.<sup>111</sup>

In a process similar to LAO, Donarelli *et al.* used a conductive AFM tip, negatively biased, to scan a MoS<sub>2</sub> flake 10 nm above the surface in the desired pattern, with the silicon substrate grounded.<sup>112</sup> The process was carried out in ambient conditions, resulting in a water meniscus forming between tip and sample whereby the top MoS<sub>2</sub> layers oxidise to MoO<sub>3</sub>, which can be removed by way of selective chemical etching (See Fig. 2.15).

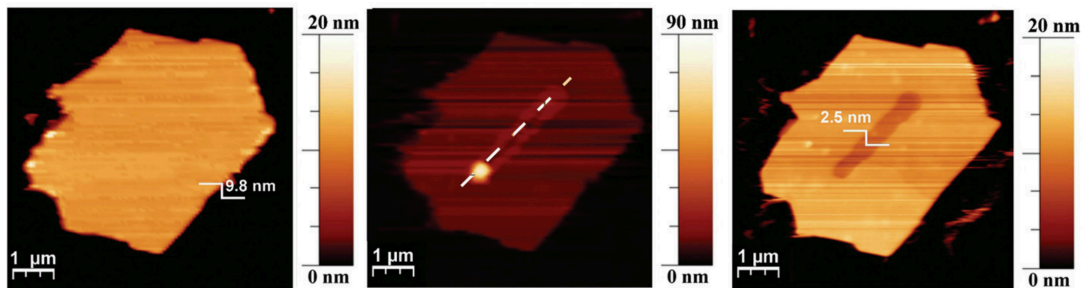


**Figure 2.15:** From left to right: MoS<sub>2</sub> pristine flake; MoS<sub>2</sub> flake after the lithography process (white dashed line represents the AFM tip path); MoS<sub>2</sub> flake after HCl etching. Tip voltage =  $-10$  V; tip speed =  $1 \mu\text{ms}^{-1}$ . Etching parameters: 10 s in 0.05 M HCl.<sup>112</sup>

Another thinning method based on the oxidation of the 2D material surface is that of plasma oxidation. Li *et al.* used this technique on WSe<sub>2</sub> by exposing it to a remote oxygen plasma, resulting

in selective oxidation of the topmost layer, which can be easily removed in KOH solution. The oxidation is self-limiting due to the low kinetic energy of the oxygen radicals in the remote plasma, even with varying exposure times.<sup>113</sup> This was again observed in MoS<sub>2</sub><sup>114</sup> and MoTe<sub>2</sub><sup>115</sup> (see Fig. 2.16) via the same method by Zhu *et al.* and Zheng *et al.* respectively, whereby the oxidised top layer MoO<sub>3</sub> was removed by thermal annealing instead of solution.

Similarly, 2D materials can also be thinned using laser irradiation. Laser thinning offers several advantages compared to other thinning methods, particularly simplicity, low cost and the lack of need for complicated lithographic processing.<sup>116</sup> Castellanos-Gomez *et al.*<sup>117</sup> reported thinning MoS<sub>2</sub> samples to MLs from bulk material with an initial thickness of  $\sim 20$  layers, but without any control over layer precision during thinning. Hu *et al.*<sup>118</sup> did show some thickness control in MoS<sub>2</sub>, but were limited to producing thicknesses of three layers or below and needed multiple laser scans to achieve this control. Finally, Nagareddy *et al.* reported the humidity-controlled uniform thinning of multilayered MoTe<sub>2</sub> films down to the ML with layer-by-layer precision via continuous wave laser irradiation of an ultralow laser power density of  $0.2 \text{ mW}\mu\text{m}^{-2}$  (see Fig. 2.16).<sup>116</sup>



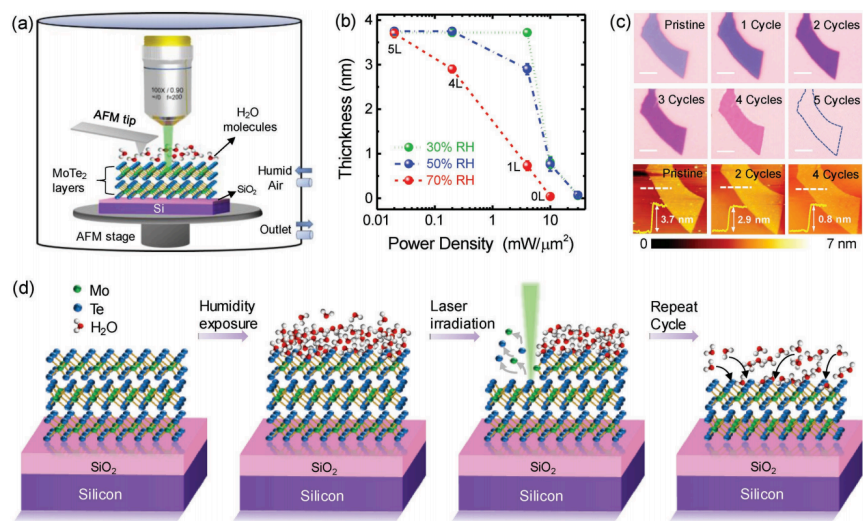


**Figure 2.16:** (a) Schematic illustration of the experimental setup used for thinning and in situ imaging of MoTe<sub>2</sub>. (b) Change in thickness of multilayered MoTe<sub>2</sub> samples as a function of incident laser power at different humidity levels. (c) Optical microscope images and corresponding AFM topography images of MoTe<sub>2</sub> samples after each thinning cycle. (d) Schematic illustrations explaining the suggested MoTe<sub>2</sub> photochemical thinning mechanism.<sup>116</sup>

## 2.6 DEVICE FABRICATION

As previously mentioned, the use of semiconductor (SC) technology exploded after the development of the transistor,<sup>6</sup> followed by the integrated circuit (IC) and the microchip. As a result, SCs have become ubiquitous in our everyday lives due to their highly economical miniaturisation and reliability. In recent years, 2D materials have become attractive for integration into current and future SC manufacturing architectures, such as transparent, flexible devices.

Of the many types of transistors available, field effect transistors (FETs), specifically metal-oxide-semiconductor FETs, have been the most important for digital electronics. A field effect transistor (FET) is a three-terminal device (source, drain, gate) in which the conductivity of a SC layer is modulated by a transverse electric field<sup>119</sup> and is commonly used for weak-signal amplification. A FET consists of a channel of n- or p-doped SC material through which current can flow with the gate modulating the flow of charge carriers between the source and drain.<sup>119</sup> They are known as unipolar transistors since they only involve single-carrier-type operation, wither electrons or holes. FETs can be subdivided into several types of devices such as junction (JFET), metal-oxide-semiconductor (MOSFET), metal-semiconductor (MESFET) and tunneling (TFET). Of these, the MOSFET is the most important device for advanced integrated circuits due to their low power consumption, massive manufacturing yield and can be constructed entirely out of silicon and its oxides.<sup>120</sup> As a result, the MOSFET is extensively used in the study of SC surfaces.<sup>121</sup>

The MOSFET consists of an MOS capacitor and two p-n junctions (see Fig. 2.17) and can be built as either n- or p-MOS transistors, depending on the polarities of the bulk (also known as the channel), source and drain regions. Fig. 2.17 shows an n-MOSFET whereby the majority carriers are electrons, the Si substrate is p-doped with n-type regions called the source and drain, and *vice versa* for a p-MOSFET. The gate oxide is a very thin insulating oxide layer that covers the channel region, on top of which a conducting gate material, either metal or highly doped polysilicon, is deposited.

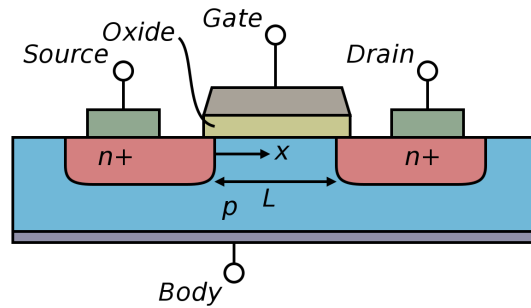


Figure 2.17: A cross-section of a basic (n-)MOSFET structure.<sup>122</sup>

For an n-MOSFET, when no voltage is applied between gate and source ( $V_G = 0$ ), some current flows due to the voltage between the drain and source ( $V_{DS}$ ). At relatively small values of  $V_{DS}$ , the IV characteristics of the device are linear, with the drain current  $I_D$  increasing proportionally with increasing drain voltage  $V_D$ . When a positive gate voltage is applied ( $V_G > 0$ ), the minority carriers in the channel, in this case holes, are repelled and the majority carriers (electrons) are attracted to the gate oxide layer, increasing the electron density in the channel inversion layer. This allows a certain amount of  $I_D$  to flow through source to drain, allowing  $V_G$  to control the device current.

### 2.6.1 SCHOTTKY VS. OHMIC CONTACTS

One of the most common junctions within electronic devices are metal to SC interfaces, which often result in Schottky barriers, a potential energy barrier for electrons formed at a (rectifying) metal-SC junction. A metal-SC interface that has negligible contact resistance relative to the bulk is known as an ohmic contact (non-rectifying). It does not degrade device performance and can pass the required current with only a very small voltage drop when compared to the overall drop across the active region of the device.

A MESFET comprises of a non-rectifying metal-SC junction.

MESFETs have similar current-voltage characteristics to MOSFETs however the source and drain contacts are ohmic rather than p-n junctions like in MOSFETs. Current transport is also due to majority carriers unlike MOSFETs which are minority carrier devices. Schottky diodes are used in high frequency electronics due to their higher switching speeds.<sup>123</sup>

If any two conducting materials in electrical contact are in thermal equilibrium, their Fermi levels must be continuous across the junction. These requirements determine a unique energy band

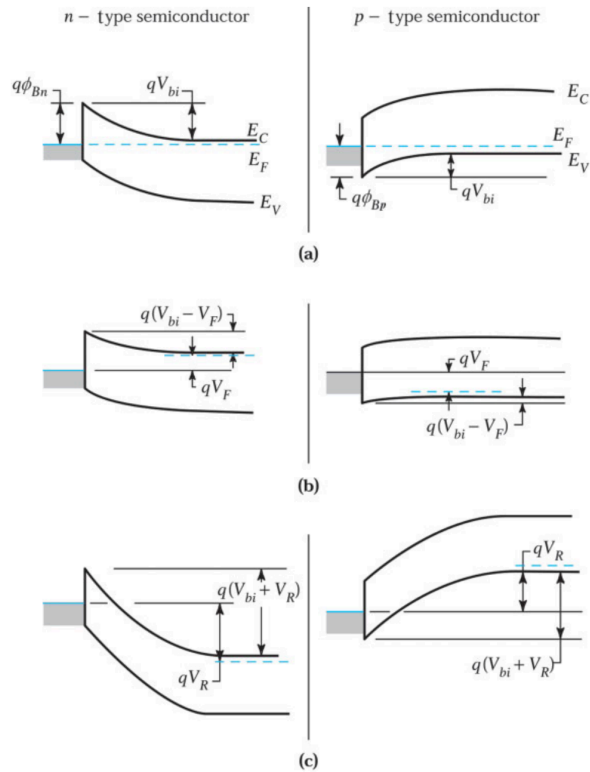


**Figure 2.18:** Energy band diagrams of metal n-type and p-type semiconductors under different biasing conditions: (a) thermal equilibrium; (b) forward bias; and (c) reverse bias.<sup>123</sup>

diagram for the ideal metal-semiconductor contact (Fig. 2.18), where the barrier height  $q\phi_{Bn}$  is the difference between the metal work function  $\phi_m$  and the SC electron affinity  $\chi_s$ :

$$q\phi_{Bn} = q\phi_m - q\chi_s \quad (2.18)$$

Similarly, for an ideal contact between a metal and a p-type SC, the barrier height  $q\phi_{Bp}$  is:

$$q\phi_{Bp} = E_g - (q\phi_m - q\chi_s) \quad (2.19)$$

where  $E_g$  is the bandgap of the SC. Therefore, for any given SC and metal system, the sum of the barrier heights for n-type and p-type is expected to be equal to the band gap:

$$q(\phi_{Bn} + \phi_{Bp}) = E_g \quad (2.20)$$

On the SC side, the electrons in the conduction band (CB) encounter a built-in potential ( $V_{bi}$ ) when trying to move into the metal:

$$V_{bi} = \phi_{Bn} - V_n \quad (2.21)$$

where  $qV_n$  is the distance between the bottom of the CB and the Fermi level. Similar equations can be derived for a p-type SC.

For Schottky diodes, which utilise Schottky barriers, operated at RT, the dominant transport mechanism is thermionic emission of majority carriers from SC over potential barrier into the metal. When a forward bias  $V_F$  is applied to the contact, the electrostatic potential difference across the barrier is reduced, resulting in electron flow out of the SC and into the metal. Nevertheless, the flux of electrons from the metal into the SC remains the same because the barrier  $\phi_{Bn}$  remains at its equilibrium value. Likewise when a reverse bias  $V_R$  is applied,  $\phi_{Bn}$  remains constant and it is the flux

of electrons from the SC into the metal that decreases below its equilibrium value.

While Schottky barriers are useful for certain applications, they can significantly hinder device performance of 2D materials.

### 2.6.2 HETEROJUNCTIONS

A heterojunction or heterostructure is the interface between two regions or layers of materials that are juxtaposed. Heterojunctions are widely used as a base in SC devices owing to their structural, interfacial and electronic properties.<sup>124</sup> Heterostructures can be easily synthesised by availing of vdW coupling in 2D materials, e.g. sequentially stacking layered materials such as TMDs, resulting in a vertical heterostructure. They can also be fabricated through the adherence of self-assembled monolayer (SAMs) on top of 2D materials, creating organic-inorganic heterostructures.

Heterojunctions in SC materials result in unequal band gaps, that is the energy difference between the valence band (VB) and the conduction band (CB). The band gap can range from 0 eV (i.e. no gap) in a metal to over 4 eV in an insulator. Due to unequal band gaps, SC interfaces can be classified into three heterojunction types, which are illustrated in Fig. 2.19.

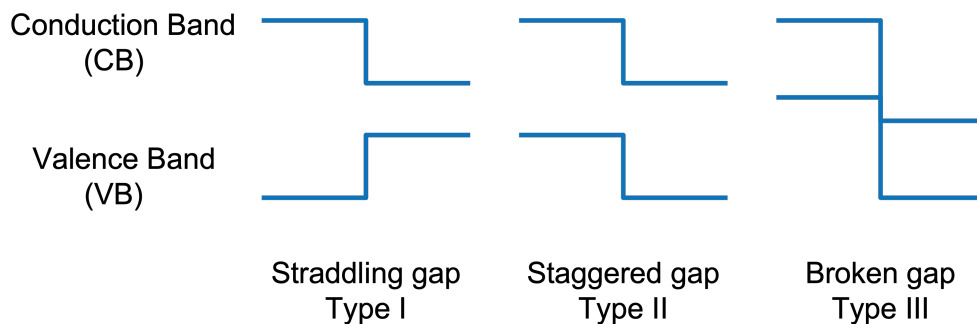


**Figure 2.19:** The three different types of heterojunctions in SC interfaces; type I - straddling gap, type II - staggered gap, and type III - broken gap.

- **Type I - straddling gap**

The bandgap of one SC is entirely contained within the bandgap of the other one, i.e.  $E_{g1} > E_{g2}$ ,  $E_{V1} < E_{V2}$  and  $E_{C1} > E_{C2}$ . These junctions result in ultrafast recombination between electrons and holes and are mostly used in optoelectronic applications. Examples of 2D material heterostructures of this kind are MoS<sub>2</sub>/ReS<sub>2</sub> and WSe<sub>2</sub>/BP.<sup>125,126</sup>

- **Type II - staggered gap**

The bandgaps overlap but the CB and VB of the second SC are both lower than the CB and VB of the first, i.e.  $E_{V1} > E_{V2}$  and  $E_{C1} > E_{C2}$ . Type II heterojunctions can promote charge carrier transfer and separation at the interface and localised VBM and CBM states further enhance charge separation and enable carriers to be easily collected, making these junctions ideal for solar cells.<sup>127</sup> Staggered gaps can be found in heterostructures of the most commonly synthesised TMDs such as MoS<sub>2</sub>, WS<sub>2</sub>, MoSe<sub>2</sub> and WSe<sub>2</sub>.<sup>128</sup>

- **Type III - broken gap**

The bandgaps do not overlap at all or the VB of the first SC overlaps with the CB of the second SC. In the case of the latter, the CB electron states in the n-type material are more or less aligned with the VB hole states in the p-type material. This overlap at the junction results in a negative resistance, allowing for high electron tunnel efficiency. Broken gaps has been shown for Bi<sub>2</sub>Te<sub>3</sub>/WSe<sub>2</sub> and p-WSe<sub>2</sub>/n-MoO<sub>x</sub> vdW systems.<sup>129</sup>

### 2.6.3 CONTACT RESISTANCE & INTERFACE GEOMETRIES

A major obstacle in the development and integration of practical 2D electronic and optoelectronic devices which must be addressed is that of reliable, low-resistance electrical contacts to 2D materials.<sup>130</sup> It has been shown that large contact resistances can occur between TMD channels and bulk metal contacts, significantly reducing the efficiency of current flow.<sup>131</sup> Regardless of the

electrode material used, it requires the transmission of electrons through the interface between two different crystal lattices, which always causes a contact resistance due to reflections, Schottky barriers and scattering at the interface.<sup>132</sup> Low contact resistance in 2D SC devices is crucial for achieving high 'on' current, large photoresponse<sup>133</sup> and high-frequency operation.<sup>134</sup> Nevertheless, the chemical interaction at the metal-SC interface governs everything for 2D materials. Pristine surfaces of 2D materials (i.e. no dangling bonds) hinder formation of any interface bonds with a metal, thus increasing contact resistance.<sup>135</sup>

There are two possible geometries at the interface between bulk (3D) metals and 2D materials: top contact and edge contact (Fig. 2.20), each of which perform differently. While top contacts are relatively straightforward to fabricate, edge contacts are difficult to make using standard lithographic techniques on a single/few-layered 2D material.<sup>135</sup> However, in most experiments, the contacts are a combination of both geometries. This is particularly true for devices based on TAC-grown channels.

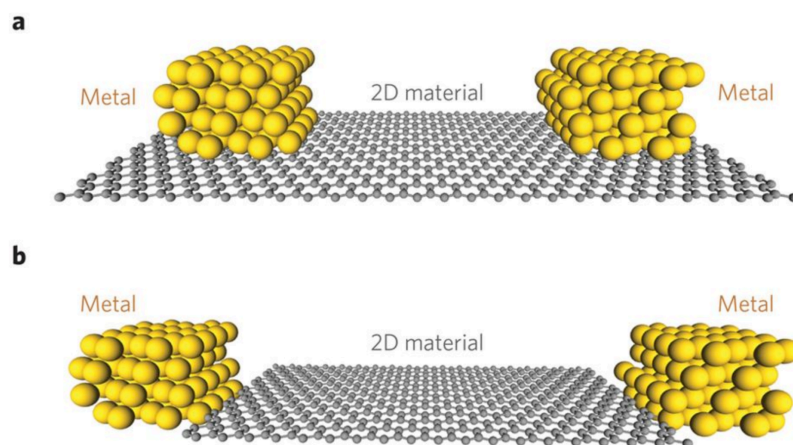


**Figure 2.20:** Schematic representation of interface geometries between 2D materials and their metal contacts in (a) top contact and (b) edge contact configurations.<sup>135</sup>

As it is difficult for metals to covalently bond with pristine 2D material surfaces, a van der Waals (vdW) gap forms at the interface, acting as an additional tunneling barrier for the charge carriers, in addition to any innate Schottky barrier.<sup>130,136</sup> This extra barrier reduces the charge injection from



metals, which leads to higher contact resistance. By reducing this vdW tunnel barrier as well as optimising edge contacts with all layers of the 2D material to produce a more seamless contact design, the contacts can be significantly improved with reduced resistance.

## 2.7 RAMAN SPECTROSCOPY

As a characterisation technique, Raman spectroscopy is powerful, non-invasive and non-destructive. It can provide crystal structure information, hence it is used extensively on 2D materials such as graphene and TMDs.<sup>76</sup> It works on the principle that when monochromatic light interacts with a sample, it will be absorbed, reflected or scattered. The vast majority of photons scatter elastically, known as Rayleigh scattering. These scattered photons are the same frequency,  $\omega_0$ , as the incoming beam. However, about one in  $10^7$  are scattered inelastically in a process known as Raman scattering, due to the interactions with molecular or lattice vibrations in the sample, whereby the frequencies of the weakly scattered photons are  $\omega_0 \pm \omega_q$ , with  $\omega_q$  is the vibrational frequency of the molecule. The Raman effect is named after the Indian physicist Sir C. V. Raman who first reported the phenomenon in 1928.<sup>137</sup> To obtain a Raman spectrum, a monochromated light source (i.e. laser) is shone on a sample and the intensity of scattered light as a function of frequency is measured.

Raman scattering can be classified as two relative probabilities, Stokes ( $\omega_0 - \omega_q$ ) and Anti-Stokes ( $\omega_0 + \omega_q$ ). In Stokes Raman scattering, the chemical bonds in the material absorb some of the energy thus the molecule is left in an excited state, as illustrated in Fig. 2.21(a). The scattered light is lower in energy (frequency), whereas it is conversely higher in energy (frequency) for Anti-Stokes scattering (Figure 2.21(a)). If the polarizability of the molecule is altered after interacting with the incident photon, the vibration is said to be Raman active, differentiating it from vibrations that are infrared (IR) active whereby the dipole moment must change. The energy change in light is

dependent on bonds and symmetry in the material, allowing Raman signals to act as a characteristic fingerprint of materials.<sup>138</sup>

Raman spectra are typically displayed in terms of Raman shift with units of wavenumbers (inverse wavelength,  $\text{cm}^{-1}$ ) relative to the excitation light (e.g. 532 nm). This Raman shift represents the difference in energy between the incident and emitted photon, thus giving the energy difference of the initial and final vibrational levels of the molecule. The frequency shift of the light depends on the bonds and symmetry in the material, producing a characteristic peak for each Raman active vibrational mode. Fig. 2.21(b) shows a typical Raman spectrum of molecular vibrations with mirrored positive and negative Raman shifts, for Stokes and Anti-Stokes respectively. However, the Anti-Stokes peaks are much lower in intensity than the Stokes under normal conditions due to the Maxwell-Boltzmann distribution law that describes the population of thermally excited vibrational states.<sup>139</sup> Since both give the same information, it is conventional to measure the Stokes side of the spectrum.<sup>140</sup> The large intensity at  $0 \text{ cm}^{-1}$  is where all reflected and Rayleigh scattered light is detected. An application of the Anti-Stokes signal is coherent Anti-Stokes Raman spectroscopy (CARS), which is used to enhance the naturally weak spontaneous Raman signal.<sup>141</sup>

### 2.7.1 CLASSICAL RAMAN THEORY

Though quantum mechanical Raman theory is necessary to fully describe the Raman phenomenon, classical Raman theory can describe most Raman effects. The following is adapted from ‘Introductory Raman Spectroscopy’ by J. R. Ferraro, K. Nakamoto and C. W. Brown.<sup>138</sup>

In classical Raman theory, a molecular dipole moment  $\vec{\mu}$  in the system, induced by an electric field  $\vec{E}$ , can be defined as:

$$\vec{\mu} = \alpha \vec{E} \quad (2.22)$$

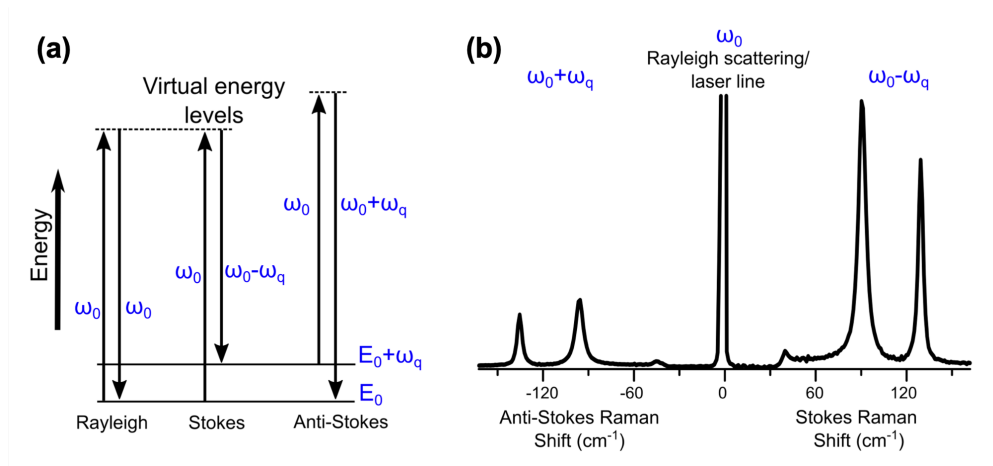


**Figure 2.21:** (a) Jablonski schematic of the excitation to, and relaxation from, an excited energy state for Rayleigh, Stokes and Anti-Stokes scattering. (b) Typical Raman spectrum showing the three scattering types. (Figure courtesy of Dr. John McManus)

where  $\alpha$  is the proportionality constant known as polarisability, i.e. how much the electron density is perturbed by the electric field. The electric field strength of the electromagnetic wave  $\vec{E}$  (i.e. laser beam) fluctuates with time  $t$ :

$$\vec{E} = \vec{E}_0 \cos(\omega_0 t) \quad (2.23)$$

where  $\vec{E}_0$  is the vibrational amplitude and  $\omega_0$  is the frequency of the laser. If the molecule is vibrating with a frequency  $\omega_q$ , the nuclear displacement  $q$  is written as:

$$q = q_0 \cos(\omega_q t) \quad (2.24)$$

where  $q_0$  is the vibrational amplitude. The polarisability is influenced by the nuclear motion due to the geometry of the nucleus constantly changing to minimise the energy of the system. This change in polarisability can be described using a Taylor series expansion:

$$\alpha = \alpha_0 + \left( \frac{\partial \alpha}{\partial q} \right)_{q_0} q_0 + \dots \quad (2.25)$$

where  $\alpha_0$  is the polarisability at the equilibrium position and  $(\partial\alpha/\partial q)_{q_0}$  is the rate of change of  $\alpha$  with respect to the change in  $q$  at the equilibrium position. Combining the previous four equations, we obtain:

$$\mu(t) = \underbrace{\alpha_0 \vec{E}_0 \cos(\omega_0 t)}_{\text{Rayleigh}} + \underbrace{\frac{1}{2} \left( \frac{\partial\alpha}{\partial q} \right)_{q_0} q_0 \vec{E}_0 \cos[(\omega_0 - \omega_q)t]}_{\text{Stokes}} + \underbrace{\frac{1}{2} \left( \frac{\partial\alpha}{\partial q} \right)_{q_0} q_0 \vec{E}_0 \cos[(\omega_0 + \omega_q)t]}_{\text{Anti-Stokes}} \quad (2.26)$$

In this equation, the first term represents Rayleigh scattering, the second and third terms representing Stokes scattering, where incident light re-emitted is red-shifted, and Anti-Stokes scattering, where the emitted light is blue-shifted. If  $(\partial\alpha/\partial q)_{q_0} = 0$ , the vibration is not Raman-active.

### 2.7.2 RAMAN OF TMDs

For TMDs, Raman spectroscopy can give information on chemical species/elemental composition, crystal structure, phase, defects, strain, doping and even film thickness/number of layers.<sup>76,142,143</sup> The Raman spectra of TMDs are generally characterised by two main peaks, corresponding to the in-plane and out-of-plane motion of the atoms. These key modes for 2H and 1T configurations are summarised in Fig. 2.22(a) and (b). Additional modes can be observed in the low-frequency ( $< 50\text{cm}^{-1}$ ) region of the Raman spectrum of TMDs. These are referred to as the shear mode (SM) and layer-breathing mode (LBM).<sup>144</sup> These low-frequency modes occur due to relative motions of the planes themselves, either in-plane or out-of-plane to the atomic layers, as illustrated in Fig. 2.22(c). As such, these modes only occur for multilayers, i.e.  $\geq 2$  layers (L), and can be used to further characterise 2D materials e.g. layer number and stacking sequence.<sup>145,146</sup> Single layer  $\text{MoS}_2$  and  $\text{WS}_2$  both show  $D_{3d}$  symmetry.<sup>143,147</sup> The unit cell consists of one metal atom (Mo/W) sandwiched between two sulfur atoms. For a  $\text{MoS}_2$  monolayer, the modes can be

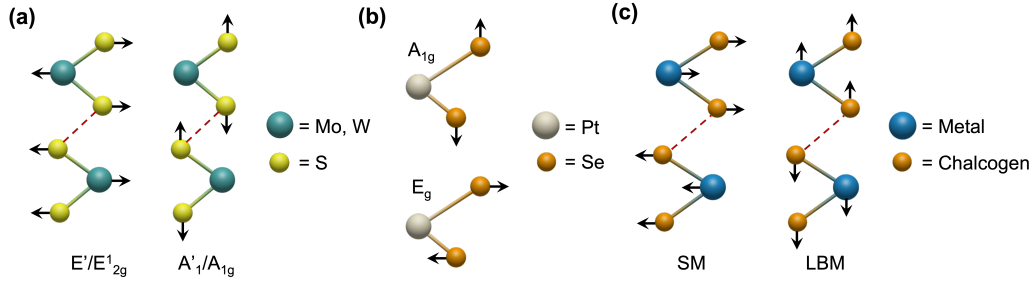


**Figure 2.22:** Typical in-plane ( $E_g/E'_{2g}$ ) and out-of-plane ( $A_{1g}$ ) Raman active vibrational modes of TMDs of (a) 2H-MoS<sub>2</sub>/WS<sub>2</sub> and (b) 1T-PtSe<sub>2</sub>. (c) Overview of the layer breathing mode (LBM) and shearing mode (SM) of TMDs in low-frequency Raman spectroscopy.

decomposed into the following irreducible representations:<sup>148</sup>

$$\Gamma_{1L}^{MoS_2} = A_{1g} + E_{1g} + 2A_{2u} + 2E_{2g}^1 \quad (2.27)$$

Though the  $A_{1g}$ ,  $E_{1g}$  and  $E_{2g}^1$  symmetries are all Raman active modes, the  $E_{1g}$  mode requires a scattering geometry with a  $\mathbf{z}$  component which cannot be significantly observed experimentally in the 2D monolayer. Pristine CVD-grown monolayer MoS<sub>2</sub> typically has Raman peaks observed at  $\sim 384\text{cm}^{-1}$  and  $\sim 405\text{cm}^{-1}$ , corresponding to in-plane ( $E_{2g}^1$ ) and out-of-plane ( $A_{1g}$ ) vibrational modes respectively, when excited at 532 nm.<sup>145,149,150</sup>

The WS<sub>2</sub> Raman spectrum can be similarly characterised *via* the first order modes. Pristine WS<sub>2</sub> exhibits a characteristic peak at  $352\text{cm}^{-1}$ , which, when excited at 532 nm, is a combination of several different modes. Of these, the most intense are the in-plane vibrational mode ( $E_{2g}^1$ ) and the resonantly excited  $2\text{LA}(M)$  phonon mode.<sup>145,151</sup>

As PtSe<sub>2</sub> exhibits a  $D_{3d}$  point-group symmetry, it produces the following irreducible modes at the

<sup>‡</sup>The true labelling for ML MoS<sub>2</sub> symmetries are  $A'_1$ ,  $E''$  and  $E'$ . For simplicity, the labelling convention for bulk MoS<sub>2</sub> is used.<sup>143</sup>

centre of the Brillouin zone:

$$\Gamma_{1L}^{PtSe_2} = A_{1g} + E_g + 2A_{2u} + 2E_u \quad (2.28)$$

$A_{1g}$  (out-of-plane) and  $E_g$  (in-plane) are the two Raman-active modes, as shown in Figure 2.22(b). The  $E_g$  and  $A_{1g}$  modes are generally observed at  $\sim 175 \text{ cm}^{-1}$  and  $\sim 205 \text{ cm}^{-1}$  respectively for the ML when excited at 532 nm. As layer number is increased, the  $E_g$  mode is gradually red-shifted to lower wavenumbers.<sup>76,146</sup> In addition, the  $A_{1g}/E_g$  intensity ratio gradually increases with increasing layer thickness.<sup>76,146</sup> The less intense feature at  $\sim 230 \text{ cm}^{-1}$  is assigned to an overlap between the  $A_{2u}$  and  $E_u$  modes, which are longitudinal optical (LO) modes involving the out-of-plane and in-plane motions of Pt and Se atoms respectively.<sup>76</sup> This contribution is most evident with close-to-ML thickness and decreases in relative intensity with increasing flake thickness.

## 2.8 PHOTOLUMINESCENCE

This section is adapted from the books edited by C. S. S. Kumar and by D. L. Andrews, G. D. Scholes and G. P. Wiederrecht. .<sup>152,153</sup>

Luminescence is a phenomenon involving the spontaneous emission of light radiation from a substance or material following the absorption of energy into an excited state. Photoluminescence (PL) is where the energy absorbed is in the form of photons, leading to the electrons in the ground state being excited to a higher energy state and after some energy loss (relaxation), the excited electrons return to ground state along with the emission of a photon.

PL is a powerful emission spectroscopy technique for characterising and studying the properties of nanomaterials, due to its relative simplicity. Again, similar to Raman, it is a non-invasive and non-destructive technique. PL spectroscopy involves the excitation of a sample with a

monochromatic light source, typically a laser, and the detection of the emitted light. A PL spectrum is obtained by scanning and measuring the emitted light.

Room temperature (RT) PL is often used as an indicator of the crystal quality of the material, but this does not take into account the possible presence of non-radiative defects and the fact that the ratio of near-band edge emission to defect emission is strongly dependent on the measurement conditions.

PL can provide much information on the optical properties of semiconductors, such as both intrinsic and defect-related recombination process, as well as giving an overview of the SC material's optical quality. In a bulk SC, the absorption of a photon leads to excitation of an electron from the VB to the CB. The charge carriers are separated by distances that encompass several molecules or ions. This separation, along with the high dielectric constant of the material, makes their binding energy relatively small. The minimum amount of energy required to form the charge carriers is known as the SC's band-gap energy ( $E_g$ ). The absorption of photons with energy similar to that of the band gap,  $h\nu \geq E_g$ , leads to an optical transition producing a hole in the VB and an electron in the CB. Absorption of photons with energy greater than  $E_g$  produces excitations above the CB edge. The resulting electrons can lose the excess energy through non-radiative processes. Therefore PL spectroscopy is a direct method for determining the bandgap in TMDs.

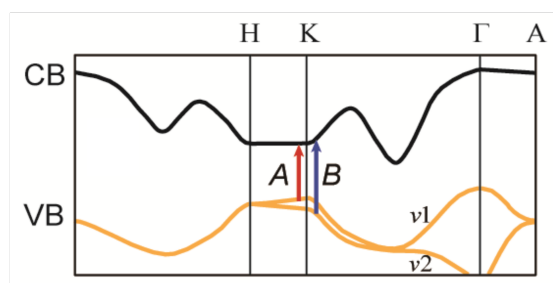


**Figure 2.23:** Simplified band structure of bulk MoS<sub>2</sub>. The black line is the conduction band minimum (CBM). The two orange lines show the highest valence bands split by the interlayer interactions. The two arrows are the direct-gap transitions showing the A exciton (red) and B exciton (blue).<sup>154</sup>

Most Mo- and W- based TMDs exhibit a transition from an indirect to a direct bandgap SC with decreasing layer thickness down to the monolayer which can explain the observed jump in ML photoluminescence efficiency,<sup>66</sup> where the PL quantum yields in ML MoS<sub>2</sub> increase by up to a factor of  $\sim 10^4$  from the bulk.<sup>18,64</sup> This results in ML MoS<sub>2</sub> on Si/SiO<sub>2</sub> exhibiting strong PL at RT from the A exciton<sup>§</sup> which is the most prominent peak at  $\sim 1.85$  eV (670 nm).<sup>149,150,156</sup> ML MoS<sub>2</sub> has a second weaker component in its PL, referred to as the B exciton, at  $\sim 2$  eV.<sup>154</sup> The two components are known to arise from direct-gap optical transitions between the maxima of split valence bands ( $\nu_1, \nu_2$ ) and the conduction band minimum (CBM), all located at the K-point of the Brillouin zone, as n in Fig. 2.23.<sup>64,154</sup> Pristine ML WS<sub>2</sub> also exhibits a strong PL response with only one direct electronic transition at  $\sim 1.95$  eV,<sup>71</sup> which is up to three orders of magnitude stronger than that of multilayers.<sup>69</sup>

One issue that can affect spectra are the measurement conditions such as temperature and excitation energy.<sup>157</sup> The PL of TMDs in particular is very sensitive to changes in structure and environment, with the crystal quality influencing the intensity, peak position and the FWHM of the PL peak.<sup>156</sup> Similar to Raman, MoS<sub>2</sub> PL is known to be sensitive to temperature,<sup>158,159</sup> strain,<sup>160–162</sup> dielectric,<sup>163</sup> defects,<sup>164–166</sup> substrate<sup>167,168</sup> and dopants.<sup>169,170</sup> Mouri *et al.* demonstrated that p-type doping with high electron affinity chemical dopants seems to enhance PL intensity, while n-type doping tends to reduce it.<sup>171</sup>

---

<sup>§</sup>Excitons, according to the Wannier-Mott model, are quasiparticles that are a combination of an electron and a positive hole bound by Coulomb interaction. A characteristic feature of excitons is that their formation (e.g. at optical excitation) does not lead to the separation of carriers, thus the excitons are electrically neutral excitations.<sup>155</sup>



*Certain people - men, of course - discouraged me, saying science was not a good career for women. That pushed me even more to persevere.*

Françoise Barré-Sinoussi, virologist & discoverer of HIV

# 3

## Experimental Methods

IN THIS CHAPTER, A GENERAL OVERVIEW and details of the various pieces of equipment and techniques used to synthesise, fabricate and characterise the materials explored in this thesis are provided. The theory behind these techniques is largely contained in Chapter 2, except in some cases where it was deemed more suitable to be included here.

### 3.1 GENERAL MATERIALS

All materials synthesised and exfoliated in this work were grown/transferred to SiO<sub>2</sub>/Si substrates purchased from University Wafers and Dasom RMS. These substrates consisted of 500 μm thick Si (100) with a top layer of 300 nm SiO<sub>2</sub> obtained by dry thermal oxidation. The Si substrates are cleaned before every CVD run and post-mechanical exfoliation transfer by rinsing the substrates in acetone followed by isopropanol (IPA). The substrates are then dried using nitrogen gas (N<sub>2</sub>). This cleaning process removes the majority of large surface contaminants.

All chemicals were ordered from Sigma-Aldrich/Merck unless specified otherwise and were used as received. Metal targets for metal film deposition were obtained from HMW-Hauner. All gases were supplied by BOC gases.

TMD crystals for mechanical exfoliation (ME) were purchased from HQ Graphene. Nitto Denka BT-150E-CM and Scotch Magic tape were used during the mechanical exfoliation process.

### 3.2 MATERIAL SYNTHESIS

The fabrication of materials used in this thesis can be experimentally divided into two categories: mechanical exfoliation (ME) and vapour phase deposition (VPD), which can be further subdivided into thermally assisted conversion (TAC) and chemical vapour deposition (CVD).

#### 3.2.1 VAPOUR PHASE DEPOSITION

Both VPD methods were performed in quartz tube furnaces, with a separate dedicated furnace used for each chalcogen examined to minimise cross-contamination (see Fig. 3.1). Both use qualitatively similar process, with the primary difference being the chalcogen heating element. The sulfur heater (low-temperature zone, see left image in Fig. 3.1) was an array of halogen lamps, while the other low-

temperature zone had its own dedicated selenium furnace (see right image in Fig. 3.1). Throughout this work, solid phase chalcogen precursors were used, consisting of either sulfur powder or selenium pellets (< 5 mm, > 99.99 % purity). The melting temperatures of the chalcogens are well below the reaction temperatures and using a lower-temperature zone for the vapourisation of the chalcogen prevents excessive amounts of chalcogen in the furnace. Two distinct types of transition metal (TM) sources were used in the CVD synthesis; a thin layer of TM oxide eg. MoO<sub>3</sub> or a sputter deposited TM film on a SiO<sub>2</sub>/Si substrate.

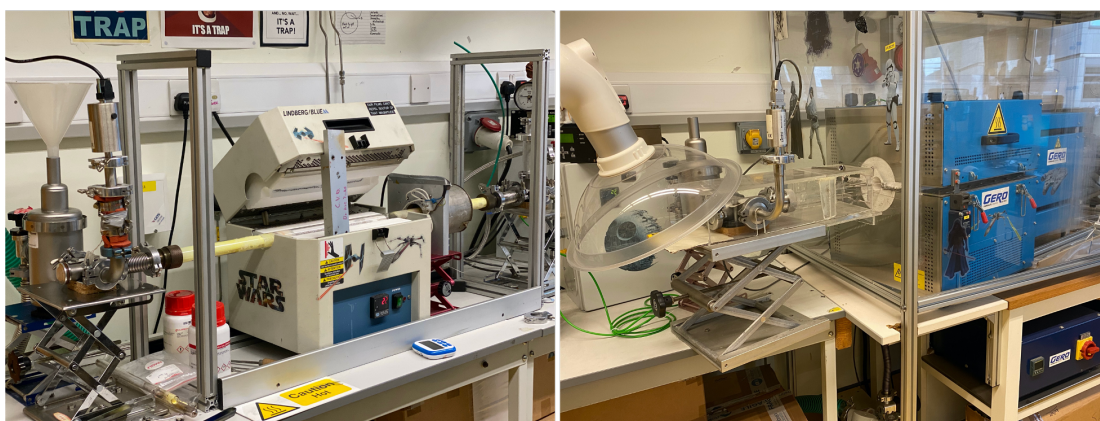


**Figure 3.1:** Photos of sulfur (left) and selenium (right) two-zone furnaces used in this work for both TAC and CVD processes.

### 3.2.2 METAL DEPOSITION

For thermally assisted conversion (TAC) of TM (Mo, W, Pt) to TMD, the transition metal thin films were deposited by physical vapour deposition (PVD) onto Si/SiO<sub>2</sub> substrates. Three methods of PVD were used to deposit a controlled thickness of TM; argon-ion sputtering, electron beam evaporation and molecular beam epitaxy (MBE).

For argon-ion sputtering, the sputter coater used was a Gatan Precision Etching and Coating System (PECS) which involves a beam of high energy Ar ions striking a desired metal target, a MaTeck Pt

target in this case, thus sputtering onto the substrate below. The chamber pressure was  $\sim 5 \times 10^{-5}$  mbar during the deposition, with a deposition rate between 0.3 to 1 Å/s. While this method is relatively straightforward, the impacting high energy metal atoms can damage the sample surface and any underlying films. These embedded metal atoms may result in gate leakage. In addition, the tool has limited throughput due to  $\sim 2 \times 2$  cm sample size limitation.

For e-beam evaporation of TM, a Temescal FC-2000 Evaporation System was used, whereby a high energy beam of electrons bombards a metal target, heating the target until the metal atoms evaporate thus depositing a thin film on the substrate. E-beam evaporation can offer good thickness control and the material flux is a less energetic and therefore a less damaging technique than sputtering.

In addition, molecular beam epitaxy (MBE) was used, whereby thin films are grown with precise control over properties such as thickness, stoichiometry and crystal phase. The chosen materials are evaporated in ultra high vacuum (UHV) and the resultant evaporant flux impinges on a substrate, typically a single crystal held at high temperature. Growth of Pt thin films were carried out in a DCA M600 MBE system with a base pressure of  $5 \times 10^{-10}$  Torr on a variety of Al<sub>2</sub>O<sub>3</sub> growth substrates; c-plane sapphire, r-plane sapphire and amorphous alumina. The substrates were annealed under vacuum for  $\sim 2$  hours prior to deposition. Pt was deposited at 600 °C.

All three tools use a quartz crystal microbalance to monitor deposition rate and film thickness.

### 3.2.3 THERMALLY ASSISTED CONVERSION (TAC)

Once appropriate thicknesses of the desired TM are deposited, the TAC process, as described previously by Gatensby *et al.*<sup>94</sup> and O'Brien *et al.*<sup>76</sup>, can be utilised to transform the metal into the desired TMD. Though an extremely versatile fabrication technique applicable to many TMDs, the only TMD TAC film examined in this thesis was that of PtSe<sub>2</sub>.

Once Pt was deposited, the films\* of desired thickness were placed into the centre of a custom-built quartz-tube furnace (see right image in Fig. 3.1) with two heating zones. The tube was then evacuated and the samples were heated to 450 °C under 150 sccm forming gas (9:1 Ar:H<sub>2</sub>) flow in the high-temperature zone. A selenium (Se) precursor (solid pellets < 5 mm) was heated independently upstream in the furnace in the second (low-temp) zone (Sigma Aldrich, ≥ 99.99%), to ~250 °C, the Se-vapour was carried downstream to the Pt films for a duration of 2 hr to ensure selenisation of the surface. After a 30 min post-anneal at 450 °C in 150 sccm Ar, the furnace was subsequently cooled to room temperature. The forming gas helps to reduce surface oxidation of the metal film.<sup>172</sup> For the growth of selenide TMD films, the presence of H<sub>2</sub> is especially necessary as the selenium is not reactive enough on this temperature/pressure. Se combines with H<sub>2</sub> to form H<sub>2</sub>Se which is much more reactive with the transition metal film.<sup>173</sup> To minimise health risk from exposure to the selenium used in the growth of Se-TMDs, a solid Se precursor was utilised. In addition, a sealed ventilation box was placed over the furnace to prevent Se contamination from entering the lab atmosphere.

#### 3.2.4 CHEMICAL VAPOUR DEPOSITION (CVD)

The CVD synthesis method here was previously developed by O'Brien *et al.*<sup>93</sup> and was primarily used to synthesise monolayer (ML) TMDs in the dedicated sulfur furnace, such as MoS<sub>2</sub> and WS<sub>2</sub>. This technique can also be applied to selenide TMDs. The notable difference between the CVD and TAC processes is the TM precursor and growth substrate geometry. In CVD, all precursors are evaporated and the materials grown are high in crystallinity, whereas TAC produces polycrystalline thin films.

---

\*From atomic force microscope (AFM) measurements of the thicknesses of Pt layers before and after selenisation, it has been reported that the initial Pt thickness expands approximately four times after post-selenisation.<sup>96</sup> Henceforth, TAC film thicknesses will be referred to by their starting Pt thickness, unless otherwise stated.

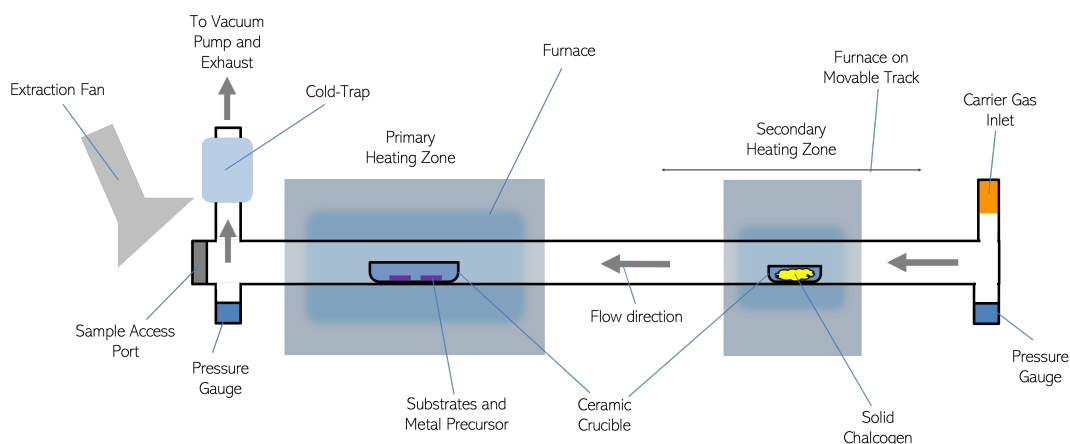


**Figure 3.2:** Schematic of the two-zone quartz furnace systems used for TMD synthesis in this thesis. Image courtesy of Dr. Conor Cullen.

For the CVD synthesis of TMDs, at least two precursors are necessary; one containing the metal and another containing the chalcogen. The options in chalcogen precursors are usually straightforward, with either  $\text{H}_2\text{S}/\text{H}_2\text{Se}$  or the vapourised chalcogen being used. Elemental selenium is usually favoured over  $\text{H}_2\text{Se}$  due to its lower toxicity.

The CVD method employs a microreactor geometry, where the growth substrate is brought into close proximity with the seed substrate containing the metal precursor (see Fig. 3.3). For  $\text{MoS}_2$ ,  $\text{MoO}_3$  dispersed in solution was dropcasted onto a  $\text{SiO}_2$  precursor substrate. Once the solvent is evaporated, a clean growth substrate was then placed face-down on the  $\text{MoO}_3$  precursor substrate. Similarly, for  $\text{WS}_2$ , a dropcasted solution of  $\text{Bi}_2(\text{WO}_4)_3$  dissolved in  $\text{NH}_3 \cdot \text{H}_2\text{O}$  (solvent baked off at  $100^\circ\text{C}$ ) was used in the microreactor. This stack/sandwich geometry allows allows a sufficient amount of sulfur vapour to intercalate between the wafers and react with the vaporised Mo precursor to generate  $\text{MoS}_2$  monolayers which then deposit on the growth substrate.

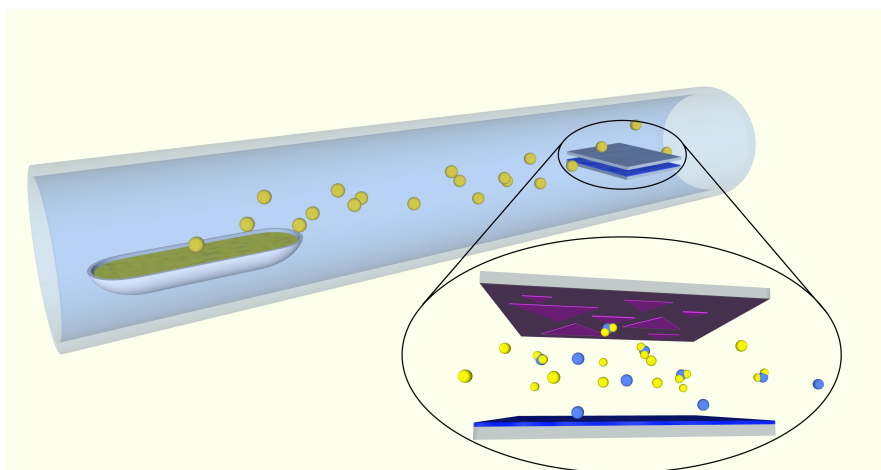


**Figure 3.3:** Schematic of the furnace setup used for CVD TMD synthesis in this thesis. On the left is the upstream low temperature zone where the chalcogen is evaporated (yellow) and carried downstream to the high temperature zone, on the right. A detailed close-up is shown of the microreactor with the bottom substrate as the seed layer containing the metal precursor (blue) and the resulting TMD growth on the top substrate. Image courtesy of Dr. John McManus.

### 3.2.5 MECHANICAL EXFOLIATION

Mechanical exfoliation (ME) and transfer are the most successful techniques to obtain high-quality single or few-layer crystalline materials from their native bulk structures, particularly for graphene and TMDs.<sup>82</sup> For this work, a custom mechanical transfer stage was built (see Fig. 3.4), based on the experimental setup outlined by Castellanos-Gomez *et al.*<sup>174</sup> To prepare samples with ME flakes on the substrate, PDMS stamps (Gel-Pak-4) were used in transferring the thinned flakes from Nitto/Scotch tape to the desired substrate using a transfer stage. Once the flakes had been transferred from the stamp to the substrate, the sample was annealed under Ar at 150 °C to ensure good adhesion, especially for spin-coating purposes.

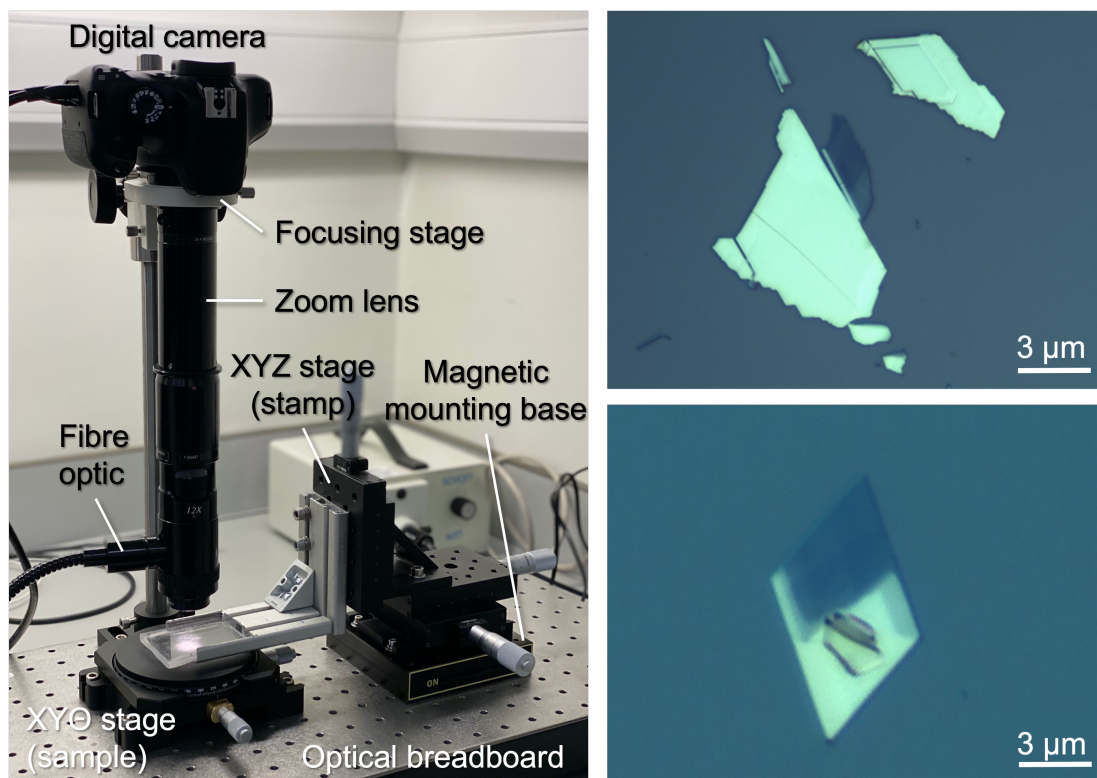


**Figure 3.4:** Left: photo of custom-built mechanical transfer apparatus. Right: optical microscope images of ME PtSe<sub>2</sub> flakes transferred onto a SiO<sub>2</sub>/Si substrate using this setup. Darker areas of flakes indicate very few layers.



### 3.3 LITHOGRAPHIC TECHNIQUES

#### 3.3.1 PHOTO & ELECTRON BEAM LITHOGRAPHY

To create samples that were suitable for electrical characterisation, lithographic techniques were necessary to create channel devices. Two approaches were used: UV photolithography (masked and maskless) and electron beam lithography (EBL).

UV lithography is the standard technique for integrated circuit (IC) fabrication. It involves UV light shining through a patterned mask onto a substrate spin-coated with a light-sensitive polymer called resist. The excess photoresist is removed by immersing the substrate in developer followed by rinsing in DI water. Positive photoresist becomes soluble in the developer whereas negative photoresist becomes insoluble after exposure to UV. The lithography tools used in this work were an OAI mask aligner situated in a Class 100 cleanroom and a maskless lithography setup, Intelligent micro patterning (IMP). The IMP operates by projecting a monochrome image onto the substrate, which can be aligned using the in-built microscope. This generally involved two steps in fabrication of TAC devices: first - markers and channels, and second - contacts (post-selenisation). For ME flakes, only the contacting step was required.

EBL is a powerful technique for creating patterns and nanostructures that are too small to fabricate using conventional photolithography, achieving resolutions up to a few nm. A highly focused beam of electrons is rastered over a sample, again spin coated with (electron sensitive) resist, to write out the desired pattern. The e-beam induces a change in the molecular structure of the resist, altering its solubility. This results in cross-linking in the case of negative tone resist and chain scission in the case of positive tone resist. Like photolithography, the substrate is immersed in developer to selectively dissolve either the exposed/unexposed areas of resist. Three steps were generally involved in



**Figure 3.5:** Photos of IMP tool used for maskless UV lithography.

fabricating the channel devices using EBL; markers, channels and then contacts post-selenisation. A Karl Zeiss Supra 40 field emission scanning electron microscope (FE-SEM)<sup>†</sup> and Raith Quantum software beam blanker and software were used. The samples were first spin-coated with a layer of e-beam sensitive resist, PMMA A6. The exposure areas were removed with a developer solution (IPA:MIBK 4:1).

For all techniques of device fabrication, positive resist was used to allow precise metal deposition. Once, the metal was deposited, the remaining resist was removed in lift-off step in acetone, leaving clearly defined channels and/or contacts.

---

<sup>†</sup>Scanning electron microscopy (SEM) is described in further detail in Section 3.4.5.

### 3.4 MICROSCOPIC TECHNIQUES

#### 3.4.1 ATOMIC FORCE MICROSCOPY (AFM)

For this project, the AFMs used were an Asylum Research Cypher and primarily a Bruker Multimode 8. The mode used to perform most topographical measurements was ScanAsyst-Air, a PeakForce tapping mode, similar to tapping mode but with the gain and setpoint constantly being re-adjusted automatically through a sophisticated real-time feedback loop, allowing optimal data to be collected whilst minimising noise. Typical probes used in topography measurements were ScanAsyst-Air (silicon nitride,  $k = 0.4 \text{ N/m}$ ,  $f_0 = 75 \text{ kHz}$ , Bruker) and SSS-NCH (etched silicon,  $k = 42 \text{ N/m}$ ,  $f_0 = 330 \text{ kHz}$ , Nanosensors). The subsequent images were analysed and their topographical profiles extracted using the Gwyddion software.

#### 3.4.2 NANOSHAVING/NANOMACHINING

Tips used to nanomachine/nanoshave were wear-resistant diamond with broad cone angles (NM-RC,  $k = 350 \text{ N/m}$ ,  $f_0 = 750 \text{ kHz}$ , Adama Innovations Ltd., see Fig. 2.7(b)). Prior to any AFM manipulation, the tip was underwent a contact mode force calibration to determine the deflection sensitivity of the cantilever. This involved performing a thermal tune followed by multiple ramps (i.e. force-distance curves) on a sapphire substrate (SAPPHIRE-12M, Bruker). From this, the inverse value of the AFM's optical lever sensitivity (InvOLS,  $\text{nm/V}$ ) was measured using the force curve slope on retraction, as previously outlined in Section 2.1.5. This process also gives a more accurate value for the spring constant,  $k$ .



Figure 3.6: Photos of the Bruker Multimode 8 AFM, showing several components and aspects of the system.

Once the shaving/machining tip was calibrated, the key operating parameters that determined the quality of nanomachining are:

1. Deflection setpoint
2. Scan speed.

2D TMD materials were nanomachined/nanoshaved at various scan speeds (10– 30  $\mu\text{m/s}$ ) and setpoints (0.01 – 0.5 V) to optimise parameters in contact mode using a Bruker Multimode 8.

### 3.4.3 KELVIN PROBE FORCE MICROSCOPY (KPFM)

As mentioned in Section 2.1.7, a bias can be applied either through the tip or the sample in KPFM. In this work, the bias was applied through the sample as the CPD images of higher potential translate to higher work function, and vice versa. For a sample-biased system, the work functions,  $\varphi$ , can be determined from the CPD as such:<sup>42</sup>

$$\begin{aligned}
 CPD &= V_{probe} = \frac{\varphi_{sample} - \varphi_{probe}}{|e|} \\
 \varphi_{probe} &= \varphi_{Au} - |e|CPD_{Au} \\
 \varphi_{sample} &= \varphi_{probe} + |e|CPD_{sample}
 \end{aligned}
 \tag{3.1}$$

Where  $e$  is the elementary charge.

PeakForce KPFM (PF-KPFM) was the primary KPFM mode used in this work on the Bruker Multimode 8. As mentioned in Section 2.1.7, PF-KPFM is a two pass mode that combines Bruker’s proprietary PeakForce tapping mode and standard FM-KPFM. Like other electrical AFM modes, samples were electrically connected directly to the chuck through silver paint (Agar Scientific) contact from the sample to its magnetic puck.

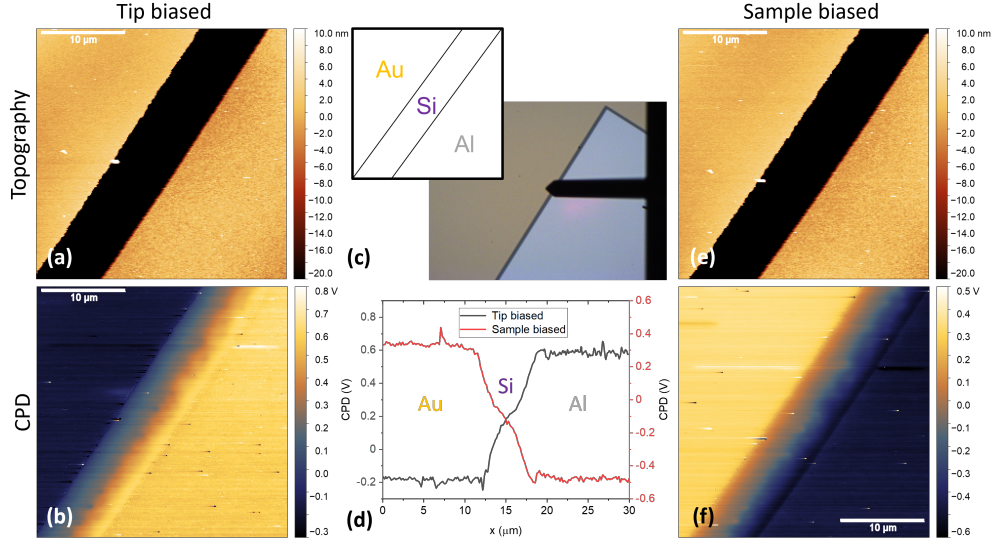


**Figure 3.7:** PeakForce Kelvin probe force microscopy calibration under different biases. (a) PF-KPFM topography and (b) corresponding surface potential map while tip biased. (c) Schematic and optical of KPFM calibration Au-Si-Al sample. (d) Contact potential difference (CPD) line profiles of tip biased (b, black) and sample biased (c, red) with corresponding material regions labelled. (e) PF-KPFM topography and (f) corresponding surface potential map while sample biased.

For all KPFM measurements throughout this work, three different electrically conductive probes were used:

- SCM-PIT-V2, antimony-doped Si,  $k = 3 \text{ N/m}$ ,  $f_0 = 75 \text{ kHz}$ , Bruker
- PFQNE-Al, silicon nitride,  $k = 0.8 \text{ N/m}$ ,  $f_0 = 300 \text{ kHz}$ , Bruker
- AD-2.8-AS, boron-doped single crystal diamond,  $k = 2.8 \text{ N/m}$ ,  $f_0 = 75 \text{ kHz}$ , Adama Innovations Ltd.

To calibrate the tips, a KPFM calibration sample (PFKPFM-SMPL, Bruker) was used (Fig. 3.7(c)), which is patterned with Au, Si, Al strips. Both the Au and Al films deposited are  $\sim 50 \text{ nm}$  in thickness on n-doped silicon substrate. A staircase potential profile is expected across the 3 different materials (see Fig. 3.7(d)). KPFM calibration measurements under sample bias were compiled for statistical purposes to produce Fig. 3.8(e).  $\varphi_{probe}$  was calculated using the work function of the Au strip  $\varphi_{Au}$

which is assumed to be 5.12 eV based on literature values.<sup>175–177</sup>  $\phi_{Au}$  is used in the probe calculations rather than  $\phi_{Al}$  as aluminium forms an oxide in ambient conditions, thus gold is more stable. From this,  $\phi_{probe}$  was determined to be  $5.31 \pm 0.27$  eV for SCM-PIT-V2,  $4.69 \pm 0.22$  eV for PFQNE-Al and  $5.50 \pm 0.20$  eV for AD-2.8-AS. In addition, the lift heights were optimised for each tip type prior to imaging. Optimal heights were determined to be 85 nm for SCM-PIT-V2, 40 nm for PFQNE-Al and 75 nm for AD-2.8-AS.

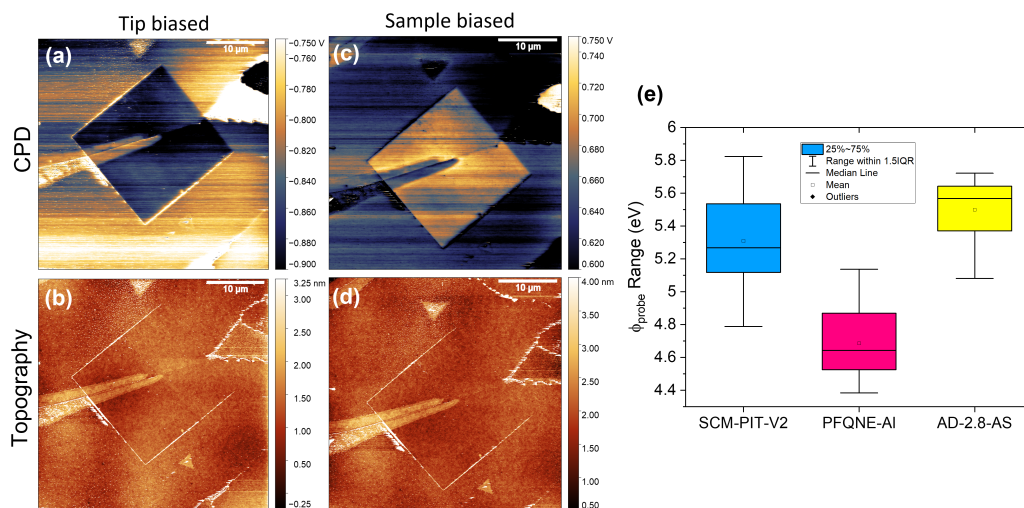


**Figure 3.8:** (a) and (c) show CPD maps under tip (a) and sample (c) bias of CVD-grown monolayer MoS<sub>2</sub> after nanoshaving, with their respective topographical images (b) and (d). (e) Calibrated work function ranges for probes using throughout this work.

### 3.4.4 CONDUCTIVE AFM

AFM conductivity measurements were carried out using the conductive PeakForce tapping mode, PF-TUNA, on the Bruker Multimode 8. Like other electrical AFM modes, samples were electrically connected directly to the chuck through silver paint (Agar Scientific) contact from the sample to its magnetic puck. The sample was biased at 1 V during measurements. The tips used were AD-40-SS ( $k = 40$  N/m,  $f_0 = 200$  kHz, Adama Innovations Ltd.) – super sharp (tip radius < 5 nm) conductive

single crystal diamond probes. To allow conductivity in the tip, the diamond coating is highly doped with boron leading to a macroscopic resistivity of 0.003–0.005  $\Omega$  cm.

### 3.4.5 SCANNING ELECTRON MICROSCOPY

The scanning electron microscope, was invented by Manfred von Ardenne in 1937.<sup>178</sup> It was the first microscope to achieve high magnification by scanning a very small raster with a finely focused beam of electrons. Although there had been some crude models before his, von Ardenne was the first to succeed in eliminating the chromatic aberration that had plagued previous electron microscopes. The SEM uses a focused beam of high-energy electrons to generate signals as their energy is dissipated at the surface of specimens. The signals that derive from electron-sample interactions contain information on topography and composition of a sample's surface.

Generally in SEM, data is collected over a selected surface area in a raster fashion and an image is generated. However, like the AFM, there are some limitations to the SEM. Firstly, the samples must be solid stable in a vacuum on the order of  $10^{-5}$  –  $10^{-6}$  torr. Any 'wet' samples, such as organic materials, decrepitate/outgas at low temperatures. Nevertheless these samples can be examined in a special 'environmental' SEMs at a relatively low vacuum. Also, an electrically conductive coating must be applied to electrically insulating samples for study in conventional SEMs to avoid charging effects, unless the instrument is capable of operation in a low vacuum mode.

The SEMs used in this thesis were Karl Zeiss Supra 40 for EBL and Karl Zeiss Ultra plus for general imaging. The Karl Zeiss Ultra plus was operated at 5 kV accelerating voltage, 30  $\mu$ m aperture and a working distance of typically 5 – 7 mm. Primarily, imaging was acquired using the secondary electron detector (SE2).



### 3.5 SPECTROSCOPIC TECHNIQUES

#### 3.5.1 RAMAN SPECTROSCOPY

Raman spectroscopy was carried out using a WITec Alpha 300R spectrometer with a 532 nm excitation laser, which was fitted with a Rayshield Coupler to detect Raman lines close to the Rayleigh line at  $0\text{ cm}^{-1}$ . Spectra were recorded using a laser power of  $< 100\ \mu\text{W}$  for  $\text{MoS}_2$  and  $\text{WS}_2$  and  $< 300\ \mu\text{W}$  for  $\text{PtSe}_2$  in order to minimise sample heating. A 100x objective with a numerical aperture (NA) of 0.95 and a spectral grating with 1800 lines/mm were used for all Raman spectra. Maps were generated by taking 4 spectra per  $\mu\text{m}$  in both x and y directions over large areas. The resulting data was analysed and the spectra were subsequently graphed using a combination of WITec Project FIVE and Origin Pro software.

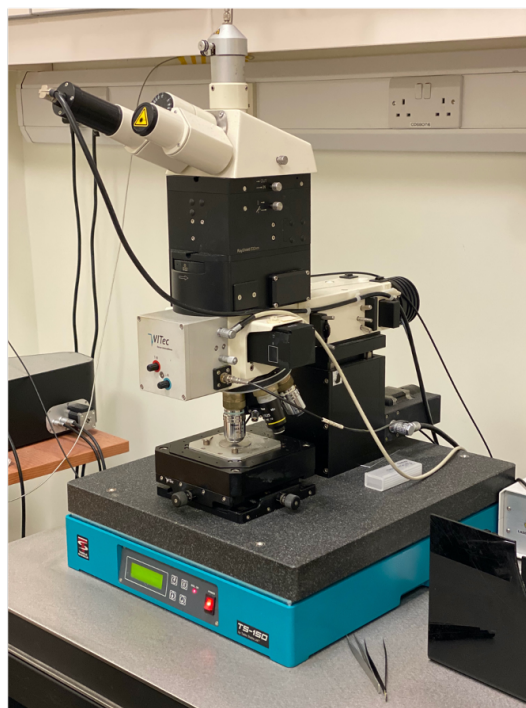


**Figure 3.9:** Photograph of WITec Alpha 300R scanning Raman and PL spectrometer used in this work.

#### 3.5.2 PHOTOLUMINESCENCE

In this work, all PL measurements and spectra were recorded using a WITec Alpha 300R at RT with a 532 nm laser as the excitation source. A 100x objective with a numerical aperture (NA) of 0.95 and

a spectral grating with 600 lines/mm were used for all PL measurements. Spectra were recorded using a laser power of  $< 100 \mu\text{W}$  for  $\text{MoS}_2$  and  $\text{WS}_2$ . Cold temperature PL measurements were carried out at 77 K. Maps were generated by taking 4 spectra per  $\mu\text{m}$  in both x and y directions over large areas. The resulting data was analysed and the spectra were subsequently graphed using a combination of WITec Project FIVE and Origin Pro software.

### 3.6 ELECTRICAL CHARACTERISATION

The  $\text{PtSe}_2$  TAC devices were fabricated using shadow-masked UVL and EBL to pattern the substrate in the desired geometry. Pt was deposited using e-beam evaporation and subsequently selenised using the TAC method. Contacts were deposited *via* e-beam evaporation, comprised of a 5 nm Ti (adhesion layer) with 45 nm Au on top. The ME  $\text{PtSe}_2$  flake devices were fabricated using maskless UVL. E-beam evaporation was employed to deposit contacts consisting of 5:45 nm Ti/Au. The electrical characterisation of the TMD devices was carried out in ambient conditions using a Karl Suss probe station connected to a Keithley 2612A source meter. The voltage was applied through needle-probes, contacting Au electrodes deposited on the TMDs. The measured current was collected and plotted automatically using Labview and Origin Pro software to give current-voltage (I-V) curves.

*All sorts of things can happen when you're open to new ideas  
and playing around with things.*

Stephanie Kwolek, chemist & inventor of Kevlar

# 4

## Patterning 2D Surfaces by Nanoshaving

### 4.1 INTRODUCTION

SCANNING PROBE MICROSCOPY (SPM) TECHNIQUES have been widely employed in the fabrication of nanostructures on a wide variety of surfaces.<sup>47-49</sup> One such technique is atomic force microscopy (AFM), a versatile tool that allows users to not only probe a samples' electrical, magnetic

and mechanical properties in a wide range of environments at very high resolution, but also to manipulate materials down to the nanometre scale.<sup>179,180</sup> Self-assembled monolayers (SAMs) have proved to be ideal resist materials for such physical manipulation and fabrication.<sup>50,104,181–183</sup> Nanoshaving is when an SPM tip is used to ablate a surface layer mechanically or electrochemically with a required normal force.<sup>50</sup> It differs from nanomachining as it selectively removes adsorbed layers (adlayers) rather than penetrating the sample surface.<sup>51</sup> Mechanical displacement, or nanoshaving of SAMs by an AFM probe is a relatively inexpensive technique, ideal for fundamental studies.<sup>50</sup>

Despite being highly researched materials for a wide range of applications, to date, there has been little exploration of the nanopatterning of SAMs on 2-dimensional (2D) materials using AFM. The versatile material removal applications of AFM make it an excellent candidate for investigating non-covalently functionalised 2D systems and it offers advantages over established techniques such as bottom-up approaches and focused ion beam (FIB) milling.<sup>52,184</sup> The AFM-based approach avoids problems related to ion-injection from FIB,<sup>185</sup> low resolution ( $\sim 300$  nm) of confocal Raman microscopy<sup>186</sup> and constraints on nanostructure size and shape due to mask limitations in bottom-up approaches.<sup>187</sup> AFM nanopatterning also enables data to be collected *in situ* during the nanoshaving/nanomachining process, giving insight into the mechanical properties of the material. The mechanical nature of the nanoshaving process is the root of its limitations. The SAM adsorbates (resist) should be selectively removed without substantially damaging the underlying 2D material. Different factors such as sample material, tip speed, applied force, tip angle, sliding direction, humidity and sample orientation affect how a material is removed.<sup>53</sup> Furthermore, AFM-based mechanical nanoshaving has the issue of ridge formation or the accumulation of materials around the inscribed features.<sup>54</sup>

Chemical functionalisation of layered 2D materials, such as graphene or transition metal dichalcogenides (TMDs), is essential in modifying their properties and expanding their capabilities

and applications.<sup>97</sup> Exploiting the functionalisation of TMDs is seen as a route to their widespread application of TMDs in photonics, energy storage and conversion, drug delivery and medical devices.<sup>98,99</sup> TMD surfaces tend to be rather inert to chemical functionalisation, due to saturation of basal plane chalcogen atoms.<sup>98,100</sup> Meanwhile, the metal sites sandwiched in between the chalcogen layers are rendered somewhat protected from functionalisation. Fortunately, TMDs have a tendency to be very sticky, as evidenced by the many organic groups that readily physisorb through electrostatic interactions to the electron-rich chalcogen surface atoms.<sup>98</sup> As has been previously shown for graphene, non-covalent functionalisation of 2D materials is an attractive strategy for altering their surface chemistry without damaging their electrical and mechanical properties.<sup>188–190</sup>

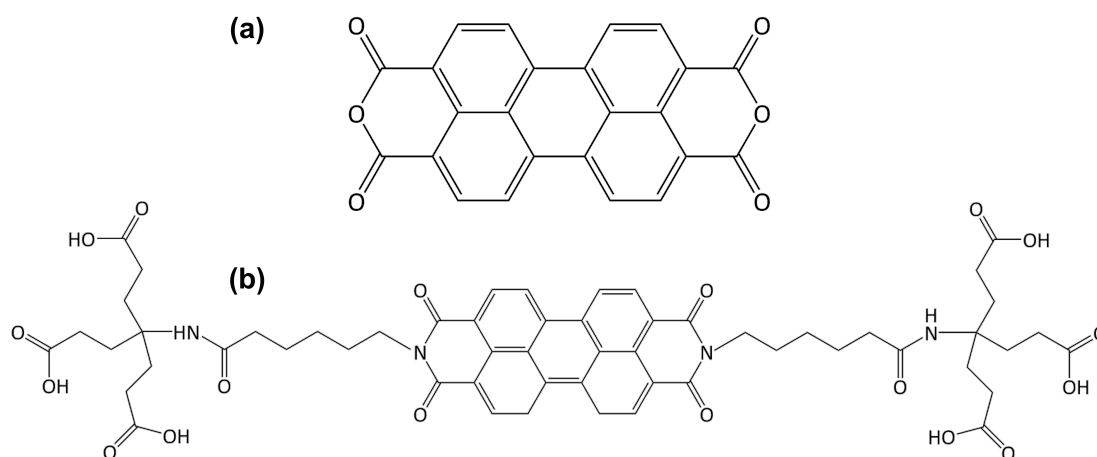


**Figure 4.1:** Chemical structures of (a) perylene-3,4,9,10-tetracarboxylic dianhydride (PTCDA) and (b) N,N'-substituted perylene-3,4:9,10-tetracarboxdiimide, a perylene diimide (PDI) derivative.

Würthner *et al.* outlined how perylene-based dyes have been implemented in many fields of technology due to their excellent physical and optical properties and their tendency towards self-assembly.<sup>191</sup> Perylene is a polycyclic aromatic hydrocarbon consisting of two bonded naphthalene molecules and its derivatives range from intense orange to red in colour.<sup>192</sup> Perylene-based  $\pi$ -surfactants can be ideally used as probes as they possess the characteristic

spectroscopic fingerprint features (absorption, emission, Raman) of both the aromatic dispersant and the respective carbon allotrope.<sup>193</sup> A key primary perylene is perylene-3,4,9,10-tetracarboxylic dianhydride (PTCDA, Fig. 4.1(a)), an organic semiconductor.<sup>194</sup> Peng *et al.* determined an increase of the electroactive surface area and superior conductivity in graphene with PTCDA as a surfactant.<sup>195</sup> However, one fundamental drawback of primary perylene and PTCDA is their intrinsic insolubility in organic solvents and water.<sup>193</sup>

Another perylene of interest in surfactant systems is N,N'-substituted perylene-3,4:9,10-tetracarboxdiimide,<sup>196</sup> a derivative of perylene diimide (PDI, Fig. 4.1(b)), which has been frequently used for the dispersion and stabilisation of carbon allotropes in aqueous solutions.<sup>193</sup> PDI-based molecules exhibit strong absorption through their large aromatic core, which can become attached to 2D layers via van der Waals (vdW) interactions.<sup>197-199</sup> Berner *et al.* previously investigated the packing density of PDI for the non-covalent functionalisation of single-layer graphene grown *via* chemical vapour deposition (CVD).<sup>188</sup> Depending on the presence of substrate contamination, the aqueous-phase deposition of PDI resulted in different packing densities of SAMs which were directly observed in scanning tunneling microscopy (STM). Wirtz *et al.* showed that perylene derivative SAMs can be used to improve adhesion to MoS<sub>2</sub>, acting as seeding layers for atomic layer deposition (ALD) oxides<sup>197</sup> while Kim *et al.* developed this methodology for the passivation of MoS<sub>2</sub> monolayer channels in FETs, significantly improving performance.<sup>99</sup> Additionally, Abellán *et al.* reported the formation of a protective layer with an electron-deficient PDI derivative which conferred black phosphorus flakes with considerable stabilisation against oxygen degradation.<sup>200,201</sup>

For any electronic material, a key parameter is the work function ( $\phi$ ), which is defined as the difference in energy level at vacuum and the Fermi energy ( $WF = E_{vac} - E_F$ )<sup>202</sup> and interprets how that material interacts when interfaced with other materials/elements. The work function also controls the charge transfer and transport across the interface, thus it is important to study the

electrostatic potentials of TMD/organic heterostructures and the effect of the organic layer in modulating the TMD work function.<sup>203</sup> Kelvin probe force microscopy (KPFM) has been used to characterise the charge distribution of various materials by measuring the surface potential/contact potential difference (CPD) between the AFM tip and sample surface.<sup>41</sup> It has been used to measure the contact resistance and potential drops in functionalised graphene<sup>204</sup> and bilayer MoS<sub>2</sub><sup>205</sup> between contacts under external bias conditions, as well as organic thin film transistors.<sup>206</sup> By engineering specific surface dipoles, the work function can be intentionally modified. Therefore, KPFM is a useful technique for characterising the charge transfer at the interface between 2D TMDs and non-covalent adlayers. One challenge with KPFM can be that adsorbed species from ambient air, such as water and carbon, change not only the topography but also the surface potential through charge transfer doping. Kahn discusses how exposure of the semiconductor surface to ambient air or other contaminants can affect work function, electron affinity and ionisation energy.<sup>202</sup>

When predicting the properties of interfaces between divergent materials, like organic SAM-inorganic 2D heterojunctions, it is helpful to examine these by way of an energy level diagram. For the SAM-2D case, the relevant energy levels are the highest occupied molecular orbital (HOMO) and lowest unoccupied molecular orbital (LUMO) vs. the 2D valence band maximum (VBM) and conduction band minimum (CBM).<sup>207</sup> The likely flow of charges in the ground and excited states can be predicted using this energy level alignment. This approach can also be used to identify potential SAM-2D material combinations for photovoltaic cells, photodetectors, diodes and other electronic and optical devices.

Dipoles and charges in SAM molecules can change the electronic structure of the 2D material in a similar manner to a gate voltage in a transistor, moving the 2D Fermi level ( $E_F$ ) up or down in energy.<sup>207</sup> Many commonly used organic SCs, such as planar phthalocyanines and perylenes, are neutrally charged with either small dipoles or no net dipole moment. In these systems, the movement of charge carriers is determined by hybridisation and ground state-charge transfer.<sup>207</sup>

Habib *et al.* reported that in PTCDA/MoS<sub>2</sub> heterojunctions, hybridisation mixes the S p<sub>z</sub> and Mo d<sub>z<sup>2</sup></sub> orbitals near the CBM and the conjugated C p<sub>z</sub> orbitals.<sup>208</sup> This hybridisation results in the narrowing of the MoS<sub>2</sub> bandgap and increases the density of states (DOS) near the band edges, resulting in a large intensity increase and a red shift in the PL spectrum. In addition, a net charge transfer occurs due to the enhanced DOS near the conduction band minimum (CBM) and overlapping of the excitonic energy levels in the heterostructure (see Fig. 4.2(b)). A similar type-II band alignment was also predicted by Obaidulla *et al.* (see Fig. 4.2(a)).<sup>209</sup>

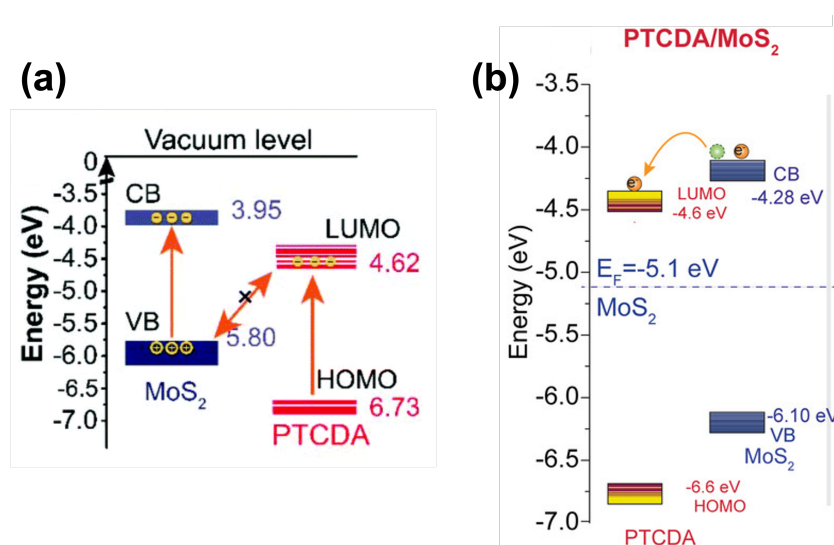


**Figure 4.2:** Previously reported Type-II band alignment illustrations for organic-inorganic heterostructures of PTCDA on MoS<sub>2</sub> by (a) Obaidulla *et al.*<sup>209</sup> and (b) Habib *et al.*<sup>208</sup>

This chapter investigates the work function change associated with the non-covalent functionalisation of monolayer TMDs with PDI SAMs, as measured by KPFM. The reversibility of such functionalisation is then examined through the approach of nanoshaving. Another perylene, PTCDA, which is chemically distinct from PDI, was deposited on the shaved areas to demonstrate non-covalent co-functionalisation of TMDs. A grating pattern was fabricated using nanoshaving as a lithographic technique. A diffraction grating was chosen as it is one of the most essential optical



components used in many academic and industrial areas<sup>210</sup> and is relatively simple in structure.

## 4.2 EXPERIMENTAL METHODS

### 4.2.1 CVD OF TMDs

MoS<sub>2</sub> and WS<sub>2</sub> samples were grown in a micro-cavity in a two-zone CVD furnace at 700 °C and 900 °C respectively, using the method outlined by O'Brien *et al.*<sup>93</sup> The MoS<sub>2</sub> samples were grown directly on SiO<sub>2</sub>/Si substrates (300 nm thick oxide layer, highly p-doped Si) with MoO<sub>3</sub> dropcasted from solution and sulfur as solid precursors for MoS<sub>2</sub>. A dropcasted solution of Bi<sub>2</sub>(WO<sub>4</sub>)<sub>3</sub> dissolved in NH<sub>3</sub>.H<sub>2</sub>O (solvent baked off at 100 °C) and sulfur served as precursors for WS<sub>2</sub>.

### 4.2.2 SURFACE FUNCTIONALISATION OF TMDs BY SAMs

Directly after TMD growth, perylene diimide (PDI, Fig. 4.1(b)) dissolved in aqueous buffer solution (1 mM) was deposited by dropcasting on the TMD for the functionalisation step. Post-shaving of PDI on MoS<sub>2</sub>, PTCDA (Fig. 4.1(a)) dissolved in dimethylformamide (DMF, 1 mM) was deposited on the MoS<sub>2</sub> in the same fashion as PDI.

### 4.2.3 AFM CHARACTERISATION & MANIPULATION

AFM nanoshaving and KPFM were performed in ambient conditions using a Bruker Multimode 8. All nanoshaving operations were carried out using nanomechanical diamond cone tips (NM-RC,  $k = 350$  N/m,  $f_0 = 600$  kHz, supplied by Adama Innovations Ltd.) in contact mode. The deflection sensitivity of the cantilevers was determined by performing force-distance curves pre-shaving on a sapphire substrate. For KPFM, the tips (SCM-PIT-V2 and PFQNE-Al, Bruker) were calibrated using a Au-Si-Al calibration sample (PFKPFM-SMPL, Bruker). To minimise possible topographical

artefacts, PeakForce KPFM (PF-KPFM), a two-pass (lift) mode, was used, where topographical data was recorded in the first pass. Then the tip was lifted to a user-specified distance above the sample surface ( $\sim 85$  nm for SCM-PIT-V<sub>2</sub>,  $\sim 45$  nm for PFQNE-A1), measuring the work function in the second pass. Raman and PL spectra were recorded using a WITec Alpha 300R with a 532 nm laser as the excitation source and a laser power of  $<100$   $\mu$ W, in order to minimise sample damage. A 100x objective with a numerical aperture (NA) of 0.95 and a spectral grating with 1800 lines/mm were used for all Raman spectra while a spectral grating with 600 lines/mm was used for all PL measurements. Maps were generated by taking 4 spectra per  $\mu$ m in both x and y directions over large areas.

### 4.3 RESULTS & DISCUSSION

The feasibility of removing perylene-based SAMs from the surface of monolayer TMDs *via* AFM nanoshaving was examined. CVD-grown MoS<sub>2</sub> samples on 300 nm SiO<sub>2</sub>/Si were prepared, along with one CVD-grown WS<sub>2</sub> sample. One sample remained as pristine MoS<sub>2</sub>, while others, including WS<sub>2</sub>, were functionalised with PDI. One MoS<sub>2</sub>/PDI sample was further functionalised with PTCDA post-nanoshaving.

Nanoshaving was carried out in a single pass contact mode on all samples in ambient conditions. Using the cantilever spring constant,  $k$ , and Hooke's Law, the contact force is defined as:

$$F_{tip} = kd \tag{4.1}$$

where  $d$  = deflection sensitivity (nm/V)  $\times$  deflection setpoint (V). It was found that damage of the underlying TMD monolayer began to be observed at loads  $> 1.5$   $\mu$ N. Nanoshaving at loads  $< 1$   $\mu$ N generally resulted in discontinuous and incomplete removal of material from the TMD surface. The

average load which resulted in the best nanoshaving was  $1.25 \pm 0.04 \mu\text{N}$ . This was sufficient to remove adsorbate molecules completely without causing damage to the TMD.

KPFM was employed to investigate and compare the shaved TMD, with and without functionalisation. In KPFM, a bias can be applied either through the tip or the sample. In this work, the bias was applied through the sample meaning that the CPD images of higher potential translate to higher work function, and vice versa. The work function is defined as the difference in energy between vacuum and Fermi energy levels ( $\varphi = E_{vac} - E_F$ ).<sup>202</sup> For a sample-biased system, the work functions,  $\varphi$ , can be determined from the CPD as such:<sup>42</sup>

$$\begin{aligned} CPD = V_{probe} &= \frac{\varphi_{sample} - \varphi_{probe}}{|e|} \\ \varphi_{probe} &= \varphi_{Au} - |e|CPD_{Au} \\ \varphi_{sample} &= \varphi_{probe} + |e|CPD_{sample} \end{aligned} \tag{4.2}$$

Where  $e$  is the elementary charge. Measurements were performed using Si cantilevers whose work functions ( $\varphi_{probe} = 5.31 \pm 0.27 \text{ eV}$  for SCM-PIT-V2,  $4.69 \pm 0.22 \text{ eV}$  for PFQNE-Al) were determined by calibration with a Au-Al reference sample.

#### 4.3.1 NANOSHAVING PRISTINE $\text{MoS}_2$

To investigate and characterise the molecular assembly and the effect of nanoshaving on such assemblies, the complementary techniques of KPFM, Raman and PL spectroscopies were used. Typical images acquired during KPFM imaging of  $\text{MoS}_2$  prior to nanoshaving are shown in Fig. 4.3(a) and (b), with topography measured on the first pass and surface potential measured on the second pass in a lift mode. For pristine  $\text{MoS}_2$ , apart from the accumulation of surface contaminants formed at the shaved area perimeter, there was a negligible decrease in the apparent

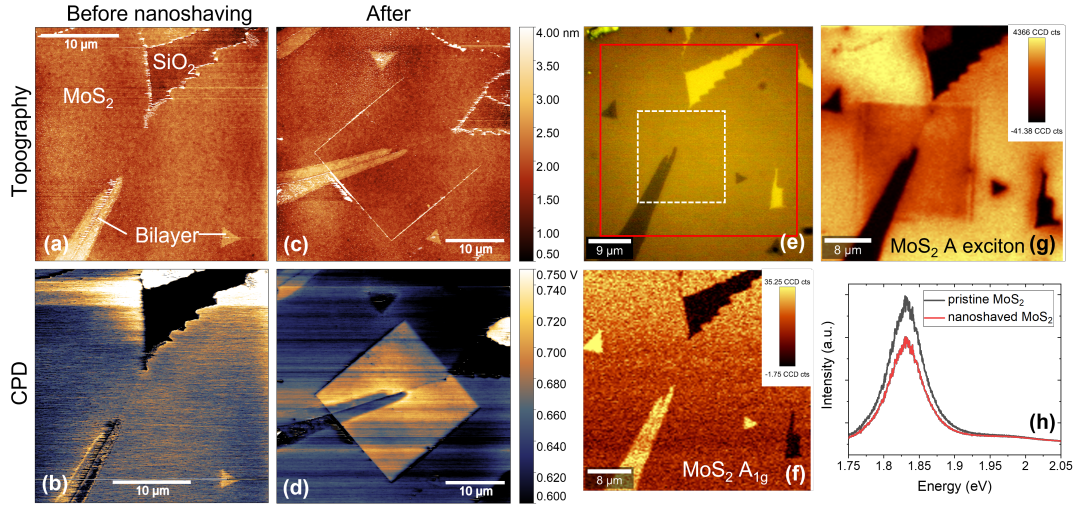


**Figure 4.3:** Nanoshaving of pristine MoS<sub>2</sub> — (a) and (c) show topography of the area of MoS<sub>2</sub> before and after nanoshaving, with their respective contact potential difference (CPD) images (b) and (d). (e) Optical image of the area scanned using Raman and PL spectroscopy (red box) with shaved area indicated by white dashed box. (f) Raman peak intensity map of MoS<sub>2</sub> A<sub>1g</sub> mode (405 cm<sup>-1</sup>). (g) PL peak intensity map of MoS<sub>2</sub> A exciton (1.83 eV) with (h) corresponding average spectra of pristine vs. shaved areas.

topographical height of the MoS<sub>2</sub> following nanoshaving (Fig. 4.3(c)). However, there is a significant contrast in the CPD between the nanoshaved and pristine areas of MoS<sub>2</sub>, with a slight increase of  $0.062 \pm 0.062$  eV for monolayer MoS<sub>2</sub> and  $0.034 \pm 0.63$  eV for the bilayer in this image. It should be noted that ridge formation of nanoshaved debris typically occurs on the perimeter of the shaving scan area, as seen in Fig. 4.3(c).

Pristine CVD-grown monolayer MoS<sub>2</sub> typically has Raman peaks observed at  $\sim 384\text{cm}^{-1}$  and  $\sim 405\text{cm}^{-1}$ , corresponding to in-plane ( $E_{2g}^1$ ) and out-of-plane ( $A_{1g}$ ) vibrational modes respectively (see Fig. A.1), when excited at 532 nm.<sup>145,149</sup> Monolayer MoS<sub>2</sub> on Si/SiO<sub>2</sub> also exhibits strong photoluminescence at room temperature from the A exciton at  $\sim 1.85$  eV (670 nm).<sup>149</sup> From Raman analysis of the area, it is clear in Fig. 4.3(f) there is no significant change in the peak intensity of the A<sub>1g</sub> mode from nanoshaving. There is also no significant shifting or broadening of the  $E_{2g}^1$  and A<sub>1g</sub> peaks (see Fig. A.1). Nevertheless, there was a slight decrease in intensity but no shift in position

of the PL signal of the A exciton at 1.83 eV (see Fig. 4.3(g) and (h)). This implies that the MoS<sub>2</sub> is being cleaned of surface contaminants and adsorbates during nanoshaving, rather than removal or destruction of the TMD monolayer.

#### 4.3.2 NANOSHAVING PDI ON MoS<sub>2</sub>

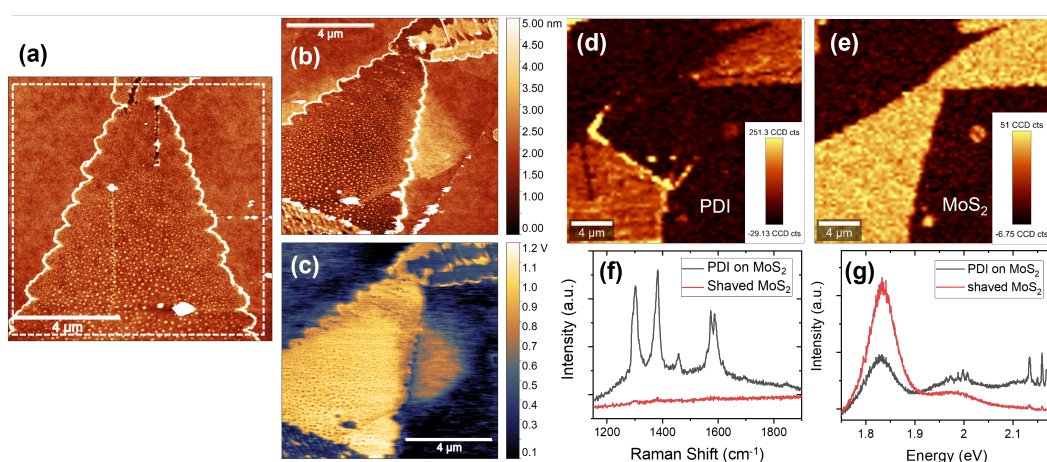


**Figure 4.4:** Nanoshaving PDI on MoS<sub>2</sub> — (a) topography of PDI functionalised MoS<sub>2</sub>. (b) topography and (c) CPD of nanoshaved PDI/MoS<sub>2</sub> area indicated by white dashed box in (a). (d) corresponding Raman peak intensity map of PDI (1300 cm<sup>-1</sup>) mode. (e) Raman peak intensity map of MoS<sub>2</sub> A<sub>1g</sub> (404 cm<sup>-1</sup>). (f) average Raman spectra of shaved and non-shaved areas, showing characteristic PDI peaks. (g) average PL spectra of shaved and non-shaved areas.

From AFM, the typical thicknesses of CVD-grown monolayer MoS<sub>2</sub> and WS<sub>2</sub> flakes were determined to be 0.7 nm and 0.75 nm respectively. After dropcasting PDI and rinsing with deionised (DI) water and isopropanol (IPA) to remove excess PDI molecules not directly bound to the TMD surface, the samples were examined using AFM/KPFM. The pristine MoS<sub>2</sub> monolayer step height before functionalisation is consistent with previously reported values.<sup>99,102,211</sup> Raman analysis shows that the PDI appears to self-assemble preferentially to the TMD surface rather than SiO<sub>2</sub> (see Fig. 4.4(d) and Fig. 4.10(c)), as previously observed in other studies.<sup>102,197</sup> The average

combined step height of monolayer MoS<sub>2</sub> functionalised with PDI SAM was 2 nm, indicating a thickness of  $\sim 1.3$  nm for the PDI SAM. This compares well to previously reported values.<sup>102</sup>

Fig. 4.4(a) shows the topography of a typical MoS<sub>2</sub> flake with a PDI overlayer. Nanoshaving PDI on MoS<sub>2</sub> resulted in a reduction of step height by  $\sim 1.2$  nm (the thickness of a PDI SAM) demonstrating nanoshaving's applicability for lithography. Fig. 4.4(c) shows significant contrast between the shaved and non-shaved areas with a difference in CPD of 490 mV, which equates to a reduction in the work function of pristine MoS<sub>2</sub> of  $0.49 \pm 0.03$  eV. This indicates that functionalisation of monolayer MoS<sub>2</sub> with PDI reduces the surface potential and thus the work function, possibly due to doping. This has been previously observed for the work function of chlorine-doped CVD-grown MoS<sub>2</sub>, where the doping reduced the  $\phi_{\text{MoS}_2}$  by 0.4 eV as measured by KPFM.<sup>212</sup>

The capability of nanoshaving as a lithographic technique is further confirmed by the near-complete absence of PDI's characteristic peaks in the Raman maps (Fig. 4.4(d)) and Raman and PL spectra (Fig. 4.4(f) and (g)). In the non-shaved areas, the characteristic signature for PDI molecules is clearly visible when resonantly excited at 532 nm (Fig. 4.4(f) and (g)). It should be noted the PDI signal is mostly absent on the SiO<sub>2</sub> substrate (except in areas of pileup), indicating that changes in step height above the substrate can be attributed to the SAM. The peaks at 1300 and 1380 cm<sup>-1</sup> are the in-plane ring 'breathing' modes, with the ring deformation occurring at 1457 cm<sup>-1</sup>. The 1585 cm<sup>-1</sup> doublet is C-C stretching mode and the additional peaks visible in Fig. 4.4(g) between 1.95 and 2.05 eV (2500 – 3000 cm<sup>-1</sup>) are overtones and combinations related to the first order vibrational modes.<sup>102,199,213,214</sup> The Raman map of the MoS<sub>2</sub> A<sub>1g</sub> mode ( $\sim 404$  cm<sup>-1</sup>) in Fig. 4.4(e) shows no damage to the TMD underlayer from nanoshaving. This is further confirmed in Fig. A.2 where there is no change (i.e. no broadening) in the FWHM of both the E<sub>g</sub> and A<sub>1g</sub> peaks. In Fig. 4.4(g), the pristine MoS<sub>2</sub> PL at 1.85 eV is significantly quenched upon addition of the PDI. This quenching of PL while in a heterostructure has been observed by Obaidulla *et al.* for a similar

configuration, N,N'-diphenyl-3,4,9,10-perylene-dicarboximide (PTCDI-Ph) on MoS<sub>2</sub>.<sup>209</sup> It was suggested that this effect was due to 'trap-like' states occurring at the hetero-interface, indicating separation of photogenerated electron-hole pairs, as well as less ordered morphology than PTCDI/MoS<sub>2</sub>. Nevertheless, the MoS<sub>2</sub> PL intensity can be somewhat recovered upon nanoshaving the PDI (Fig. 4.4(g)). This reversibility reaffirms nanoshaving as a suitable candidate for lithography of these systems.

#### 4.3.3 FURTHER PL ANALYSIS OF NANOSHAVED MoS<sub>2</sub> & PDI ON MoS<sub>2</sub>

To evaluate the effect of the adsorbed PDI layer on the PL spectrum of the combined system, the PL spectra were further analysed and split up into their components using Pseudo-Voigt fitting in Origin software. The Pseudo-Voigt function is an approximation for the Voigt function, which is a linear combination of Gaussian and Lorentzian functions and accounts for the thermal broadening of the natural Lorentzian line shape.

Fig. 4.5(a) shows the fitted PL spectra (originally from Fig. 4.3(h)) of pristine MoS<sub>2</sub> (bottom) and nanoshaved MoS<sub>2</sub> (top). In Fig. 4.5(a), we can see that the A exciton (A<sup>0</sup>) at ~ 1.83 eV decreases with intensity upon nanoshaving but the B exciton at ~ 1.95 eV remains the same. Neither appear to shift in energy but the ratio between the A<sup>0</sup> and B increases with nanoshaving from 0.04 to 0.05. There is a third component at ~ 1.78 – 1.82 eV, which is the formation of a negatively charged exciton or trion, due to interplay between the exciton and a charge carrier.<sup>171</sup> Previous reports suggest the trion (A<sup>-</sup>) recombination tends to dominate in mechanically exfoliated monolayer MoS<sub>2</sub> due to unintentional heavy n-type doping.<sup>171,215,216</sup> However, in these spectra, the neutral exciton A<sup>0</sup> dominates the signal peak ~ 1.83 eV, which strongly suggests that the excitons can recombine without forming trions due to less doping/excess carriers in the CVD-grown monolayer. With nanoshaving of as-grown CVD MoS<sub>2</sub>, the A<sup>-</sup> signal appears to decrease very slightly in

intensity. This combined with the slight quenching of the direct  $A^0$  recombination peak could be due to local compressive strain caused by nanoshaving,<sup>217</sup> and removal of adsorbates.<sup>218</sup>

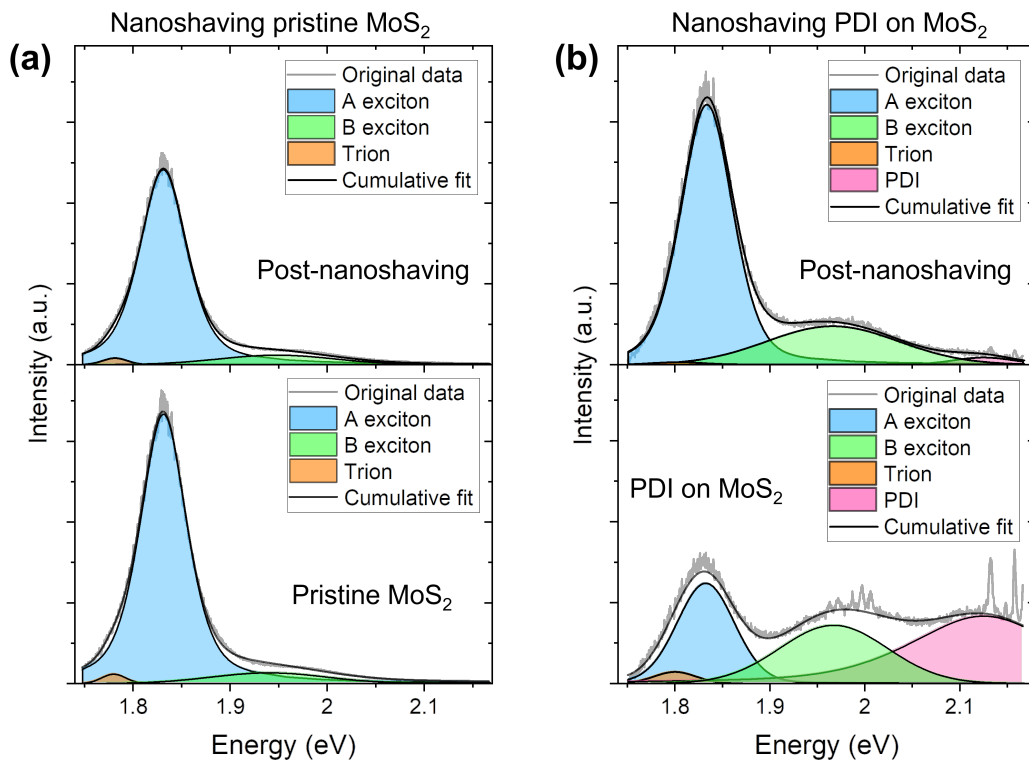


**Figure 4.5:** Fitted PL spectra of nanoshaved (top) and non-shaved (bottom) areas of (a) pristine  $\text{MoS}_2$  from Fig. 4.3(h) and (b) PDI on  $\text{MoS}_2$  from Fig. 4.4(g).

Fig. 4.5(a) shows the fitted PL spectra (originally from Fig. 4.4(g)) of PDI on  $\text{MoS}_2$  (bottom) and nanoshaved  $\text{MoS}_2$  (top). As previously mentioned, upon functionalisation of  $\text{MoS}_2$  with PDI, several Raman modes of the perylene molecules are distinctly visible at  $\sim 1300 - 1585 \text{ cm}^{-1}$  ( $\sim 2.13 - 2.18 \text{ eV}$ ), of which overtones are seen at lower energies ( $2500 - 3000 \text{ cm}^{-1}/1.96 - 2.02 \text{ eV}$ ) when excited at 532 nm. It should be noted, these distinct features are only visible on the surface of the TMD monolayer. PDI on the surface of the  $\text{SiO}_2$  substrate does not demonstrate any Raman



signal but produces a broad PL signal at  $\sim 2.12$  eV (see Fig. A.3). The enhanced PDI Raman modes arise from orbital overlap with the TMD band structure, resulting in band alignment and energy transfer under resonant conditions.<sup>209,219</sup> Furthermore, the enhancement of the B exciton ( $\sim 1.97$  eV) upon addition of PDI arises from the coupling of PDI's molecular excitons to the TMD excitonic states.<sup>220</sup>

If we examine the overall A exciton peak, we can see it is significantly quenched and also broadened (from 0.064 to 0.071 eV FWHM) by the PDI functionalisation. By including the PL from PDI on the SiO<sub>2</sub> (see Fig. A.3) in the peak model applied for pristine MoS<sub>2</sub> layers, the quenching and broadening can be attributed to a reduction in the A<sup>0</sup> exciton with an increase in the A<sup>-</sup> intensity. This reduction in the neutral exciton can be attributed to the introduction of trap-like states by the PDI adlayer and defects in the ordering on the MoS<sub>2</sub> surface.<sup>209</sup>

Though some evidence of PDI remnants on the MoS<sub>2</sub> monolayer upon nanoshaving is shown through the presence of the polyaromatic Raman modes ( $\sim 2.13 - 2.18$  eV), the PL emission of the nanoshaved area bears a resemblance to the spectrum of pristine MoS<sub>2</sub>. Firstly, the PL spectrum shows an almost complete reduction in the PDI Raman signal, as well as the coupled PDI signal at  $\sim 2.12$  eV. Secondly, the enhancement of the B exciton by PDI coupling is also somewhat reversed, with a reduction in relative intensity from 2.37 to 1.57 post-shaving. Thirdly, the quenching of the overall A exciton by PDI is also reversed with a significant increase in intensity of A<sup>0</sup>. In contrast, the trion A<sup>-</sup> is effectively quenched to beyond that of the unshaved pristine MoS<sub>2</sub>. A potential explanation of this effect could be the passivation of MoS<sub>2</sub> defects by non-covalent functionalisation with PDI before subsequent removal, as has been seen to occur with PTCDA as a SAM layer on 2D TMD surfaces.<sup>220</sup> However, to better observe the PL components, it is desirable to carry out measurements at lower temperatures (e.g. 77 K) to reduce non-radiative recombination effects on the spectrum.

#### 4.3.4 PATTERNING PDI ON $\text{MoS}_2$ *VIA* NANOSHAVING

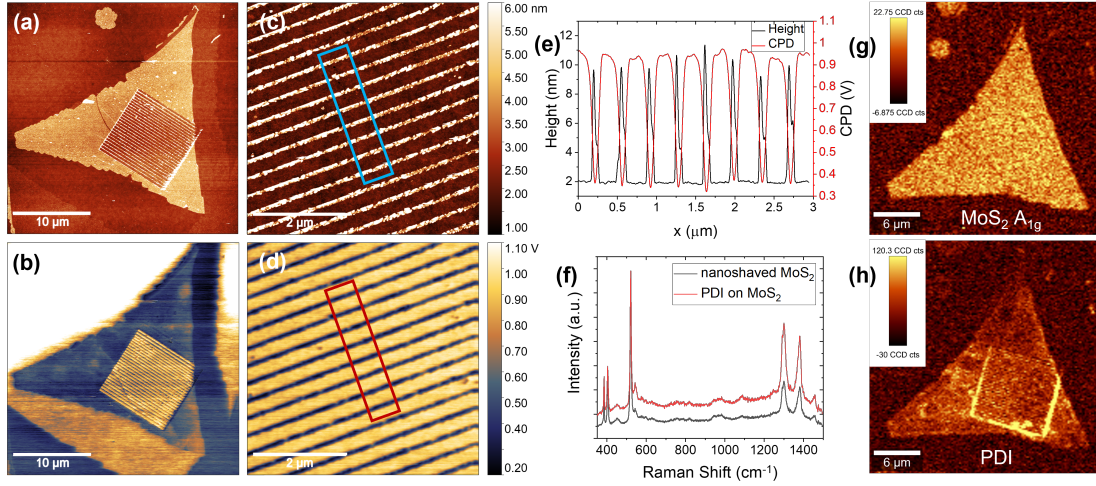


**Figure 4.6:** Nanoshaving grating pattern into PDI on  $\text{MoS}_2$  — (a) topography and (b) CPD of PDI-functionalised CVD  $\text{MoS}_2$  flake with nanoshaved grating pattern. (c) Topography and (d) CPD zooms of grating area showing uniformity. (e) Plot of height profile and corresponding potential profile (areas indicated in (c) and (d)). (f) average Raman spectra of shaved and non-shaved areas. Corresponding Raman peak intensity maps of (g)  $\text{MoS}_2$   $A_{1g}$  ( $400 \text{ cm}^{-1}$ ) and (h) PDI ( $\sim 1300 \text{ cm}^{-1}$ ) modes.

To demonstrate the applicability of this technique for lithography in these systems, a grating pattern was nanoshaved into the PDI/ $\text{MoS}_2$  (see Fig. 4.6(a)). This resulted in a remarkably uniform grating (Fig. 4.6(b)), consisting of a  $\sim 360 \text{ nm}$  pitch (250 nm trough, 110 nm peak). The average PDI pitch step height (Fig. 4.6(c)) is much higher ( $\sim 8 \text{ nm}$  above  $\text{MoS}_2$ ) compared to unpatterned PDI on  $\text{MoS}_2$ , most likely due to shaving debris pile-up. From KPFM in Fig. 4.6(d), the surface potential corresponds precisely to the topography, which is evident when overlaid in Fig. 4.6(e). It shows a relative surface potential or work function difference between the PDI lines and  $\text{MoS}_2$  of 600 mV or 0.6 eV, respectively, reaffirming the localised reduction in  $\phi_{\text{MoS}_2}$  due to PDI functionalisation. This selective removal is also visible in the Raman spectra, with Fig. 4.6(f) showing a clear reduction in intensity of the PDI vibrational modes ( $\sim 1300 \text{ cm}^{-1}$ ,  $\sim 1380 \text{ cm}^{-1}$  and  $\sim 1455 \text{ cm}^{-1}$ ). Nevertheless the PDI signal remains to some degree as the pitch is comparable with the laser spot size ( $\sim 300$

nm). Again, Fig. 4.6(g) shows the underlying MoS<sub>2</sub> to be undamaged and the parallel lines of PDI SAMs still adsorbed to the TMD surface (Fig. 4.6(h)). These results indicate that nanoshaving is a viable lithography technique introducing minimal contaminants, i.e. no resist necessary and without collateral damage to the SAM. In addition, nanoshaving could be suitable for the fabrication of other ordered optical/photonics structures, e.g. by rotating the sample 90°, a shaving pass of the same spacing parameters would produce a dot array.

#### 4.3.5 CO-FUNCTIONALISATION OF MoS<sub>2</sub>

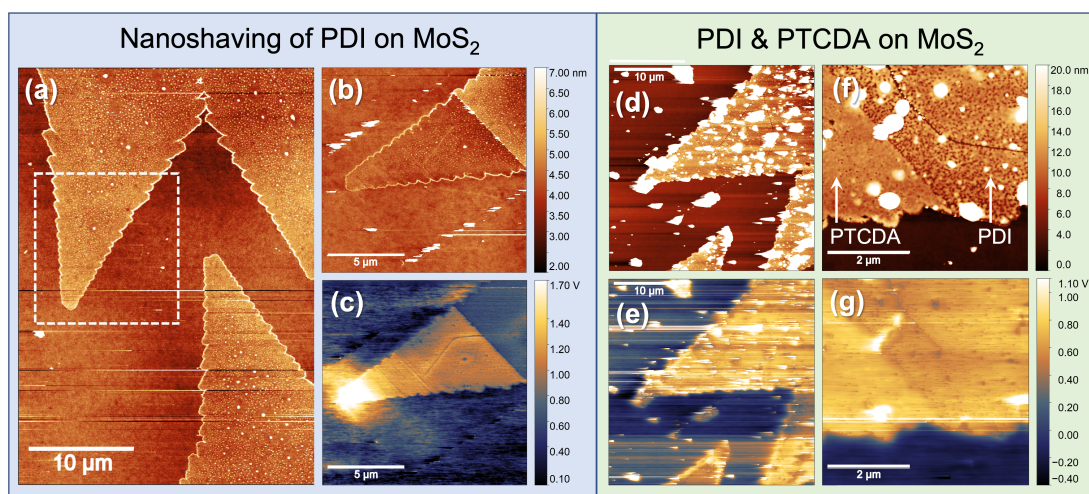


**Figure 4.7:** Co-functionalised MoS<sub>2</sub> — (a) Topography of PDI functionalised MoS<sub>2</sub>. (b) Topography and (c) CPD of nanoshaved PDI/MoS<sub>2</sub> area indicated by white dashed box in (a). (d) Topography and (e) CPD of area in (b) after deposition of PTCDA. (f) Topography and (g) corresponding CPD close-up of PTCDA/PDI boundary on MoS<sub>2</sub>.

A PDI/MoS<sub>2</sub> sample was further functionalised after nanoshaving with PTCDA to demonstrate chemically distinct non-covalent co-functionalisation of MoS<sub>2</sub>. For the sake of clarity, the KPFM will be compared and examined first, followed by comparison of the Raman/PL pre- and post-deposition of PTCDA.

Fig. 4.7(a) shows an AFM topography image of MoS<sub>2</sub> flakes functionalised with PDI. In Fig. 4.7(b),

KPFM of the area outlined in Fig. 4.7(a) is shown post-nanoshaving with the corresponding CPD image, Fig. 4.7(c). The step height from PDI to the nanoshaved area on MoS<sub>2</sub> is  $\sim 1.3$  nm, again consistent with previous SAM measurements.<sup>102</sup> Fig. 4.7(c) shows significant contrast between the shaved and non-shaved areas with a difference in CPD of  $390 \pm 150$  mV, which equates to an increase of  $0.39 \pm 0.15$  eV in the  $\phi$  of the PDI/MoS<sub>2</sub> heterostructure upon removal of PDI. Fig. 4.7(d) shows the topography of the same flake after dropcasting PTCDA and Fig. 4.7(e) shows the corresponding CPD image. Both images indicate that a PTCDA SAM has formed on the nanoshaved area of MoS<sub>2</sub>. The large particulates observed were later determined to be excess PTCDA and were removed following further rinsing in DMF. Fig. 4.7(f) and (g) show a close-up KPFM scan of the PDI/PTCDA boundary on the monolayer flake. The PTCDA appears to form a closer-packed and more homogenous SAM than the PDI. This is most likely due to cleaning of the MoS<sub>2</sub> surface with nanoshaving before deposition of PTCDA, whereas PDI was deposited on an as-grown surface with surface contaminants. This further demonstrates the capability of nanoshaving as a local surface cleaning technique. Additionally, sterics on the sidechains, like in PDI, will effect packing. Fig. 4.7(g) shows the CPD contrast between the two heterostructures, with  $\phi_{PDI/MoS_2} = 5.87 \pm 0.11$  eV and  $\phi_{PTCDA/MoS_2} = 5.96 \pm 0.10$  eV. The slightly increased surface potential and thus work function of the PTCDA/MoS<sub>2</sub> system can be attributed to the increased molecular order and packing density in the PTCDA SAM, which has previously been observed in KPFM of octadecyltrichlorosilane [OTS, CH<sub>3</sub>(CH<sub>2</sub>)<sub>17</sub>SiCl<sub>3</sub>] SAMs on oxidized Si(100) and polycrystalline silicon surfaces.<sup>221</sup>

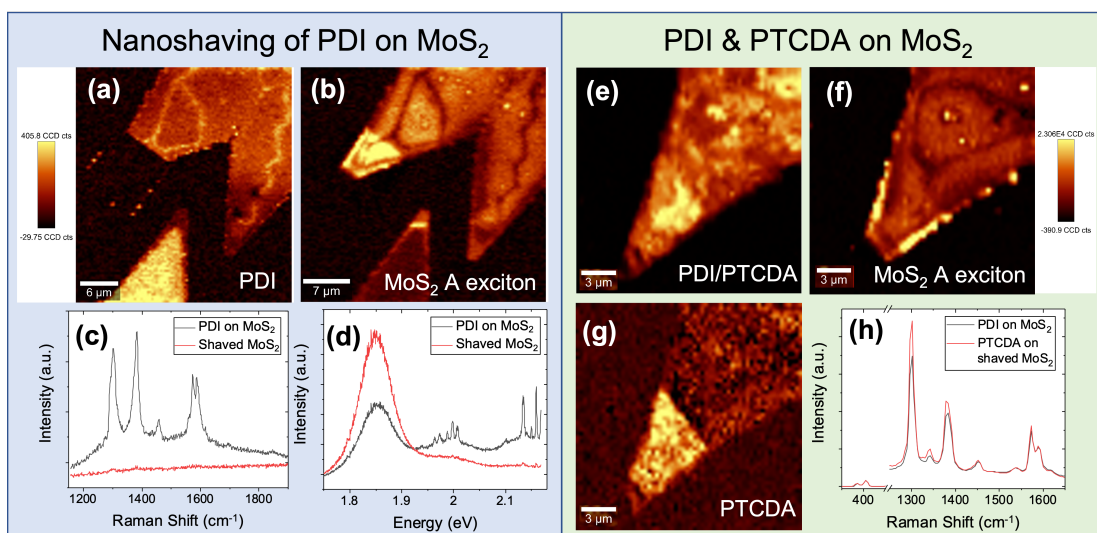


**Figure 4.8:** Co-functionalised MoS<sub>2</sub> — (a) Raman peak intensity map of PDI ( $\sim 1300\text{ cm}^{-1}$ ) mode. (b) PL peak intensity map of MoS<sub>2</sub> A exciton ( $\sim 1.85\text{ eV}$ ). (c) average Raman spectra of shaved and non-shaved areas, showing characteristic PDI peaks. (d) average PL spectra of shaved and non-shaved areas. (e) Raman peak intensity map of the combined degenerate breathing, ring distortion and Kekulé mode<sup>214</sup> of PDI and PTCDA ( $1300\text{ cm}^{-1}$ ) mode. (f) PL peak intensity map of MoS<sub>2</sub> A exciton ( $\sim 1.85\text{ eV}$ ). (g) Raman peak intensity map of PTCDA ( $\sim 1340\text{ cm}^{-1}$ ) mode. (h) Average Raman spectra of PDI and PTCDA functionalised areas, showing characteristic perylene peaks vs. the MoS<sub>2</sub> Raman peaks.

The non-covalent co-functionalisation of MoS<sub>2</sub> was further examined using the complementary optical techniques of Raman and PL. Like previous PDI shaving, the almost complete absence of PDI's characteristic peaks can be seen in the Raman map (Fig. 4.8(a)) and spectra (Fig. 4.8(c) and (d)), indicating that the SAM is fully removed by way of nanoshaving. In Fig. 4.8(b), the pristine MoS<sub>2</sub> PL at 1.85 eV is significantly quenched upon addition of the PDI. The PL spectra in Fig. 4.8(d) show the same features as described in Section 4.3.3 with the shaved and non-shaved areas. These reaffirm the KPFM measurements in demonstrating the almost complete removal of the PDI adlayer from the monolayer MoS<sub>2</sub> using nanoshaving.

As has been previously observed for PDI, the enhanced PTCDA Raman modes arises from orbital overlap with the TMD band structure, resulting in band alignment and energy transfer under resonant conditions.<sup>209,219</sup> Fig. 4.8(e) shows the Raman peak intensity map of the combined

degenerate breathing, ring distortion and Kekulé mode of the perylene core<sup>214</sup> at  $\sim 1300 \text{ cm}^{-1}$ , which is shared by both PDI and PTCDA. Fig. 4.8(f) also shows quenching the MoS<sub>2</sub> A exciton in the shaved area, similar to the quenching by PDI. In Fig. 4.8(g) a vibrational mode unique to PTCDA ( $\sim 1340 \text{ cm}^{-1}$ ) is mapped, along with the Raman spectra of the PDI and PTCDA functionalised areas in Fig. 4.8(h). All of these indicate the formation of a PTCDA SAM solely on the nanoshaved region of MoS<sub>2</sub>, thus demonstrating co-functionalisation of TMDs, while the PDI adlayer helps to passivate the other areas towards PTCDA assembly.

It should be noted that the PTCDA Raman signal is many orders of magnitude more intense than the MoS<sub>2</sub> E<sub>2g</sub><sup>1</sup> and A<sub>1g</sub> modes ( $\sim 384 \text{ cm}^{-1}$  and  $\sim 405 \text{ cm}^{-1}$ ), and the PDI modes (1300, 1380, 1457  $\text{cm}^{-1}$  and the doublet at 1585  $\text{cm}^{-1}$ ). This leads to any PTCDA contamination on the PDI SAM dominating the signal, hence the large overlap in spectra in Fig. 4.8(h) of the PDI and PTCDA SAMs.

#### 4.3.6 CHANGE IN WORK FUNCTIONS WITH NANOSHAVING & FUNCTIONALISATION

CPD measurements from all flakes were compiled for statistical purposes to produce Fig. 4.9(a) and (b), detailing the work function ranges for each of the parameters and the corresponding change in work functions from pristine CVD-grown MoS<sub>2</sub>. Nanoshaving pristine MoS<sub>2</sub> does not appear to significantly alter the work function while PDI seems to lower the pristine work function by  $\sim 0.45 \text{ eV}$ . In contrast, the addition of PTCDA on the nanoshaved MoS<sub>2</sub> appears to lower  $\phi_{\text{MoS}_2}$  by only  $\sim 0.23 \text{ eV}$ . The mean experimental  $\phi_{\text{PTCDA}/\text{MoS}_2}$  value of 5.62 eV, along with the mean  $\phi_{\text{MoS}_2}$  value of  $\sim 5.85 \text{ eV}$ , are comparable to the calculated work functions of 5.946 eV for pristine MoS<sub>2</sub> and 5.725 eV for PTCDA/MoS<sub>2</sub> heterostructure by Habib *et al.*<sup>203</sup> This theoretical  $\Delta\phi$  of 0.221 eV between pristine MoS<sub>2</sub> and the heterostructure is in strong agreement with the experimental  $\Delta\phi$  of 0.23 eV in this work. Habib *et al.* attributes this change in work function after introducing an

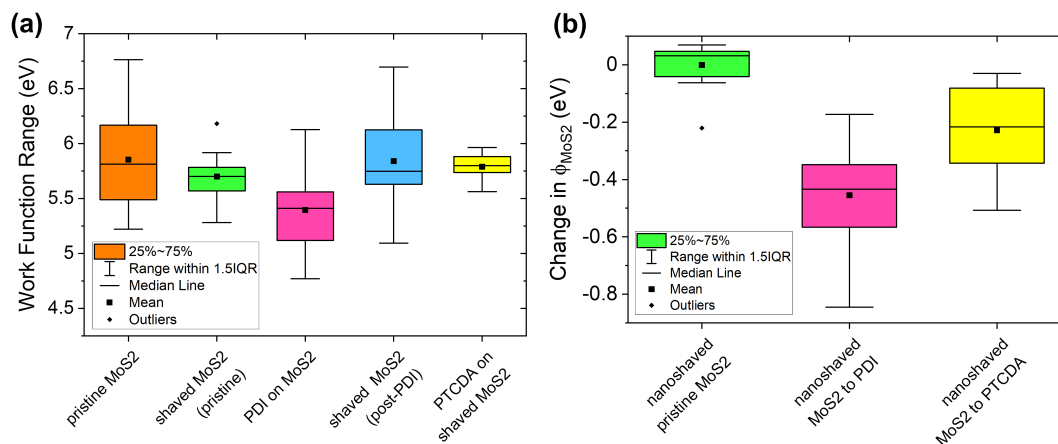


**Figure 4.9:** (a) Work function range as measured by KPFM. (b) change in work function from pristine MoS<sub>2</sub> with nanoshaving and non-covalent functionalisation.

organic over-layer on the inorganic surface to a chemical effect, the change in dipole moment at the interface due to charge rearrangement, adsorption induced bandbending effect at the interface and overlayer induced substrate relaxation.<sup>203,222–224</sup> The spread in CPD values between flakes and measurements in this work can in part be attributed to electrical isolation. However, as any potential offset should be the same on any single flake, a comparison can still be made to determine the difference in potential between shaved areas and non-shaved areas. This is providing that any changes in the state of the tip are accounted for through calibration, as was the case here.

A spread in work functions determined by KPFM is not unexpected as it is known that such values are highly sensitive to numerous factors including surface contamination, sample quality and grounding and experimental conditions (ambient in this case of this work). In literature, this leads to a relatively large spread in reported work function values of MoS<sub>2</sub> calculated from CPDs. Choi *et al.* investigated the layer-dependent work function of MoS<sub>2</sub> by way of surface potential measurements in KPFM.<sup>225</sup> The work functions of mechanically exfoliated (ME) 1, 2 to 6 layer MoS<sub>2</sub> were 5.15, 5.25 – 5.39 eV and increased with increasing layer number. After annealing, the flake work functions decreased by 0.1 – 0.2 eV due to the reduction in the amount of surface adsorbates.

Tamulewicz *et al.* examined the influence of flake-substrate effects on the work functions of mono to few layer ME MoS<sub>2</sub>, with values ranging from 4.84 eV for monolayer, 4.89 eV for bilayer to 4.99 eV for 5 layer.<sup>226</sup> In contrast, Habib *et al.* calculated the work function for pristine ML MoS<sub>2</sub> to be 5.946 eV,<sup>203</sup> which is very comparable to the mean experimental  $\varphi_{\text{MoS}_2}$  value in this study of  $\sim 5.85$  eV. While still within range of the former two studies, 5.85 eV is relatively high in comparison with the aforementioned values. One explanation might be the fabrication methods: mechanically exfoliated flakes (top-down) vs. CVD-grown monolayers (bottom-up), though a more in-depth comparison study is needed.

#### 4.3.7 NANOSHAVING PDI ON WS<sub>2</sub>

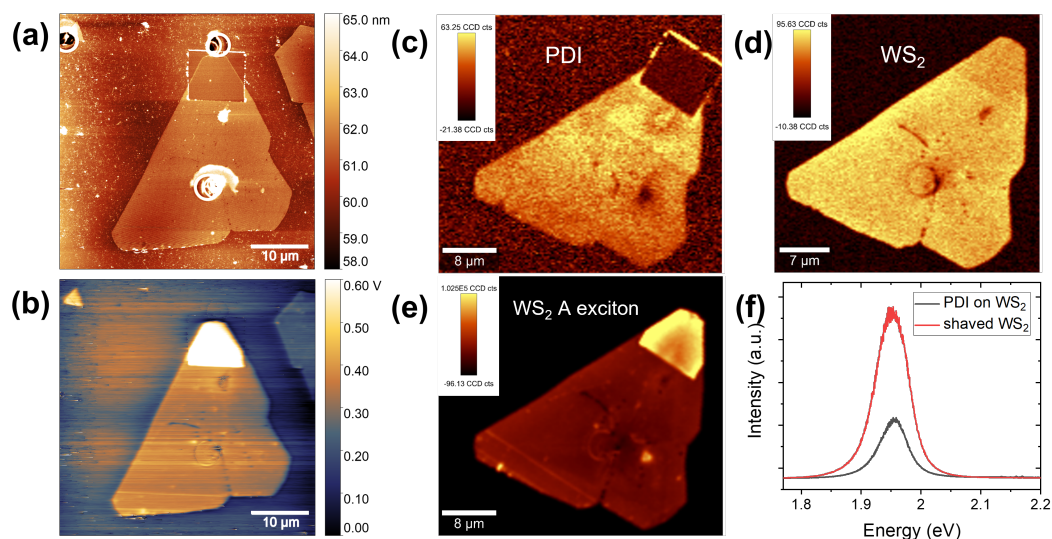


**Figure 4.10:** Nanoshaving PDI on WS<sub>2</sub> — (a) topography and (b) CPD of nanoshaved PDI functionalised WS<sub>2</sub>. Raman peak intensity maps of (c) PDI (1300 cm<sup>-1</sup>) and (d) WS<sub>2</sub> 2LA(M) + E<sub>2g</sub><sup>1</sup> mode (352 cm<sup>-1</sup>). (e) PL peak intensity map of WS<sub>2</sub> A exciton (1.95 eV) with (f) corresponding average spectra of functionalised vs. shaved areas.

To demonstrate that these methods could be applied to different TMD systems and not just limited to MoS<sub>2</sub>, PDI was deposited on WS<sub>2</sub> (in the same fashion as MoS<sub>2</sub>) and an area of flake was



subsequently nanoshaved (Fig. 4.10). The average load applied was 1.08  $\mu\text{N}$ , slightly less than the average load of 1.25  $\mu\text{N}$  used on PDI/MoS<sub>2</sub>. As previously mentioned, the step height of pristine CVD-grown WS<sub>2</sub> monolayer was determined to be 0.75 nm by AFM. Upon addition of PDI, the step height of the heterostructure was measured to be  $\sim 1.9$  nm (Fig. 4.10(a)), similar to PDI/MoS<sub>2</sub> and comparable to previous observations.<sup>197</sup> The contrast in CPD between nanoshaved and non-shaved areas is clearly visible in Fig. 4.10(b), with a difference of  $\sim 400$  mV, equating to a reduction in  $\phi_{\text{WS}_2}$  of 0.4 eV, from an average  $\phi_{\text{WS}_2} = 6.13$  eV to  $\phi_{\text{PDI/WS}_2} = 5.73$  eV. Like MoS<sub>2</sub>, the mean pristine WS<sub>2</sub> work function is much higher ( $\sim 1$  eV) than than previously reported values.<sup>227-229</sup> However, our observation of  $\phi_{\text{WS}_2} > \phi_{\text{MoS}_2}$  is in agreement with literature values.<sup>228,229</sup>

The complete removal of PDI was further confirmed by Raman analysis in Fig. 4.10(c). Pristine WS<sub>2</sub> exhibits a characteristic peak at 352  $\text{cm}^{-1}$ , which, when excited at 532 nm, is a combination of several different modes (see Fig. A.4). Of these, the most intense are the in-plane vibrational mode ( $E_{2g}^1$ ) and the resonantly excited  $2\text{LA}(M)$  phonon mode.<sup>145,151</sup> This intense peak can be seen in Fig. 4.10(d) indicating negligible damage from nanoshaving PDI to the underlying WS<sub>2</sub> monolayer. Pristine monolayer WS<sub>2</sub> also exhibits a strong RT PL response at  $\sim 1.95$  eV, which can be seen in Fig. 4.10(e). As seen for MoS<sub>2</sub>, the significant quenching of WS<sub>2</sub> PL by functionalisation with PDI is observed in Fig. 4.10(f). This quenching effect of PDI is even more substantial in WS<sub>2</sub> than in MoS<sub>2</sub>, which warrants further investigation.

#### 4.4 CONCLUSIONS

Non-covalent functionalisation of monolayer TMDs, MoS<sub>2</sub> and WS<sub>2</sub>, on Si/SiO<sub>2</sub> with organic SAMs of PDI was explored. These organic-inorganic heterostructures were manipulated using the

novel approach of nanoshaving and the reversibility of such functionalisation was investigated using the complementary non-destructive techniques of KPFM and Raman spectroscopy. Nanoshaving pristine monolayer TMD flakes had negligible effect on the topography but KPFM showed contrast in CPD between the shaved and non-shaved areas, most likely due to clearing of surface contaminants. It was shown that PDI selectively forms SAMs on TMD surfaces rather than Si/SiO<sub>2</sub>. A grating pattern with feature sizes < 250 nm was successfully shaved into the PDI/MoS<sub>2</sub> heterostructure, demonstrating the high-resolution capabilities of nanoshaving as a lithographic technique. In addition, non-covalent co-functionalisation of MoS<sub>2</sub> was demonstrated using PTCDA SAMs on previously nanoshaved areas.

*We need to go back to the discovery, to posing a question, to having a hypothesis and having kids know that they can discover the answers and can peel away a layer.*

Shirley Ann Jackson, physicist & first black woman to  
earn a Ph.D. from MIT

# 5

## Nanomachining PtSe<sub>2</sub>

### 5.1 INTRODUCTION

THE RELENTLESS PURSUIT OF LAYERED transition metal dichalcogenide (TMD) materials derives from their unique properties, from semimetals to semiconductors, for use in 2D-based electronics.<sup>64,67,230,231</sup> Recently, considerable interest has grown in group X TMDs, referred to as

noble-metal-based TMDs (NTMDs).<sup>77,232-234</sup> Their properties differ from the more widely studied group VI TMDs, such as dichalcogenides of Mo and W, due to the fact that, in NTMDs, all d-orbitals are filled, resulting in a  $d^2sp^3$  hybridisation.<sup>235</sup> Hence, NTMDs form a thermodynamically stable octahedral 1T phase (Fig. 5.1), unlike more commonly studied TMDs, which tend to form a stable trigonal prismatic 2H-phase.<sup>62,81</sup> The electron-rich, non-bonding d-orbitals result in stronger coupling between the two  $p_z$  bands of two adjacent intermolecular chalcogen atoms, leading to the extraordinarily strong interlayer interactions with nearly isotropic in-plane and out-of-plane mechanical interlayer coupling.<sup>81</sup> In the case of PtSe<sub>2</sub>, this makes it challenging to isolate monolayer PtSe<sub>2</sub> micromechanically from bulk crystals.<sup>236</sup> In addition, the interlayer breathing force constant, which describes the interlayer coupling, is calculated to be 2.5 times larger than that of graphene.<sup>146</sup>

However, the isolation of mono- and bilayer PtSe<sub>2</sub> is of utmost interest for 2D-based electronics as it shows layer-controllable semimetal to (indirect) semiconductor transition.<sup>72,73,231,238</sup> The monolayer (ML) has been reported as having an indirect band gap of 1.2 – 1.6 eV with the bilayer (BL), also indirect, of  $\sim 0.8$  eV.<sup>75-78</sup> This quantum confinement (number of layers) enables modulation of its electronic structure resulting in a tuneable bandgap.<sup>60,64,231,238</sup> Moreover, PtSe<sub>2</sub>'s band structure can be modified by external influences such as electric fields,<sup>235</sup> doping,<sup>239</sup> defect engineering<sup>240</sup> and mechanical forces<sup>236,241,242</sup>.

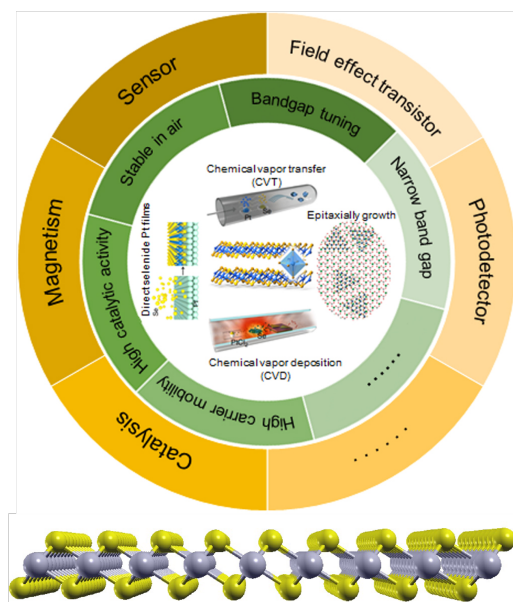


**Figure 5.1:** Summary of applications, properties and synthesis of PtSe<sub>2</sub>.<sup>237</sup> Below, three-dimensional schematic representation of a PtSe<sub>2</sub> (1T) monolayer structure, with selenium (Se) atoms in yellow and platinum (Pt) atoms in grey.

PtSe<sub>2</sub> has attracted much interest as a potential candidate for many applications, including field-effect transistors (FETs),<sup>79,96</sup> optoelectronics,<sup>243,244</sup> catalysis<sup>245,246</sup> and chemical and piezoresistive sensors.<sup>80,247,248</sup> Zhao *et al.* reported that few-layer PtSe<sub>2</sub> FETs exhibit high electron mobility at room temperature (RT) ( $\sim 210 \text{ cm}^2 \text{ V}^{-1} \text{ s}^{-1}$ ) on SiO<sub>2</sub>/Si substrate.<sup>79</sup> Nevertheless calculations predict significantly higher mobilities of  $\sim 4000 \text{ cm}^2 \text{ V}^{-1} \text{ s}^{-1}$  for PtSe<sub>2</sub> at RT.<sup>78</sup> In addition, PtSe<sub>2</sub> remains stable in air over elongated periods of time.<sup>79</sup>

Despite such progress in the research of NTMDs, challenges still remain, particularly in the understanding of the synthesis and properties of NTMD thin films. Precise control over the material dimensions, while simultaneously maintaining high material quality, is paramount to the study and understanding of thickness-dependent properties. In addition, given its application potential, investigating large-scale production methods in line with standard semiconductor back-end-of line (BEOL) processing is key to meeting future industrial integration needs.<sup>96,249</sup> Although high-quality few layer PtSe<sub>2</sub> flakes can be micromechanically exfoliated from bulk crystals,<sup>79,250–252</sup> the lack of scalability of the approach makes them only suitable for fundamental studies. Besides the top-down methods of mechanical exfoliation (ME) and liquid-phase exfoliation (LPE),<sup>235</sup> thin films of PtSe<sub>2</sub> have been fabricated *via* a range of bottom-up techniques such as thermally assisted conversion (TAC),<sup>72,76,96,231,247,253–255</sup> chemical vapour deposition (CVD)<sup>233,256–258</sup> and molecular beam epitaxy (MBE).<sup>259</sup>

Controlled physical modification of NTMDs is key to investigating their fundamental properties for use in numerous nanotechnology-based applications. As discussed in Chapter 4, scanning probe microscopy (SPM) techniques have been widely employed in the fabrication of nanostructures particularly on 2D materials, which AFM being the technique in this work. While nanoshaving selectively removes adsorbed layers (adlayers),<sup>51</sup> nanomachining is when a sufficiently stiff SPM tip is used to ablate a surface mechanically with a required normal force, removing materials locally from

the sample.<sup>50,52</sup> This technique has been exploited in a wide variety of studies, such as fabricating complex arrays of 3D nanodots on polycarbonate samples,<sup>260</sup> nanochannels of varying depth in silicon,<sup>261</sup> ferroelectric structures<sup>52</sup> and investigating the depth distribution of nitrogen-vacancy (NV) centers formed in an irradiated diamond surface.<sup>262</sup> AFM nanomachining also enables data to be collected *in situ* during the nanoshaving/nanomachining process, giving insight into the mechanical properties of the material.

Again, as previously discussed in Chapter 4, the mechanical nature of the nanomachining process is the root of its limitations. The limiting factor in creating reproducible patterns is the stability of the tip, which is prone to deformation and contamination from debris of the removed material,<sup>47</sup> and ridge formation or the accumulation of materials around the inscribed features.<sup>54</sup>

In terms of NTMDs, ML PtSe<sub>2</sub> is relatively robust in nature as its structure changes negligibly under biaxial tensile deformation,<sup>75</sup> making it a suitable candidate for nanomachining, particularly with its layer-dependent electronic structure. While ML and BL 1T-PtSe<sub>2</sub> are indirect SCs, bulk and few layer 1T-PtSe<sub>2</sub> exhibit semi-metallic in behaviour, making it a very interesting candidate for the possibility of 'self-contacting' FETs, i.e. where the semiconducting channel and contacts are made of the same material, simplifying the devices.

A major obstacle in the development and integration of practical 2D electronic and optoelectronic devices which must be addressed is that of reliable, low-resistance electrical contacts to 2D materials.<sup>130</sup> It has been shown that large contact resistances can occur between TMD channels and bulk metal contacts, significantly reducing the efficiency of current flow.<sup>131</sup> Regardless of the electrode material used, it requires the transmission of electrons through the interface between two different crystal lattices, which always causes a contact resistance due to reflections, Schottky barriers and scattering at the interface.<sup>132</sup> Low contact resistance in 2D SC devices is crucial for achieving high 'on' current, large photoresponse<sup>133</sup> and high-frequency operation.<sup>134</sup> Nevertheless, the chemical interaction at the metal-SC interface governs everything for 2D materials. Pristine surfaces

of 2D materials (i.e. no dangling bonds) hinder formation of any interface bonds with a metal, thus increasing contact resistance.<sup>135</sup>

As it is difficult for metals to covalently bond with pristine 2D material surfaces, a van der Waals (vdW) gap forms at the interface, acting as an additional tunneling barrier for the charge carriers, in addition to any innate Schottky barrier.<sup>130,136</sup> This extra barrier reduces the charge injection from metals, which leads to higher contact resistance. By reducing this vdW tunnel barrier as well as optimising edge contacts with all layers of the 2D material to produce a more seamless contact design, the contacts can be significantly improved with reduced resistance.

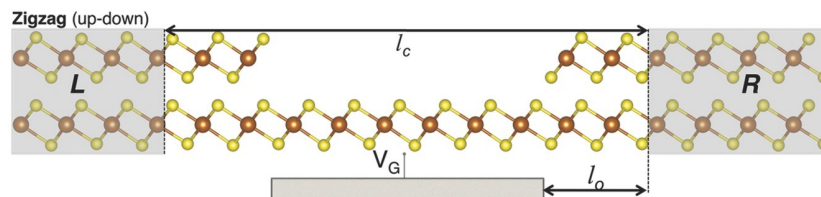


**Figure 5.2:** Schematic representation of a PdS<sub>2</sub> diode, consisting of a BL/ML/BL junction, with sulfur (S) atoms in yellow and palladium (Pd) atoms in brown.<sup>132</sup>  $l_c$  and  $l_o$  refer to the channel and overlap lengths.

An alternative to conventional metal contacts has been proposed *via* phase-engineering whereby a single-layer 2H MoS<sub>2</sub> transistor was contacted with metallic 1T MoS<sub>2</sub>.<sup>263</sup> However, 1T MoS<sub>2</sub> is metastable and reconverts to the 2H phase at room temperature (RT), thus negating the electrodes and device. Similarly, a single-material, ultrathin device based on 1T PdS<sub>2</sub> was proposed theoretically by Ghorbani-Asl *et al.*,<sup>132</sup> which consisted of a logic junction based on ML (band gap of  $\sim 1.1$  eV) and BL (semimetallic) PdS<sub>2</sub> (Fig. 5.2). It was shown that for channel lengths  $l_c \geq 2.45$  nm, the leakage current becomes negligible; any shorter and the junctions show tunnel diode characteristics. The concept is very attractive for energy efficient electronics as the whole device is built on a single flake and crystal plane, resulting in low contact resistance and sustainability (only one material used).<sup>132</sup> As PtSe<sub>2</sub> has similar properties to PdS<sub>2</sub>, a device based on a PtSe<sub>2</sub> channel and contacts

constructed in this manner should be possible with appropriate fabrication methods.

## 5.2 EXPERIMENTAL METHODS

### 5.2.1 THERMALLY ASSISTED CONVERSION (TAC) DEVICES

For thermally assisted conversion (TAC) of platinum to platinum diselenide, the platinum metal thin films were deposited by physical vapour deposition (PVD) onto Si/SiO<sub>2</sub> substrates with a 300 nm oxide layer. Three methods of PVD were used to deposit a controlled thickness of Pt; sputtering, electron beam evaporation and molecular beam epitaxy (MBE). The sputter coater used was a Gatan Precision Etching and Coating System (PECS) with a MaTeck Pt target. For e-beam evaporation of Pt, a Temescal FC-2000 Evaporation System was used. Both sputtering and e-beam evaporation use a quartz crystal microbalance to monitor deposition rate and film thickness.

Growth of Pt thin films were carried out in a DCA M600 MBE system with a base pressure of  $5 \times 10^{-10}$  Torr on a variety of Al<sub>2</sub>O<sub>3</sub> growth substrates; c-plane sapphire and amorphous alumina. The substrates were annealed under vacuum for  $\sim 2$  hours prior to deposition. Pt was deposited at 600 °C. The thin films were subsequently selenised *via* the TAC method.

Once appropriate thicknesses\* of Pt were deposited, the thermally assisted conversion (TAC) process, as described previously by O'Brien *et al.*<sup>76</sup>, was utilised to transform the metal into the TMD, PtSe<sub>2</sub>.

Lithographic techniques were used to create channel devices for electrical characterisation (see Fig. 5.3). Two approaches were used: photolithography (UVL) and electron beam lithography

---

\*From atomic force microscope (AFM) measurements of the thicknesses of Pt layers before and after selenisation, it has been reported that the initial Pt thickness expands approximately four times after post-selenisation.<sup>96</sup> Henceforth, TAC film thicknesses will be referred to by their starting Pt thickness unless explicitly stated otherwise.



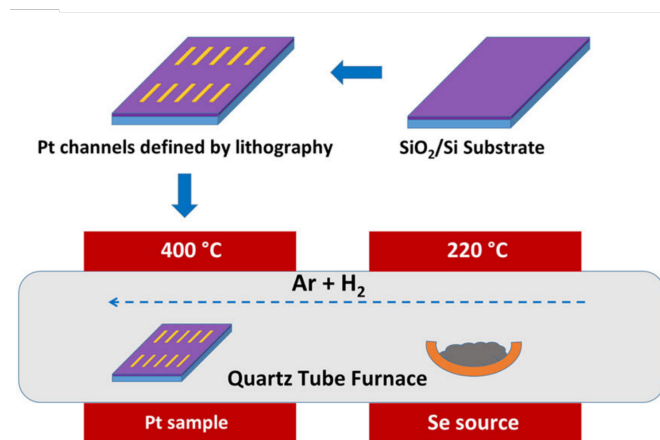


Figure 5.3: Schematic of the fabrication of PtSe<sub>2</sub> thin film channels via TAC.<sup>96</sup>

(EBL). The lithography tool used was an OAI mask aligner situated in a Class 100 cleanroom. This generally involved two steps in fabrication: first - markers and channels, and second - contacts (post-selenisation). Three steps were generally involved in fabricating the channel devices using EBL; markers, channels and then contacts post-selenisation. For both techniques of device fabrication, positive photo resist was used to allow precise metal deposition. Once, the metal was deposited, the remaining resist was removed in a lift-off, leaving clearly defined channels and subsequently contacts.

### 5.2.2 MECHANICALLY EXFOLIATED (ME) DEVICES

To prepare samples with ME flakes on the substrate, polydimethylsiloxane (PDMS) stamps (Gel-Pak-4) were used in transferring the thinned flakes from scotch tape to SiO<sub>2</sub>/Si substrates using a transfer stage. Substrates were pre-patterned with Au coordinates for ease of EBL/UVL. Once the flakes had been transferred from the stamp to the substrate, the sample was annealed under Ar at 150 °C to ensure good adhesion for spin-coating purposes. Devices were fabricated using maskless UVL as described in Section 3.3. Ti/Au contacts (5/45 nm) were deposited on the ME flakes to create a two terminal device.

### 5.2.3 CHARACTERISATION & MANIPULATION

AFM topography and nanomachining were performed in ambient conditions using an Asylum Research Cypher and a Bruker Multimode 8. TAC films and ME flakes were nanomachined at different scan speeds and setpoints to optimise parameters using a Bruker Multimode 8. All nanomachining operations were carried out using wear-resistant nanomechanical diamond cone tips (NM-RC,  $k = 600 \text{ N/m}$ ,  $f_0 = 600 \text{ kHz}$ , supplied by Adama Innovations Ltd.) in contact mode. The deflection sensitivity of the cantilevers was determined by performing force-distance curves pre-shaving on a sapphire substrate. All KPFM and PF-TUNA measurements were carried out using SCM-PIT-V2 probes from Bruker which are electrically conductive and coated with PtIr. For KPFM, the tips were calibrated using a Au-Si-Al calibration sample (PFKPFM-SMPL, Bruker). To minimise possible topographical artefacts, PeakForce KPFM (PF-KPFM), a two-pass (lift) mode, was used, where topographical data was recorded in the first pass. Then the tip was lifted to a user-specified distance above the sample surface ( $\sim 85 \text{ nm}$  for SCM-PIT-V2), measuring work function in the second pass. Samples were also electrically connected directly to the chuck through silver paint (Agar Scientific) contact from the sample to its magnetic puck. The subsequent images were analysed and their topographical profiles extracted using the Gwyddion software.

Raman spectroscopy was carried out using a WITec Alpha 300R spectrometer with a 532 nm excitation laser, which was fitted with a Rayshield Coupler to detect Raman lines close to the Rayleigh line at  $0 \text{ cm}^{-1}$ . Spectra were recorded using a laser power of  $< 300 \mu\text{W}$  in order to minimise sample heating. A 100x objective with a numerical aperture (NA) of 0.95 and a spectral grating with 1800 lines/mm were used for all Raman spectra. Maps were generated by taking 4 spectra per  $\mu\text{m}$  in both x and y directions over large areas. The resulting data was analysed and the spectra were subsequently graphed using a combination of WITec Project FIVE and Origin Pro software.

Electrical characterisation was performed in ambient conditions using a Karl Suss probe station connected to a Keithley 2612A source meter. The voltage was applied through needle-probes, contacting Au electrodes deposited on the TMD films/flakes. The measured current was collected and plotted automatically using Labview and Origin Pro software to give current-voltage (I-V) curves.

### 5.3 RESULTS AND ANALYSIS

#### 5.3.1 NANOMACHINING TAC PtSe<sub>2</sub>

PtSe<sub>2</sub> thin films were grown using the TAC process described in Section 3.2.3 whereby a Pt film on SiO<sub>2</sub>/Si was reacted with Se vapour at elevated temperatures in a low-pressure environment. As previously mentioned in Section 5.2.1, TAC film thicknesses will be referred to by their starting Pt thickness. The post-selenisation expansion factor is approximately four times the deposited thickness of Pt.<sup>96</sup> These films were characterised by AFM (see Fig. 5.4), which revealed their polycrystalline nature. The roughness (root mean square, RMS) of 3 nm converted PtSe<sub>2</sub> film was determined to 3.4 nm.<sup>†</sup>

Blanket films were imaged using tapping mode (Fig. 5.4(a)) to examine the region prior to nanomachining. Then a 1 × 1 μm area was machined while in contact mode at a predetermined setpoint of 280 mV and scanspeed of 3.9 μm/s. From Fig. 5.4(b), it is clear that the setpoint was too high and thus the PtSe<sub>2</sub> film was completely removed down to the SiO<sub>2</sub>, resulting in a large pile-up of material (Fig. 5.4(d)). It would seem the oxide layer was also partially machined as the post-selenisation thickness would be ~ 12 nm and the machining depth was ~ 15 nm (Fig. 5.4(c)).

---

<sup>†</sup>These images were produced using a broad angle diamond nanomachining tip, hence the ‘haloing’ effect on the topographical AFM images.

Another test was conducted whereby the setpoint was gradually increased by 100 mV per 100 nm of nanomachining (scanspeed remained constant at 3.9  $\mu\text{m/s}$ ) shown in Fig. 5.4(e). The resulting line profile (Fig. 5.4(f)) indicates a clear correlation between increasing setpoint and nanomachining depth, with  $\sim 1$  nm of material removed per 100 mV increase.

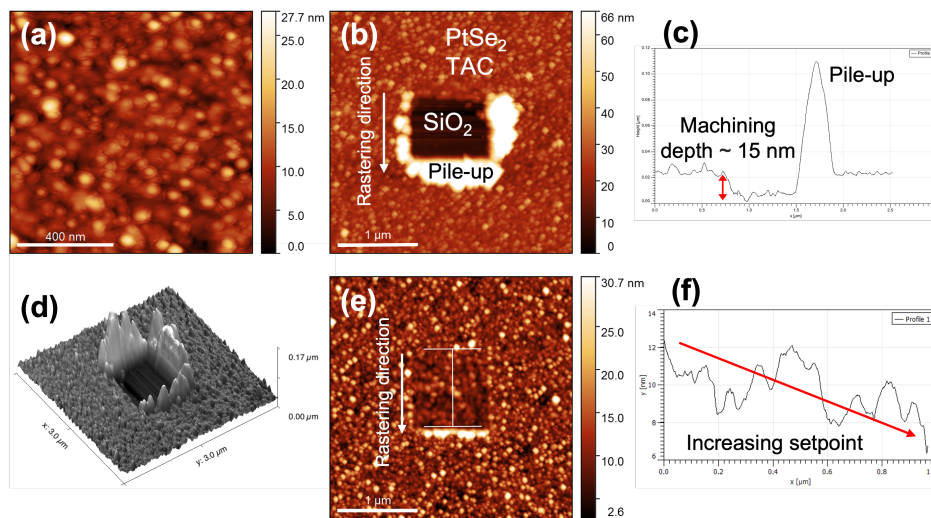


**Figure 5.4:** (a) Topographical image of 3 nm PtSe<sub>2</sub> TAC film. (b) TAC film post-nanomachining (5  $\mu\text{N}$  load, 20  $\mu\text{m/s}$  tip velocity). Arrow indicates rastering direction during machining. (c) Line height profile of machined region indicating a machining depth of  $\sim 15$  nm. (d) 3D rendered image of (b) showing pile-up. (e) Post-nanomachining with incrementally increasing setpoint. Line indicates height profile. (f) Averaged height profile of machined region in (e) indicating increasing machining depth with increasing setpoint.

## NANOMACHINING EBL-DEFINED TAC CHANNEL DEVICES

SiO<sub>2</sub>/Si substrates were patterned using EBL to create an array of channel devices with channel widths of 1000, 800, 500, 200 nm. 3 nm Pt was then sputtered and subsequently selenised *via* TAC. Topographical AFM line profiles determined the post-selenisation thickness to be  $\sim 12$  nm. Contacts were patterned, again using EBL, whereby 5:35 nm Ti:Au was then evaporated onto the substrate. Channels were nanomachined at a variety of scanspeeds (1 – 40  $\mu\text{m/s}$ ) and setpoints

(10 – 500 mV) to optimise parameters.

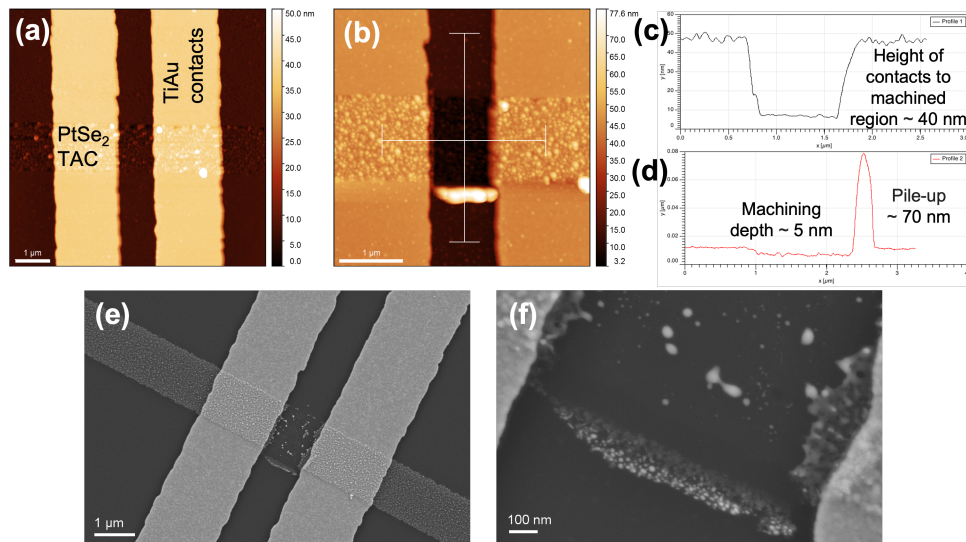


**Figure 5.5:** (a) Topographical image of 3 nm PtSe<sub>2</sub> EBL TAC channel (width 1000 nm) between TiAu contacts. (b) TAC channel post-nanomachining (3.8 μN load, 20 μm/s tip velocity). (c) Line height profile of machined region between contacts indicating a contact height to machining depth of ~ 40 nm. (d) Line height profile normal to the channel showing ~ 5 nm machining depth. (e) SEM of channel post-nanomachining. (f) Zoom of machined region in (f) showing complete removal of channel in some areas.

The first channel (Fig. 5.5(a)) was nanomachined normal to the channel length (Fig. 5.5(b)), leading to pile-up in between the contacts. Here the setpoint was deemed too high at 3.8 N, resulting in almost complete removal of the film. The topographical line profile in Fig. 5.5(c) (indicated by the white line normal to the TiAu contacts in Fig. 5.5(b)) shows the height of the contacts relative to the machined surface to be ~ 40 nm, further confirming the removal of the 12 nm TAC film. In Fig. 5.5(d), the topographical profile (indicated by the white line parallel to the TiAu contacts in Fig. 5.5(b)) the machining depth is ~ 5 nm, with a pile-up being ~ 70 nm in height, both relative to the SiO<sub>2</sub> surface. Fig. 5.5(e) and (f) are both SEM images of the machined channel, showing the removal of the PtSe<sub>2</sub> TAC channel.

The inter-contact pile-up in Fig. 5.5(b) could have potentially lead to shorting the device, thus, for

the subsequent channel (Fig. 5.6(a)), the machining procedure was rotated by  $90^\circ$  (Fig. 5.6(b)). In addition, the setpoint was reduced to 2.6 N, resulting in a thinner smoother TAC film with a reduction in RMS roughness from 2.55 nm pre-machining to 1.16 nm.

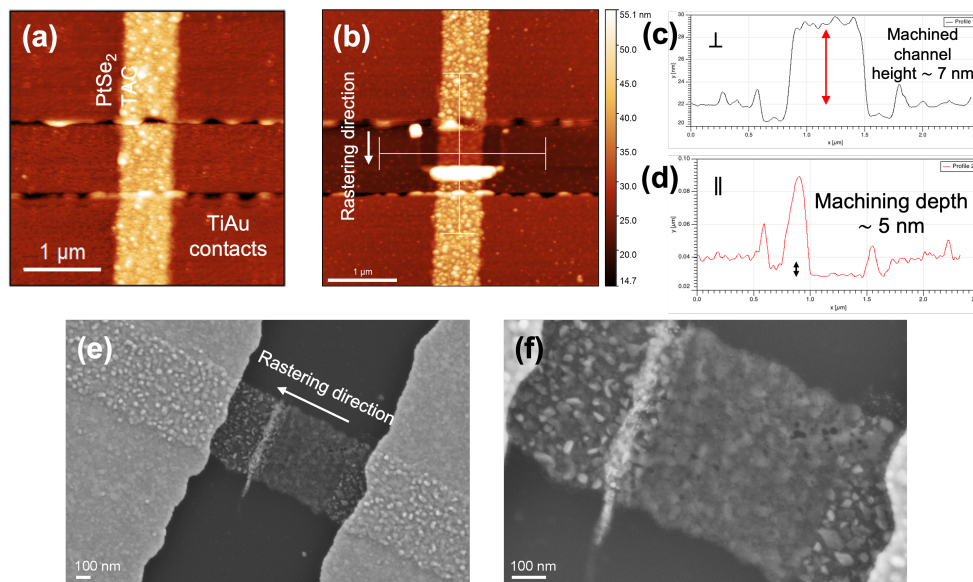


**Figure 5.6:** (a) Topographical image of 3 nm PtSe<sub>2</sub> EBL TAC channel (width 800 nm) between TiAu contacts. (b) TAC channel post-nanomachining (2.6  $\mu$ N load, 20  $\mu$ m/s tip velocity). (c) Line height profile normal to the channel showing  $\sim$  8.5 nm machined channel height. (d) Line height profile along channel indicating  $\sim$  5 nm machining depth. (e) SEM of channel post-nanomachining. (f) Zoom of machined region in (f) showing machined channel.

Fig. 5.6(c) shows the line profile (indicated by the white line normal to the PtSe<sub>2</sub> channel in Fig. 5.6(b)) of the machined channel of  $\sim$  7 nm, indicating a height reduction of  $\sim$  5 nm. In Fig. 5.6(d), the topographical profile (indicated by the white line parallel to the PtSe<sub>2</sub> channel in Fig. 5.6(b)) shows an average pile-up height of  $\sim$  60 nm and further confirms the machining depth of  $\sim$  5 nm. The SEM images in Fig. 5.6(e) and (f) show how the majority of the PtSe<sub>2</sub> channel remained intact post-machining and appears smoother, in agreement with what was measured in AFM. However, upon closer examination of Fig. 5.6(f), it appears that some grains were removed completely from film, causing discontinuities. In addition, initial roughness of TAC surfaces led to

difficulties in reproducible machining, even though machining appeared to reduce roughness. Attempts were made to perform I-V measurements on the machined channel devices but it was found that no current was transmitted. This was mostly likely due to discontinuity in TAC films in general but also exacerbated post-machining due to surface roughness caused by the TAC process (see Fig. 5.6(f)).

### 5.3.2 NANOMACHINING Pt PRE-SELENISATION

An alternative method trialled was to nanomachine pristine Pt before selenisation to achieve desired thickness as TAC significantly increases roughness, particularly with thicker Pt films. Using UV lithography (Section 3.3), 30 nm of Pt was sputtered onto SiO<sub>2</sub>/Si substrate (Fig. 5.7(a)). 30 nm was chosen as this is the general thickness for metal contacts. The quality and control over the machining was significantly improved due to the relatively smooth Pt surface (RMS roughness  $\sim$  1.3 nm). Subsequently, for a 5  $\mu$ N load and 20  $\mu$ m/s tip velocity, it was possible to control the machining depth for each pass within a nanometer (Fig. 5.7(b) and (c)). In addition, a Pt channel was nanomachined repeatedly with the same parameters (5  $\mu$ N, 20  $\mu$ m/s), allowing for iterative thinning for multiple passes, as can be observed in Fig. 5.7(a),(d)-(f).

By the third pass (Fig. 5.7(f)), bulk Pt appears to have been removed from the edges of the channel, i.e. channel width has significantly decreased. Averaged topographical profiles were extracted from each of the images (a),(d)-(f) for comparison. Fig. 5.8(a) and (b) shows the average Pt channel heights and widths respectively before and after each machining pass. The decrease in the Pt channel width further confirms the delamination of Pt during the nanomachining process. This is most likely due to Pt's poor adhesion to SiO<sub>2</sub>,<sup>264,265</sup> rather than the nanomachining alone. Therefore, 30 nm Pt on SiO<sub>2</sub> is too thick a starting point for nanomachining. In Fig. 5.8(c), the step heights (from the pristine to machined Pt in Fig. 5.8(a)) are used to determine the recess height and the amount of material removed per pass relative to the order of machining passes. The mean amount of Pt removed with each pass at

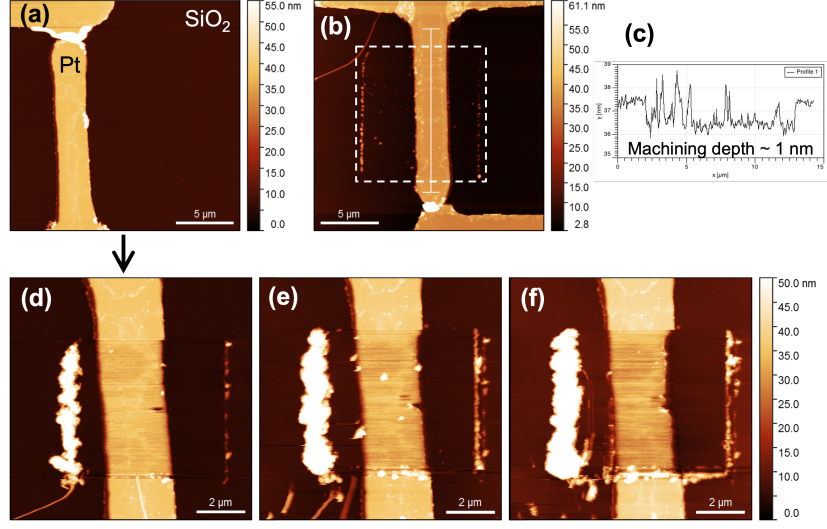


**Figure 5.7:** (a) Topographical image of 30 nm thick Pt channel (width 3 μm) between Pt (also 30 nm) contacts. (b) Pt channel post-nanomachining. Dotted line indicates machined region. (c) Line height profile showing ~ 1 nm machining depth. (d) Pt channel (a) after first pass, (e) second pass, and (f) third pass, each at 5 μN load, 20 μm/s tip velocity.

a constant load of 5 μN is ~ 3.83 nm.

It has been found that converting more than a few nm of Pt leads to disruption of the films, negating the pre-selenisation machining. This is as a result of the change in preferred orientation of PtSe<sub>2</sub> films forming during selenisation. Lin *et al.* reported an exponential increase in edge-rich (i.e. vertically aligned) PtSe<sub>2</sub> as a function of increasing thickness, from ~ 20 nm upwards<sup>266</sup> (~ 5 nm for starting Pt thickness). Similar morphologies of layers perpendicularly aligned to the growth substrate have been seen in MoS<sub>2</sub> and MoSe<sub>2</sub>.<sup>95</sup> Upon selenisation of > 5 nm of Pt, Lin *et al.* suggest chemical conversion occurs much faster than diffusion of Se gas through the film, i.e. diffusion along the layers through the vdW gaps would be significantly faster than through the layers, resulting in the layers naturally orientating perpendicular to the film. Therefore the in-plane electronic transport would be significantly decreased in PtSe<sub>2</sub> films thicker than 20 nm due to an increased contribution from out-of-plane pathways, such as vertically aligned grains.



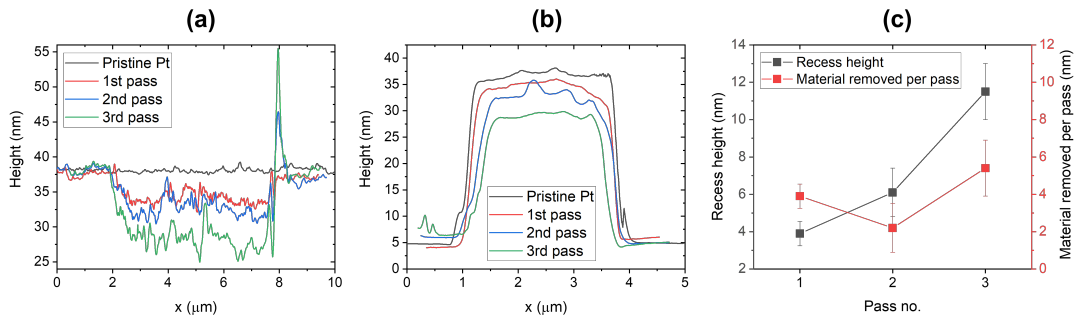


**Figure 5.8:** Topographical profiles of Pt channel (width  $\sim 3 \mu\text{m}$ ) before and after multiple nanomachining passes (each at  $5 \mu\text{N}$  load,  $20 \mu\text{m/s}$  tip velocity) (a) parallel and (b) perpendicular to the Pt channel. (c) Plot showing pass number vs. recess height (i.e. pristine Pt to machined step height) and amount of material removed per pass.

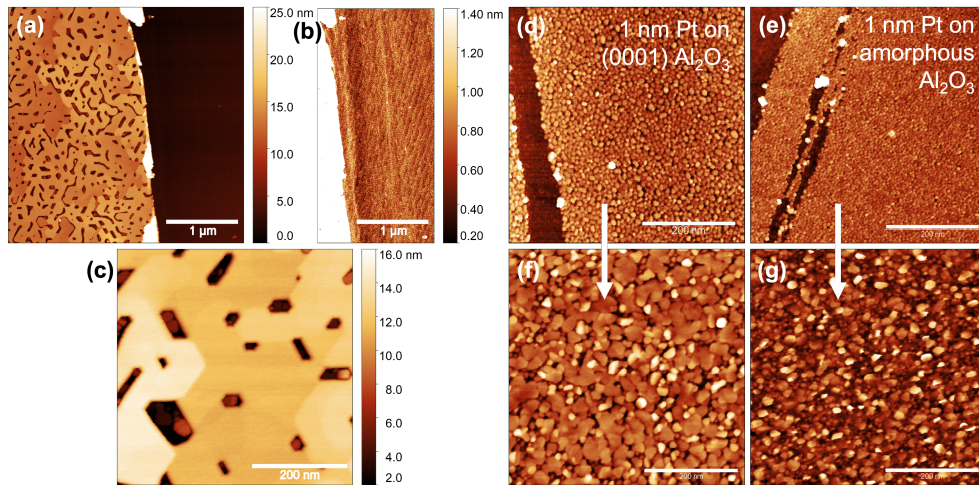


**Figure 5.9:** Topographical AFM images of Pt films deposited *via* molecular beam epitaxy (MBE). (a) 15 nm Pt deposited on c-plane sapphire ( $0001 \text{Al}_2\text{O}_3$ ). (b) Scale-adjusted in (a) to show terraces of growth substrate. (c) Magnified image of 15 nm Pt MBE growth. (d) 1 nm Pt on C-plane sapphire pre-selenisation. (e) 1 nm Pt on amorphous alumina ( $\text{Al}_2\text{O}_3$ ) pre-selenisation. (f) and (g) are (d) and (e) after conversion to  $\text{PtSe}_2$  *via* the TAC method. Scale bar for (d) - (g) is 200 nm.

As previously noted, since Pt adheres poorly to SiO<sub>2</sub>, it is worth examining other substrates in addition to higher crystallinity in the starting Pt film. An investigation into the substrate-dependent deposition of Pt and subsequent selenisation was also carried out. To provide better control, molecular beam epitaxy (MBE) was employed for growth of the Pt film, with the target substrate heated at an elevated temperature to 600 °C during deposition. While the epitaxial quality improves at higher substrate temperatures (> 600 °C), above a critical temperature Volmer-Weber growth mode starts and causes a rough film morphology.<sup>267</sup> In addition, a comparison between growth substrates was carried out, namely amorphous alumina (Al<sub>2</sub>O<sub>3</sub>) and c-plane (0001) sapphire (monocrystalline Al<sub>2</sub>O<sub>3</sub>). Fig. 5.9(a) shows the epitaxial growth of Pt (111) on (0001) Al<sub>2</sub>O<sub>3</sub>. The height scale in (a) is adjusted in Fig. 5.9(b) to show the (0001) Al<sub>2</sub>O<sub>3</sub> atomic steps. Fig. 5.9(c) shows a close-up of the the continuous oriented film indicating crystalline growth with preferred epitaxial relationship and smooth surfaces, including step heights in agreement with literature values for atomic steps of Pt (111).<sup>268</sup> In Fig. 5.9(d) and (e), we can see that the MBE deposition of Pt on the monocrystalline substrate forms larger grains than on the amorphous growth substrate. For thinner films, there is island growth (Volmer-Weber) rather than the ideal Frank-van der Merwe (layer-by-layer) or even Stranski-Krastanov (layer-plus-islands) growth. From Fig. 5.9(f) and (g), we can see that the deposited Pt grain sizes in (d) and (e) increase further upon selenisation for all substrates. For c-plane sapphire (0001 Al<sub>2</sub>O<sub>3</sub>), the mean grain diameter increases from 11 nm pre-selenisation to 40 nm upon conversion to the TMD. The same can be said for amorphous alumina, however albeit slightly less, from 7 to 20 nm.

### 5.3.3 NANOMACHINING MECHANICALLY EXFOLIATED PtSe<sub>2</sub> FLAKE DEVICES

For comparison with the roughness of the TAC films, pristine mechanically-exfoliated PtSe<sub>2</sub> flakes were nanomachined as a parallel approach. Bulk PtSe<sub>2</sub> crystals were obtained from HQ Graphene. Using the method mentioned in Section 3.2.5, pristine flakes were exfoliated using Scotch tape and

later transferred to SiO<sub>2</sub>/Si substrates. Due to the unusually strong interlayer interaction between PtSe<sub>2</sub> layers, problems arose while trying to isolate thin flakes that were large in lateral area (> a few μm). Since the initial yield of thin flakes was very low, some preliminary machining experiments to calibrate the nanomachining rate were carried out on thicker flakes.

The nanomachined ME flakes indicate that, if the roughness of TAC films is decreased, the quality and control of the nanomachining process is greatly improved. On ME flakes, the shallowest machining depth was ~ 0.8 nm, approximately the thickness of one ML, showing the capability of nanomachining to achieve layer-by-layer removal.

After refinements in the ME technique, the yield of larger, thinner flakes improved. AFM images of such flakes can be seen in Fig. 5.10(a), (c) and (d). From line profiles of Fig. 5.10(a), a ML thickness of ~ 0.6 nm was determined (Fig. 5.10(b)). This was again confirmed by a comparison of topographical AFM and Raman spectra of the corresponding low-frequency layer-dependent peaks of the same area in Fig. 5.10(d) and the spectra are in good agreement with reported values.<sup>79</sup>

Characteristic PtSe<sub>2</sub> peaks can be seen in the Raman spectra shown in Fig. 5.10(e) and (f). In (f) there are the two prominent vibrational modes visible. When excited at 532 nm, the ~ 180 cm<sup>-1</sup> peak corresponds to the in-plane E<sub>g</sub> mode, while the ~ 205 cm<sup>-1</sup> peak is the out-of-plane A<sub>1g</sub> mode. In addition, thickness-dependent shifts of the E<sub>g</sub> mode and changes in the E<sub>g</sub>/A<sub>1g</sub> intensity ratio are observed. Both the E<sub>g</sub> mode redshifts and the A<sub>1g</sub> mode increases in relative intensity to the E<sub>g</sub> with increasing thickness.<sup>235</sup> The less intense feature at ~ 230 cm<sup>-1</sup> is assigned to an overlap between the A<sub>2u</sub> and E<sub>u</sub> modes, which are longitudinal optical modes involving the out-of-plane and in-plane motions of Pt and Se atoms respectively.<sup>76</sup> This contribution is most evident with close-to-ML thickness and decreases in relative intensity with increasing flake thickness.

For 2D layered materials, lattice vibrations contain high-frequency intralayer vibrations (e.g. E<sub>g</sub>, A<sub>1g</sub>) and low-frequency interlayer vibrations.<sup>146</sup> The interlayer vibrations are located at low-frequencies that cannot be resolved by standard equipment. These can be divided into the out-of-plane

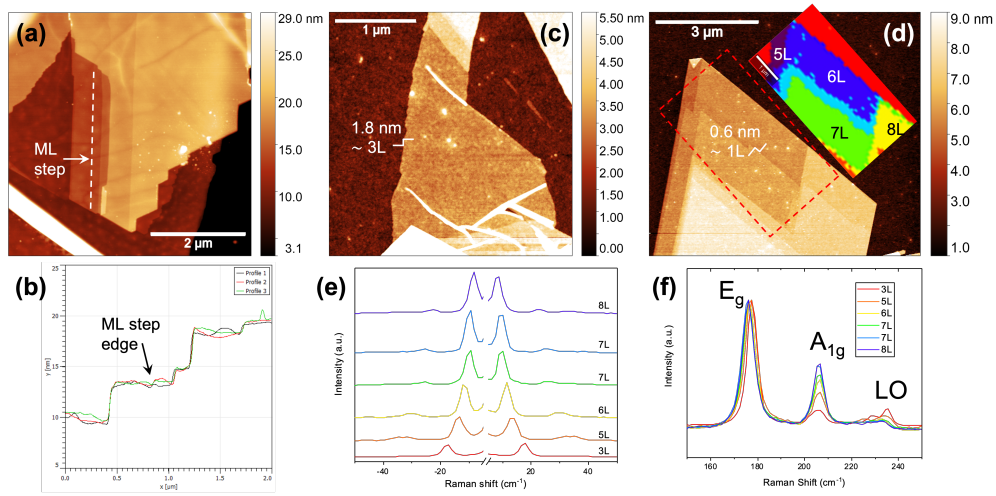


**Figure 5.10:** Topographical AFM images of ME PtSe<sub>2</sub> flakes. (a) Bulk region of ME PtSe<sub>2</sub> flakes showing multiple step edges. White dashed line indicates ML step edge. (b) Topographical line profiles of (a) indicating ML step edge and thickness. (c) ME flake with 3L region. White lines indicate height profiles. (d) AFM image of ME flake with corresponding low-frequency Raman peak intensity map overlay indicating layer number. (e) Low-frequency Raman spectra from different regions in (c) and (d) from  $-50$  to  $+50$   $\text{cm}^{-1}$ . (f) Raman spectra from  $150 - 250$   $\text{cm}^{-1}$  showing characteristic PtSe<sub>2</sub> modes. These spectra have been normalised to the  $E_g$  mode at  $\sim 180$   $\text{cm}^{-1}$  for clarity.

layer-breathing mode (LBM), in-plane shear mode and standing wave mode. Fig. 5.10(e) shows low-frequency Stokes and anti-Stokes Raman spectra of the PtSe<sub>2</sub> flakes. This characteristic peak corresponds to LBM interlayer vibration in PtSe<sub>2</sub>, which describes the motion of the top half and bottom half of the layers vibrating collectively but in opposite phase.<sup>144,146</sup> The Stokes peaks are redshifted at  $\sim 22$   $\text{cm}^{-1}$  from few-layer to thicker layers as the peaks approach 0 Raman shift, showing a clear trend in LBM peak position with increasing layer number.

To aid alignment for device fabrication, the flakes were exfoliated onto pre-patterned SiO<sub>2</sub>/Si substrates with coordinates, allowing for ease of contacting *via* maskless UV photolithography (see Fig. 5.11(a) and (b)). Fig. 5.11(c) and (d) show the corresponding topography of typical flakes after contacting with Ti/Au. AFM determined the thickness of flake (c) to be 16 nm and (d) to be 13 nm which corresponds to  $\sim 27$  and  $\sim 22$  layers respectively.

Nanomachining was carried out on the contacted flake in Fig. 5.12(a), which consisted of  $\sim 15$  layers

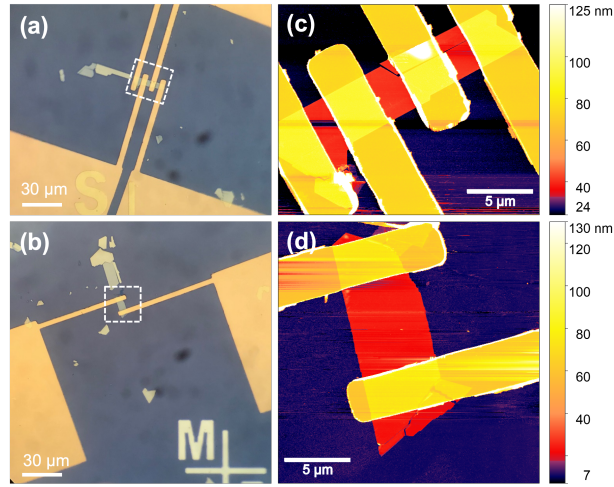


**Figure 5.11:** (a) and (b) are optical images of ME PtSe<sub>2</sub> flakes contacted via maskless UV photolithography. Contact pads are 100 μm<sup>2</sup>. (c) and (d) are corresponding topographical AFM images of flake devices, respectively (pre-machining).

(9 nm in thickness). Five machining passes with the same load of 2 μN (250 mV) and tip velocity of 5 μm/s were performed and the flake was imaged in between each pass. Fig. 5.12(b) shows the flake after the first nanomachining pass. The flake appears significantly cleaned of surface adsorbates, which are most likely from the ME process, rather than machining. The reduction in flake height was ~ 1.8 nm. Fig. 5.12(c) shows the device after the fifth machining pass. It is evident that significant destruction has occurred in the machined area with undesirable material removal particularly along the flake edges and grain boundaries. Fig. 5.12(d) shows a Raman map of the variation in position of the in-plane E<sub>g</sub> (~ 173 cm<sup>-1</sup>) mode of (c), as this can be influenced by layer thickness. From this, we can see the peak is at slightly greater wavenumbers in the nanomachined region, indicating thinning from nanomachining. Fig. 5.12(e) shows an intensity ratio map of the out-of-plane A<sub>1g</sub> to the in-plane E<sub>g</sub> mode. O'Brien *et al.* previously determined the thickness dependency of the PtSe<sub>2</sub> A<sub>1g</sub> mode intensity (with respect to the intensity of the E<sub>g</sub> mode),<sup>76</sup> similar to observations in other TMDs, such as MoS<sub>2</sub> and WS<sub>2</sub>.<sup>151,269</sup> We can see in Fig. 5.12(e) that the machined area, due to the lower ratio value, is indeed thinner than the pristine region, in agreement with (d). However, if we

examine the variation in width of the  $E_g$  peak in a map (Fig. 5.12(f)), the  $E_g$  peak signal is at its broadest in the nanomachined area with a FWHM of  $\sim 8 - 11 \text{ cm}^{-1}$  compared to  $\sim 6 \text{ cm}^{-1}$  in the pristine area. Szydłowska *et al.* deemed  $E_g$  FWHM  $> 7 \text{ cm}^{-1}$  to be of lesser quality, indicating though thinner, the  $\text{PtSe}_2$  layers are more disordered/less crystalline from the machining process.<sup>235</sup> This would also suggest that successive passes of nanomachining on an area results in more defective/damaged material that is easier to nanomachine, leading to more material removed in those areas.

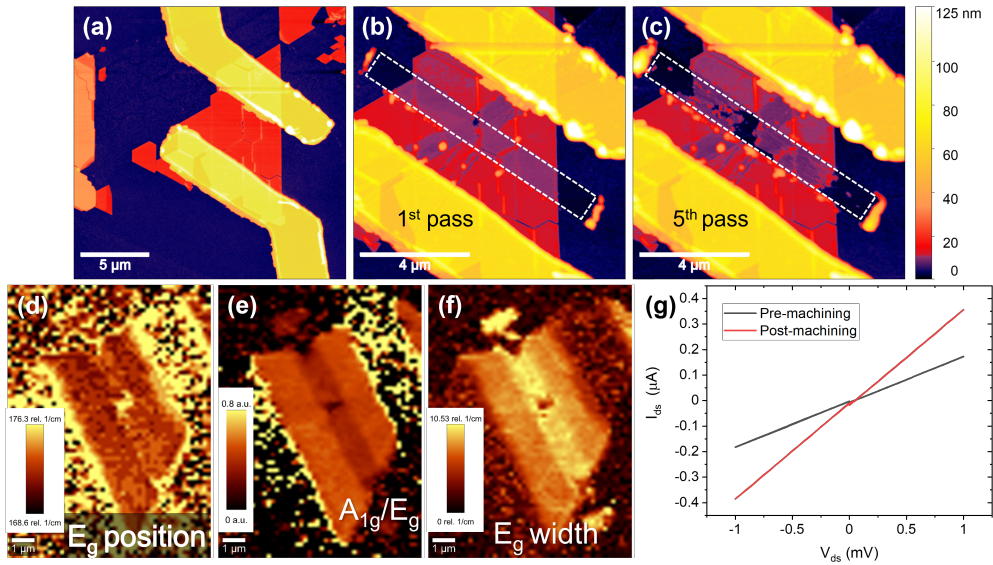


**Figure 5.12:** Topographical AFM images of ME  $\text{PtSe}_2$  flakes (a) before nanomachining, (b) after first nanomachining pass and (c) fifth pass (white dashed line indicates machined area). Each pass had  $2 \mu\text{N}$  load and  $20 \mu\text{m/s}$  tip velocity. (d) Raman peak position map of (c) showing variation in  $\text{PtSe}_2 E_g$  position ( $173 \text{ cm}^{-1}$ ) after nanomachining. (e) Map of Raman mode intensity ratio  $A_{1g}/E_g$ . (f) Map of Raman  $E_g$  mode width. (g) Graph showing IV curve of the 2-probe measurement performed on  $\text{PtSe}_2$  before and after nanomachining.

A two-probe method was used to electrically characterise the device in ambient conditions. A voltage sweep between  $-1$  to  $1 \text{ V}$  was performed before and after nanomachining. The resulting I-V curve in Fig. 5.12(e) reveals an increase in conductivity post-nanomachining. This is in contrast to a potentially expected decrease in current indicating semiconductor behaviour ( $if < 3L$ ) or destruction of the device due to nanomachining. This discrepancy in conductivity can be most likely attributed

to varied conditions between measurements, such as changes in contact resistance due to the removal of adsorbates/contaminants.

Topographical information was extracted to gain a better understanding of the nanomachining process on PtSe<sub>2</sub> when performing the five passes in Fig. 5.12. Fig. 5.13(a) shows where on the AFM height retrace images the line profiles were extracted from. Fig. 5.13(b) are the topographical profiles parallel (left plot) and normal (right plot) to the machining direction. It is evident more material is removed incrementally with the increasing number of machining passes. However, the machining at constant load (2  $\mu\text{N}$ ) appeared to reach a threshold at approx. the 8 nm mark ( $\sim 6$  nm in channel height relative to the SiO<sub>2</sub>), whereby it cannot remove further material incrementally but rather tears/strips away layers in bulk. This led to complete removal of PtSe<sub>2</sub> in some areas during the 5th pass, which can be seen in Fig. 5.13(b). This is most likely due to PtSe<sub>2</sub>'s strong interlayer interaction being greater than its adherence to SiO<sub>2</sub>.

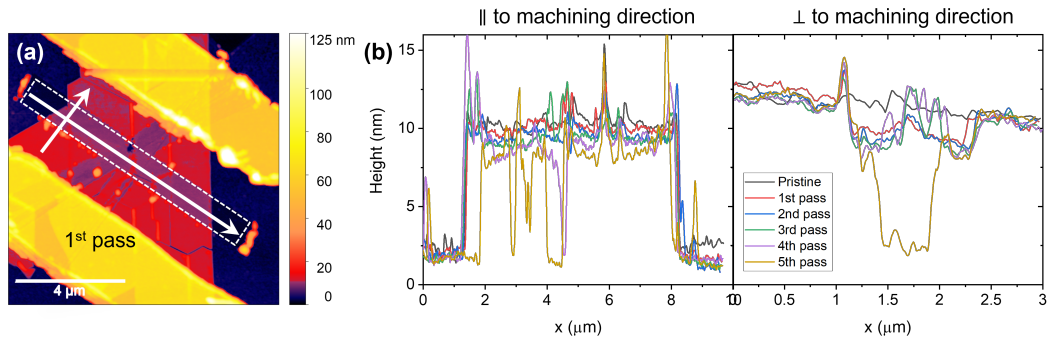


**Figure 5.13:** (a) Topographical AFM image of ME PtSe<sub>2</sub> flake after first nanomachining pass (2  $\mu\text{N}$  load, 20  $\mu\text{m/s}$  tip velocity). White dashed line indicates machined area with white arrows showing topographical line profiles and directions. (b) Topographical line profiles parallel and perpendicular to the machining direction.

The flake in Fig. 5.11(b)/(d) was subsequently contacted to the AFM puck to ensure a good conduction path (Fig. 5.14(a)) for conductive scanning probe measurements, i.e. KPFM and PF-TUNA. This was achieved by contacting one of the TiAu contact pads to the puck using Ag paint and an Ag wire (Fig. 5.14(b)). The flake was then nanomachined with a load of 0.36  $\mu\text{N}$ .

However, this load was too small and appeared to only partially clean the flake surface of adsorbates/contaminants from the ME process (Fig. 5.14(c)). Fig. 5.14(d) is the corresponding KPFM image of the local surface potential/contact potential difference (CPD). It shows an increase in surface potential of  $100 \pm 60$  mV in the machined area relative to the pristine PtSe<sub>2</sub> ( $+0.1$  eV in  $\phi_{\text{PtSe}_2}$ ). This increase can be attributed to the removal of adsorbates which tend to lower the work function of the material surface.<sup>202</sup> PF-TUNA was performed on the same area at a sample bias of 1 V. Fig. 5.14(e) shows the topography, while (f) and (g) show the tunneling and peak currents respectively (see Chapter 2 Section 2.1.6 for breakdown of measured currents). We can see the ‘cleaned’ area appears significantly more conductive than the rest of the flake. However, again this is likely due to removal of adsorbates rather than improved conductivity from nanomachining as greater contrast is observed when the layer beneath can be seen rather than the defective remaining layers.

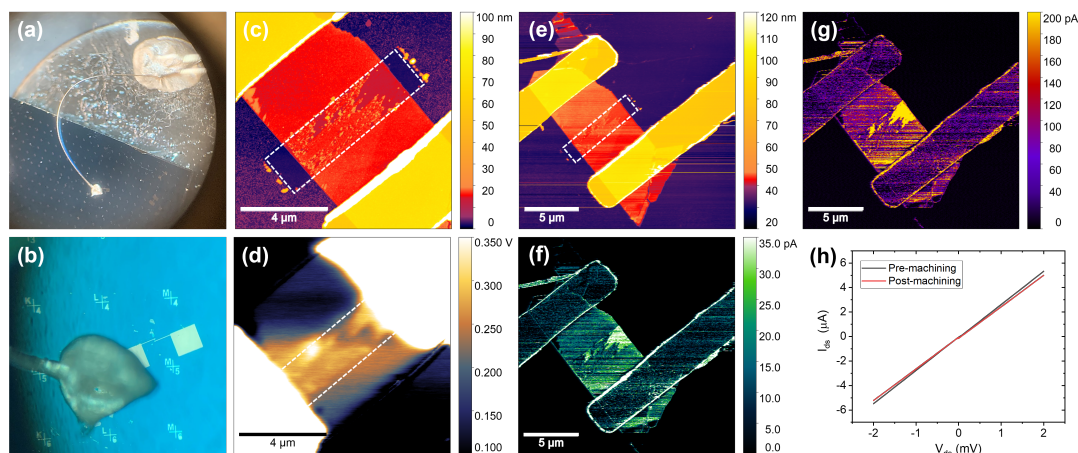


**Figure 5.14:** (a) Optical image of macro Ag wire contact on PtSe<sub>2</sub> flake device. (b) Zoom of macro contact. (c) Topography and (d) corresponding contact potential difference (CPD) of contacted flake (a) post-machining (1st pass,  $0.36 \mu\text{N}$  load,  $20 \mu\text{m/s}$  tip velocity). White dashed line indicates nanomachining area. (e) Topography, (f) tunneling current and (g) peak current maps of (a). (h) Graph showing IV curve of the 2-probe PtSe<sub>2</sub> before and after nanomachining.

Similar to the previous flake, a two-probe method was used to electrically characterise the device in ambient conditions. A voltage sweep between  $-2$  to  $2$  V was performed before and after



nanomachining. The resulting I-V curve in Fig. 5.14(h) reveals a slight decrease in conductivity post-nanomachining but ultimately no significant change is evident as the flake is still exhibiting semi-metallic behaviour. However, in comparison to the previous PtSe<sub>2</sub> device (Fig. 5.12), the conductivity is much greater overall, probably due to Fig. 5.14 being an intact crystal, rather than segmented, which would decrease the conductivity. Again, these discrepancies in conductivity can also be attributed to varied conditions between measurements and devices, e.g. changes in contact resistance.

The flake was nanomachined further to remove layers. Multiple passes were repeatedly performed with increasing loads from 0.8  $\mu\text{N}$  (100 mV deflection setpoint) incrementally to 2.7  $\mu\text{N}$  (350 mV). In Fig. 5.15(a), we can see that the increased load of 0.8  $\mu\text{N}$  from the initial pass of 0.36  $\mu\text{N}$  allows for consistent cleaning of the flake surface and removal of adsorbates, resulting in a 2 nm reduction in the flake height. From the cleaned step height in Fig. 5.15(a), the flake is determined to be  $\sim 10.8$  nm thick, corresponding to  $\sim 18$  layers (L). Fig. 5.15(b) shows the same area after nanomachining with a 1.6  $\mu\text{N}$  load (200 mV deflection setpoint).

An average of the recessed height compared to the original flake height shows a reduction of  $\sim 5$  nm in flake thickness. The recess average step height on SiO<sub>2</sub> is  $\sim 6.6$  nm ( $\sim 11$  L), at thickness at which the material should be semimetallic. Six more machining passes (nine in total) were performed with increasing setpoints; 200 mV ( $\times 3$ ), 250 mV, 300 mV and 350 mV, which corresponded to 1.6, 1.95, 2.3 and 2.7  $\mu\text{N}$ , respectively, the last of which resulted in destruction of the device (Fig. 5.15(c) and (d)). Raman maps depicting the variation in FWHM of the in-plane E<sub>g</sub> mode (177 cm<sup>-1</sup>, Fig. 5.15(f)) and the ratio of the out-of-plane mode A<sub>1g</sub> mode intensity (207 cm<sup>-1</sup>) to the E<sub>g</sub> intensity (Fig. 5.15(g)) of the PtSe<sub>2</sub> show the machined and destroyed regions, as well as the pile-up at the sides. The lack of signal in the destroyed region indicates that there is essentially no longer PtSe<sub>2</sub> present as it was ripped away during nanomachining. In addition, the FWHM broadening of the machined region would indicate some disordering of the PtSe<sub>2</sub> is occurring during nanomachining. However, the FWHM

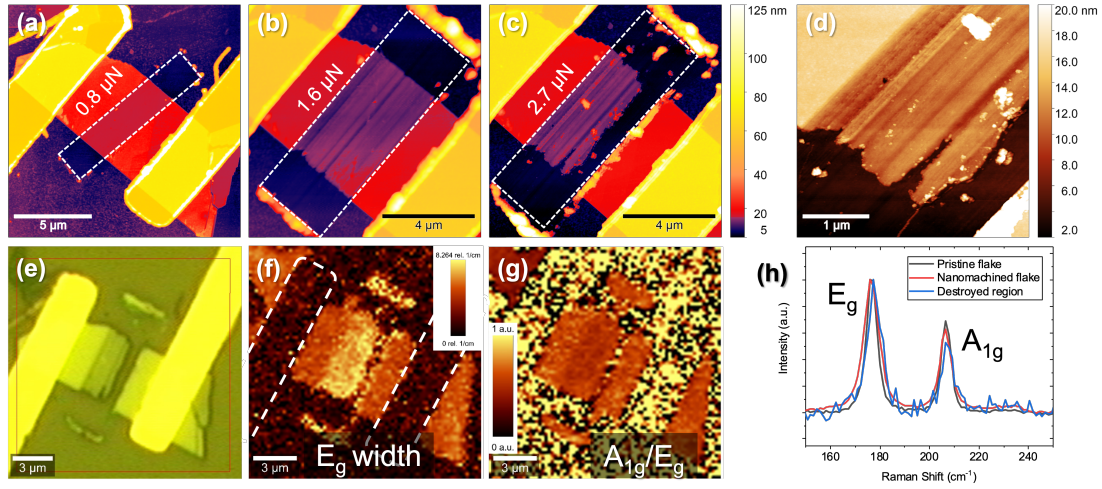


**Figure 5.15:** Topographical AFM images of ME PtSe<sub>2</sub> flake (a) after 0.8 μN load, (b) after 1.6 μN load and (c) after 2.7 μN load (tip velocity constant for each pass at 20 μm/s). (d) Close-up of machined region in (c). (e) Optical image of (c). Red box indicates Raman scan area. (f) Raman peak FWHM map of (c) showing the variation in width of in-plane E<sub>g</sub> mode (177 cm<sup>-1</sup>). (g) Raman map of (c) showing the ratio of out-of-plane A<sub>1g</sub> mode intensity (207 cm<sup>-1</sup>) to E<sub>g</sub> mode intensity (177 cm<sup>-1</sup>). Dashed lines in (f) outline the Au contacts. (h) Raman spectra comparing E<sub>g</sub> and A<sub>1g</sub> modes. These spectra have been normalised to the E<sub>g</sub> mode at ~177 cm<sup>-1</sup> for clarity.

remains  $< 8.5 \text{ cm}^{-1}$ , indicating less destruction of the PtSe<sub>2</sub> than in the previous case. In the ratio map (Fig. 5.15(g)), we can see the machined area to be of lower ratio of A<sub>1g</sub> to E<sub>g</sub>, indicating thinning of the PtSe<sub>2</sub>. Fig. 5.15(h)) shows a comparison of the characteristic Raman spectra of the pristine, nanomachined and destroyed regions of the flake. The slight decrease in the relative height of the A<sub>1g</sub> mode to the E<sub>g</sub> mode between the pristine and machined areas show that the region was marginally thinned. Like the previous device, nanomachining appeared to cause some damage to the PtSe<sub>2</sub> layers during thinning but less damage appeared to occur at repeated loads of  $< 2 \text{ μN}$ .

Again, topographical information was extracted to gain a better understanding of the nanomachining process on PtSe<sub>2</sub> while performing the nine passes in Fig. 5.15. Fig. 5.16(a) shows the loads used in each nanomachining operation (tip velocity remained constant at 20 μm/s). Fig. 5.16(b) is a comparison of topographical profiles of the PtSe<sub>2</sub> device surface after most iterations of nanomachining. Pass 6 (P6) to pass 9 (P9) were performed consecutively, without periodic

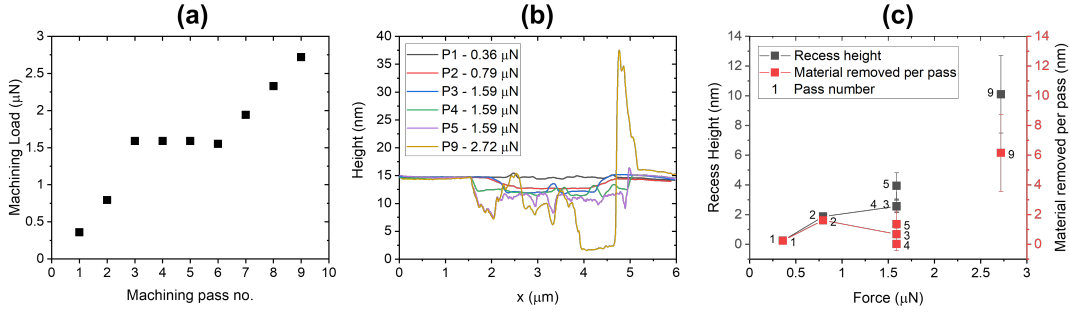


**Figure 5.16:** (a) Graph of machining loading forces vs. corresponding order of passes (tip velocity constant at  $20 \mu\text{m/s}$ ). (b) Topographical line profiles perpendicular to machining direction. (c) Plot of loading forces vs. resulting recess heights and material removed per pass.

imaging. Using the line profiles in (b), the average recess step height and subsequently the average amount of material removed with each pass were extracted and plotted in Fig. 5.16(c). There is a general upward trend of increasing passes and load results in more material being removed. Between loads of  $0.8 - 1.6 \mu\text{N}$  ( $100 - 200 \text{ mV}$  deflection setpoint), an average of  $1 \text{ nm}$  of  $\text{PtSe}_2$  is removed with each pass, which is equivalent to  $\sim 1.5 \text{ L}$ . For the last pass at  $2.7 \mu\text{N}$  (P<sub>9</sub>), we see that the most material is removed (average  $\sim 6 \text{ nm}$ ), however inconsistencies in the layer removal become evident, with some areas further recessed than others, indicating cutting and stripping of the  $\text{PtSe}_2$  layers.

#### 5.4 CONCLUSION

A novel technique for exploring and manipulating TMD layers has been developed *via* nanomachining using AFM. This technique was used to reduce layer thickness of  $\text{PtSe}_2$  TAC films and ME flakes. The machining is required to isolate the thinnest section from the bulk in the hopes of contacting it to observe mobilities, amongst other properties. AFM and SEM results revealed the nanomachining of TAC films to be quite difficult due to the roughness of the films post-selenisation, but can be used to produce thinner, smoother films overall. Machining of pristine

Pt channels allowed more control over the quantity of nanomachining, and also quality. However, selenisation of more than 5 nm Pt results in disruption of the films due to exponential increase in edge-rich PtSe<sub>2</sub>, thus significantly decreasing electronic transport in plane and reducing the reliability of fabrication for potential devices. For comparison with TAC films, pristine ME PtSe<sub>2</sub> flakes were nanomachined with a stepped depth accuracy of  $\sim 0.8$  nm, approximately the thickness of one ML, showing the capability of layer-by-layer removal via this technique. Further in-depth characterisation was conducted on flakes of varying thicknesses using AFM and low-frequency Raman spectroscopy. Using maskless UV lithography, two terminal devices were created from ME flakes. The devices were subsequently nanomachined and the results examined. Initially, it appeared that nanomachining cleaned the flake surface of adsorbates and contaminants, most likely from the mechanical exfoliation and ambient conditions. The cleaning occurred at nanomachining forces  $< 1.5 \mu\text{N}$ . With forces  $> 1.5 \mu\text{N}$ , the flakes were marginally thinned but the layers tended to adhere together rather than separate incrementally. This is most likely due to the extraordinarily strong interlayer coupling in PtSe<sub>2</sub>. In addition, nanomachining at forces  $> 2.3 \mu\text{N}$  resulted in complete material removal from the substrate, due to the weak coupling between the ME PtSe<sub>2</sub> and SiO<sub>2</sub>, particularly in comparison with the PtSe<sub>2</sub> interlayer interaction. Despite this, there is scope for nanomachining as a thinning method for devising a ‘self-contacting’ PtSe<sub>2</sub> FET, should a more appropriate substrate be selected, such as Au, where the 2D crystal/Au binding is invariably stronger the corresponding interlayer bonding.<sup>252</sup> However, an Au substrate would present challenges for device measurement. In addition, there is potential to apply these techniques to other TMD systems like PtS<sub>2</sub>, which has very similar properties to PtSe<sub>2</sub>, such as crystal structure, interlayer interactions and electronic structure.<sup>78,81,234,270</sup>

*Science makes people reach selflessly for truth and objectivity; it teaches people to accept reality, with wonder and admiration, not to mention the deep awe and joy that the natural order of things brings to the true scientist.*

Lise Meitner, physicist

# 6

## Conclusions & Future Work

For over 400 years, the optical microscope has reigned supreme in the field of microscopy. Nevertheless other types of microscopy techniques based on electrons and atomic forces have come to the fore in the last century. In particular, SPM has revolutionised nanotechnology and allowed the study and manipulation of materials on the nanoscale, making it ideal for the study of solid-state physics and semiconductor technologies. As the research field of 2D materials continues to expand exponentially, particularly with applications in future nanoelectronics, making the case for the need

of an SPM-based toolbox, such as AFM, whose capability as both a microscopic technique and nano-manipulator for these materials has never been more relevant.

In this thesis, various tools and techniques for characterising and manipulating several TMD materials and heterostructures have been examined and developed. Particular focus was given to AFM and KPFM of VPD-grown and ME TMDs and AFM-based mechanical lithography of these materials, namely nanoshaving and nanomachining.

In Chapter 4, the non-covalent functionalisation of monolayer TMDs, MoS<sub>2</sub> and WS<sub>2</sub>, on Si/SiO<sub>2</sub> with organic SAMs of PDI was explored. These organic-inorganic heterostructures were manipulated using the approach of nanoshaving and the reversibility of such functionalisation was demonstrated using the complementary non-destructive techniques of KPFM and Raman spectroscopy. Nanoshaving pristine monolayer TMD flakes had negligible effect on the topography but KPFM showed contrast in CPD between the shaved and non-shaved areas, most likely due to clearing of surface contaminants. It was shown that PDI selectively forms SAMs on TMD surfaces rather than Si/SiO<sub>2</sub>. A grating pattern with feature sizes < 250 nm was successfully shaved into the PDI/MoS<sub>2</sub> heterostructure, demonstrating the high-resolution capabilities of nanoshaving as a lithographic technique. These results indicate that nanoshaving is a viable lithography technique that introduces minimal contaminants, i.e. no resist necessary and without collateral damage to the SAM. Nanoshaving could be suitable for the fabrication of other ordered optical/photonic structures, e.g. by rotating the sample 90°, a shaving pass of the same spacing parameters would produce a dot array. In addition, non-covalent co-functionalisation of MoS<sub>2</sub> was demonstrated using PTCDA SAMs on previously nanoshaved areas, allowing more complex patterns/arrangements to be produced.

Chapter 5 reported a technique for exploring and manipulating TMD layers *via* nanomachining using AFM. This technique was used to reduce layer thickness of TAC-grown PtSe<sub>2</sub> films and ME flakes. AFM and SEM results revealed the nanomachining of TAC-grown films to be quite difficult

due to the roughness of the films post-selenisation when compared to exfoliated materials. Nevertheless nanomachining TAC films resulted in thinner, smoother films overall. Machining of pristine Pt channels allowed more control over the quantity of nanomachining, and also quality. For comparison with TAC-grown films, pristine ME PtSe<sub>2</sub> flakes were nanomachined with further in-depth characterisation conducted on flakes of varying thickness using AFM and low-frequency Raman spectroscopy. Using maskless UV lithography, two terminal devices were created from ME flakes which were subsequently nanomachined. Nanomachining at forces  $>3 \mu\text{N}$  resulted in complete material removal from the substrate due to the weak coupling between the ME PtSe<sub>2</sub> and SiO<sub>2</sub>, particularly in comparison with the PtSe<sub>2</sub> interlayer interaction. For weaker forces, it was also found that successive passes of nanomachining on an area resulted in more defective/damaged material that was easier to nanomachine, leading to more material removed in those areas.

Despite this, there is scope for nanomachining as a thinning method for devising a ‘self-contacting’ PtSe<sub>2</sub> FET, should a more appropriate substrate be selected, such as Au, where the 2D crystal/Au binding is invariably stronger than the corresponding interlayer bonding.<sup>252</sup> However, an Au substrate would present challenges for device measurement. In addition, there is potential to apply these techniques to other TMD systems like PtS<sub>2</sub>, which has very similar properties to PtSe<sub>2</sub>, such as crystal structure, interlayer interactions and electronic structure.<sup>78,81,234,270</sup> This suggests a path for continuous monitoring of device performance with each layer removal down to the monolayer, starting with metallic multi-layers and thinning down to a semiconducting monolayer. This would enable the design of ‘self-contacted’ devices based on TMDs through the creation of a semiconducting channel *via* nanomachining with high mobility, low contact resistance and low power.

For nanoshaving non-covalently functionalised SAMs on TMDs, there is scope for exploring many possibly combinations of SAMs or other adhesive molecules or even other TMDs as heterostructures. Within this, there is opportunity to delve into the fabrication and measurement of

p-n junctions, particularly using KPFM as a technique.<sup>271,272</sup> Additionally, to better observe the PL components, further measurements should be carried out on the heterostructures at lower temperatures (e.g. 77 K) to reduce non-radiative recombination effects on the spectrum. With regards nanoshaving's capability of nanolithography, the deposition of materials on the nanoshaved patterns should be examined as well as more advanced structures such as dot arrays. These nanoscale dot arrays could provide an excellent platform towards quantum information processing.<sup>273</sup>

To conclude, the techniques of AFM-based mechanical manipulation, namely nanoshaving and nanomachining, of TMDs and TMD-based heterostructures have been explored and examined and remarkable control over material removal and patterning at the nanoscale has been shown. The properties of both pristine and manipulated TMDs and TMD heterostructures have been thoroughly studied by surface microscopy and spectroscopic techniques, demonstrating the capability of an AFM-based toolbox for examining 2D materials. Nevertheless, there is further scope for more in-depth study and characterisation of the materials as well as opportunities to further improve manipulation parameters.





# Nanoshaving Raman Spectra

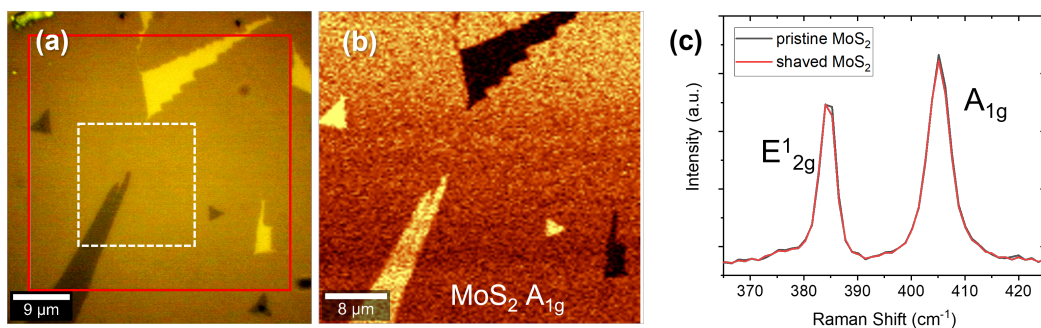


**Figure A.1:** Nanoshaved pristine MoS<sub>2</sub> Raman — (a) Optical image of the MoS<sub>2</sub> area scanned using Raman spectroscopy (red box) with shaved area indicated by white dashed box. (b) Raman peak intensity map of MoS<sub>2</sub> out-of-plane A<sub>1g</sub> (406 cm<sup>-1</sup>) mode. (c) average Raman spectra comparison of shaved and non-shaved pristine MoS<sub>2</sub> showing both E<sub>2g</sub><sup>1</sup> and A<sub>1g</sub> modes (normalised to Si peak).

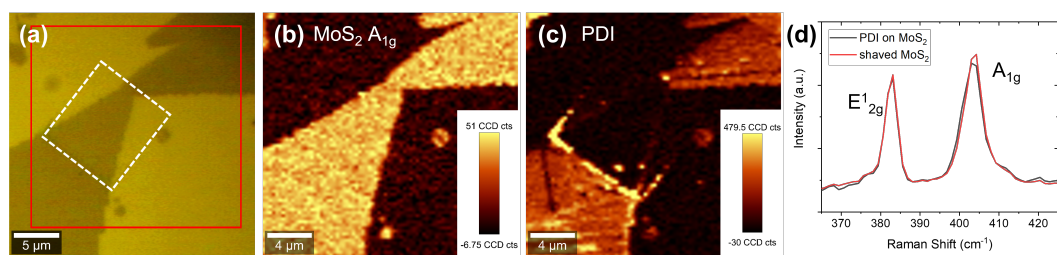


**Figure A.2:** Nanoshaved PDI/MoS<sub>2</sub> heterostructure Raman — (a) Optical image of the PDI/MoS<sub>2</sub> heterostructure area scanned using Raman spectroscopy (red box) with shaved area indicated by white dashed box. (b) Raman peak intensity map of MoS<sub>2</sub> out-of-plane A<sub>1g</sub> (406 cm<sup>-1</sup>) mode. (c) Raman peak intensity map of PDI (~1300 cm<sup>-1</sup>) mode. (d) average Raman spectra comparison of shaved and non-shaved PDI/MoS<sub>2</sub> showing both E<sub>2g</sub><sup>1</sup> and A<sub>1g</sub> modes (normalised to Si peak).

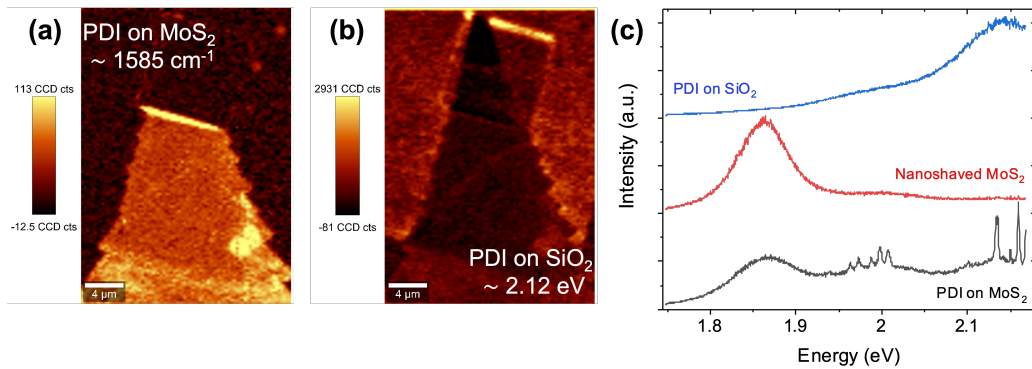


**Figure A.3:** PDI Photoluminescence/Raman — (a) Raman peak intensity map of PDI ( $\sim 1585 \text{ cm}^{-1}$ ) mode. (b) PL peak intensity map of PDI ( $\sim 2.12 \text{ eV}$ ). (c) average PL spectra comparison of PDI on SiO<sub>2</sub>, shaved MoS<sub>2</sub> and non-shaved PDI on MoS<sub>2</sub>.

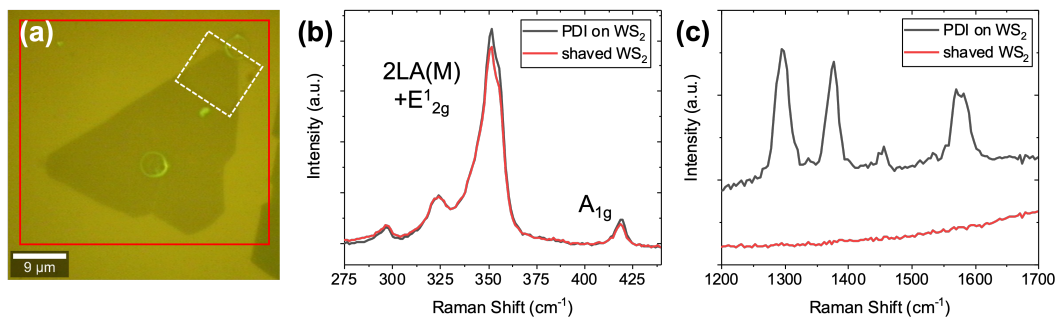


**Figure A.4:** Nanoshaved PDI/WS<sub>2</sub> Heterostructure Raman — (a) Optical image of the PDI/WS<sub>2</sub> area scanned using Raman spectroscopy (red box) with shaved area indicated by white dashed box. (b) average Raman spectra comparison of shaved and non-shaved PDI/WS<sub>2</sub> 2LA(M) + E<sub>2g</sub><sup>1</sup> mode ( $352 \text{ cm}^{-1}$ , normalised to Si peak). (c) average Raman spectra comparison of shaved WS<sub>2</sub> and non-shaved PDI on WS<sub>2</sub> showing characteristic PDI peaks.

## References

- [1] S. Berryman, “Democritus,” in *The Stanford Encyclopedia of Philosophy* (E. N. Zalta, ed.), Metaphysics Research Lab, Stanford University, Winter 2016 ed., 2016.
- [2] S. Bradbury, *The Evolution of the Microscope*. Elsevier Science, 2014.
- [3] W. Croft, *Under The Microscope: A Brief History Of Microscopy*. Series In Popular Science, World Scientific Publishing Company, 2006.
- [4] O. E. Dictionary, “Origin and meaning of microscope.”
- [5] R. Hooke, *Micrographia: Or Some Physiological Descriptions of Minute Bodies Made by Magnifying Glasses, with Observations and Inquiries Thereupon*. Dover phoenix editions, Dover Publications, 2003.
- [6] J. Bardeen and W. H. Brattain, “The transistor, a Semi-Conductor triode,” *Phys. Rev.*, vol. 74, pp. 230–231, July 1948.
- [7] G. E. Moore and Others, “Cramming more components onto integrated circuits,” *IEEE*, vol. 38, no. 114, 1965.
- [8] H. Lee, L.-E. Yu, S.-W. Ryu, J.-W. Han, K. Jeon, D.-Y. Jang, K.-H. Kim, J. Lee, J.-H. Kim, S. Jeon, G. Lee, J. Oh, Y. Park, W. Bae, H. Lee, J. Yang, J. Yoo, S. Kim, and Y.-K. Choi, “Sub-5nm All-Around gate FinFET for ultimate scaling,” in *2006 Symposium on VLSI Technology, 2006. Digest of Technical Papers.*, pp. 58–59, June 2006.
- [9] M. Fuechsle, J. A. Miwa, S. Mahapatra, H. Ryu, and et al., “A single-atom transistor,” *Nature Nanotechnology*, vol. 7, pp. 242 EP –, 02 2012.
- [10] K. S. Novoselov, A. K. Geim, S. V. Morozov, D. Jiang, Y. Zhang, S. V. Dubonos, I. V. Grigorieva, and A. A. Firsov, “Electric field effect in atomically thin carbon films,” *Science*, vol. 306, pp. 666–669, Oct. 2004.
- [11] Q. H. Wang, K. Kalantar-Zadeh, A. Kis, J. N. Coleman, and M. S. Strano, “Electronics and optoelectronics of two-dimensional transition metal dichalcogenides,” *Nat. Nanotechnol.*, vol. 7, pp. 699–712, Nov. 2012.

- [12] K. Wang, J. Wang, J. Fan, M. Lotya, A. O'Neill, D. Fox, and et al., "Ultrafast saturable absorption of two-dimensional MoS<sub>2</sub> nanosheets," *ACS Nano*, vol. 7, pp. 9260–9267, Oct. 2013.
- [13] F. Bonaccorso and Z. Sun, "Solution processing of graphene, topological insulators and other 2d crystals for ultrafast photonics," *Opt. Mater. Express*, vol. 4, p. 63, Jan. 2014.
- [14] W. Zhang, C.-P. Chuu, J.-K. Huang, C.-H. Chen, M.-L. Tsai, Y.-H. Chang, C.-T. Liang, Y.-Z. Chen, Y.-L. Chueh, J.-H. He, M.-Y. Chou, and L.-J. Li, "Ultrahigh-gain photodetectors based on atomically thin graphene-MoS<sub>2</sub> heterostructures," *Sci. Rep.*, vol. 4, p. 3826, Jan. 2014.
- [15] S. Luo, X. Qi, L. Ren, G. Hao, Y. Fan, Y. Liu, W. Han, C. Zang, J. Li, and J. Zhong, "Photoresponse properties of large-area MoS<sub>2</sub> atomic layer synthesized by vapor phase deposition," *J. Appl. Phys.*, vol. 116, p. 164304, Oct. 2014.
- [16] B. Radisavljevic, A. Radenovic, J. Brivio, V. Giacometti, and A. Kis, "Single-layer MoS<sub>2</sub> transistors," *Nat. Nanotechnol.*, vol. 6, pp. 147–150, Mar. 2011.
- [17] G. S. Duesberg, T. Hallam, M. O'Brien, R. Gatensby, H. Kim, K. Lee, N. C. Berner, N. McEvoy, and C. Yim, "Investigation of 2D transition metal dichalcogenide films for electronic devices," in *EUROSOI-ULIS 2015: 2015 Joint International EUROSOI Workshop and International Conference on Ultimate Integration on Silicon*, pp. 73–76, Jan. 2015.
- [18] V. K. Sangwan and M. C. Hersam, "Electronic transport in Two-Dimensional materials," *Annu. Rev. Phys. Chem.*, vol. 69, pp. 299–325, Apr. 2018.
- [19] K. Lee, R. Gatensby, N. McEvoy, T. Hallam, and G. S. Duesberg, "High-performance sensors based on molybdenum disulfide thin films," *Adv. Mater.*, vol. 25, pp. 6699–6702, Dec. 2013.
- [20] S.-Y. Cho, S. J. Kim, Y. Lee, J.-S. Kim, W.-B. Jung, H.-W. Yoo, J. Kim, and H.-T. Jung, "Highly enhanced gas adsorption properties in vertically aligned MoS<sub>2</sub> layers," *ACS Nano*, vol. 9, pp. 9314–9321, Sept. 2015.
- [21] M. Abramowitz and M. W. Davidson, "Introduction to microscopy," *Molecular Expressions*, 2007.
- [22] Bruker, *MultiMode 8-HR User Guide*. Bruker, 2017.
- [23] J. H. Hafner, C. L. Cheung, A. T. Woolley, and C. M. Lieber, "Structural and functional imaging with carbon nanotube AFM probes," *Prog. Biophys. Mol. Biol.*, vol. 77, no. 1, pp. 73–110, 2001.
- [24] Z. Sun, M. P. Boneschanscher, I. Swart, D. Vanmaekelbergh, and P. Liljeroth, "Quantitative atomic force microscopy with carbon monoxide terminated tips," *Phys. Rev. Lett.*, vol. 106, p. 046104, Jan. 2011.

- [25] Q. Zhong, D. Inniss, K. Kjoller, and V. Elings, "Fractured polymer/silica fiber surface studied by tapping mode atomic force microscopy," *Surface Science*, vol. 290, no. L688, 1993.
- [26] J. E. Jones and S. Chapman, "On the determination of molecular fields.—i. from the variation of the viscosity of a gas with temperature," *Proceedings of the Royal Society of London. Series A, Containing Papers of a Mathematical and Physical Character*, vol. 106, pp. 441–462, Oct. 1924.
- [27] G. Haugstad, *Atomic force microscopy: Understanding basic modes and advanced applications*. Hoboken, NJ: Wiley-Blackwell, Sept. 2012.
- [28] J. L. Hutter and J. Bechhoefer, "Calibration of atomic-force microscope tips," *Rev. Sci. Instrum.*, vol. 64, pp. 1868–1873, July 1993.
- [29] M. J. Higgins, R. Proksch, J. E. Sader, M. Polcik, S. Mc Endoo, J. P. Cleveland, and S. P. Jarvis, "Noninvasive determination of optical lever sensitivity in atomic force microscopy," *Rev. Sci. Instrum.*, vol. 77, p. 013701, Jan. 2006.
- [30] Attar, T. Pettersson, and M. W. Rutland, "Thermal calibration of photodiode sensitivity for atomic force microscopy," *Rev. Sci. Instrum.*, vol. 77, p. 116110, Nov. 2006.
- [31] H.-J. Butt and M. Jaschke, "Calculation of thermal noise in atomic force microscopy," *Nanotechnology*, vol. 6, p. 1, Jan. 1995.
- [32] R. W. Stark, T. Drobek, and W. M. Heckl, "Thermomechanical noise of a free v-shaped cantilever for atomic-force microscopy," *Ultramicroscopy*, vol. 86, pp. 207–215, Jan. 2001.
- [33] J. L. Hutter, "Comment on tilt of atomic force microscope cantilevers: effect on spring constant and adhesion measurements," *Langmuir*, vol. 21, pp. 2630–2632, Mar. 2005.
- [34] B. Ohler, "Cantilever spring constant calibration using laser doppler vibrometry," *Rev. Sci. Instrum.*, vol. 78, p. 063701, June 2007.
- [35] H.-J. Butt, B. Cappella, and M. Kappl, "Force measurements with the atomic force microscope: Technique, interpretation and applications," *Surf. Sci. Rep.*, vol. 59, pp. 1–152, Oct. 2005.
- [36] J. Kámán, R. Huszánk, and A. Bonyár, "Towards more reliable AFM force-curve evaluation: A method for spring constant selection, adaptive lever sensitivity calibration and fitting boundary identification," *Micron*, vol. 125, p. 102717, Oct. 2019.
- [37] N. P. D'Costa and J. H. Hoh, "Calibration of optical lever sensitivity for atomic force microscopy," *Rev. Sci. Instrum.*, vol. 66, pp. 5096–5097, Oct. 1995.
- [38] B. Voigtländer, *Scanning Probe Microscopy: Atomic Force Microscopy and Scanning Tunneling Microscopy*. Springer, Feb. 2015.

- [39] Y. Liu, Q. Guo, H.-Y. Nie, W. M. Lau, and J. Yang, "Optimization and calibration of atomic force microscopy sensitivity in terms of tip-sample interactions in high-order dynamic atomic force microscopy," *J. Appl. Phys.*, vol. 106, p. 124507, Dec. 2009.
- [40] L. Kelvin, "V. contact electricity of metals," *The London, Edinburgh, and Dublin Philosophical Magazine and Journal of Science*, vol. 46, pp. 82–120, July 1898.
- [41] M. Nonnenmacher, M. P. O'Boyle, and H. K. Wickramasinghe, "Kelvin probe force microscopy," *Appl. Phys. Lett.*, vol. 58, pp. 2921–2923, June 1991.
- [42] S. Sadewasser and T. Glatzel, *Kelvin Probe Force Microscopy: From Single Charge Detection to Device Characterization*. Springer, Cham, 2018.
- [43] C. Sommerhalter, T. Glatzel, T. W. Matthes, A. Jäger-Waldau, and M. C. Lux-Steiner, "Kelvin probe force microscopy in ultra high vacuum using amplitude modulation detection of the electrostatic forces," *Appl. Surf. Sci.*, vol. 157, pp. 263–268, Apr. 2000.
- [44] H. O. Jacobs, P. Leuchtman, O. J. Homan, and A. Stemmer, "Resolution and contrast in kelvin probe force microscopy," *J. Appl. Phys.*, vol. 84, pp. 1168–1173, Aug. 1998.
- [45] S. Y. Luchkin and K. J. Stevenson, "On the origin of extended resolution in kelvin probe force microscopy with a worn tip apex," *Microsc. Microanal.*, vol. 24, pp. 126–131, Apr. 2018.
- [46] A. Kikukawa, S. Hosaka, and R. Imura, "Silicon pn junction imaging and characterizations using sensitivity enhanced kelvin probe force microscopy," *Appl. Phys. Lett.*, vol. 66, pp. 3510–3512, June 1995.
- [47] R. Garcia, A. W. Knoll, and E. Riedo, "Advanced scanning probe lithography," *Nat. Nanotechnol.*, vol. 9, pp. 577–587, Aug. 2014.
- [48] Y. Yan, S. Chang, T. Wang, and Y. Geng, "Scratch on polymer materials using AFM Tip-Based approach: A review," *Polymers*, vol. 11, Sept. 2019.
- [49] T. Michels and I. W. Rangelow, "Review of scanning probe micromachining and its applications within nanoscience," *Microelectron. Eng.*, vol. 126, pp. 191–203, Aug. 2014.
- [50] O. El Zubir, I. Barlow, G. J. Leggett, and N. H. Williams, "Fabrication of molecular nanopatterns at aluminium oxide surfaces by nanoshaving of self-assembled monolayers of alkylphosphonates," *Nanoscale*, vol. 5, pp. 11125–11131, Nov. 2013.
- [51] Y. Yan, Y. Geng, and Z. Hu, "Recent advances in AFM tip-based nanomechanical machining," *Int. J. Mach. Tools Manuf.*, vol. 99, pp. 1–18, Dec. 2015.
- [52] F. Zhang, D. Edwards, X. Deng, Y. Wang, J. I. Kilpatrick, N. Bassiri-Gharb, A. Kumar, D. Chen, X. Gao, and B. J. Rodriguez, "Investigation of AFM-based machining of ferroelectric thin films at the nanoscale," *J. Appl. Phys.*, vol. 127, p. 034103, Jan. 2020.

- [53] P. T. Mathew, B. J. Rodriguez, and F. Fang, "Atomic and Close-to-Atomic scale manufacturing: A review on atomic layer removal methods using atomic force microscopy," *Nanomanufacturing and Metrology*, vol. 3, pp. 167–186, Sept. 2020.
- [54] H. Göbel and P. von Blanckenhagen, "Atomic force microscope as a tool for metal surface modifications," *J. Vac. Sci. Technol. B Microelectron. Nanometer Struct. Process. Meas. Phenom.*, vol. 13, pp. 1247–1251, May 1995.
- [55] S. Z. Butler, S. M. Hollen, L. Cao, and et al., "Progress, challenges, and opportunities in two-dimensional materials beyond graphene," *ACS Nano*, vol. 7, pp. 2898–2926, Mar 2013.
- [56] M. C. Hersam, "Emerging device applications for two-dimensional nanomaterial heterostructures," in *2015 73rd Annual Device Research Conference (DRC)*, pp. 209–209, [ieeexplore.ieee.org](http://ieeexplore.ieee.org), June 2015.
- [57] G.-Y. Zhao, H. Deng, N. Tyree, M. Guy, A. Lisfi, Q. Peng, J.-A. Yan, C. Wang, and Y. Lan, "Recent progress on Irradiation-Induced defect engineering of Two-Dimensional 2H-MoS<sub>2</sub> few layers," *NATO Adv. Sci. Inst. Ser. E Appl. Sci.*, vol. 9, p. 678, Feb. 2019.
- [58] A. Hijazi and A. E. Moutaouakil, "Graphene and MoS<sub>2</sub> structures for THz applications," in *2019 44th International Conference on Infrared, Millimeter, and Terahertz Waves (IRMMW-THz)*, pp. 1–2, [ieeexplore.ieee.org](http://ieeexplore.ieee.org), Sept. 2019.
- [59] J. A. del Alamo, "Nanometer-scale III–V CMOS," in *2016 Compound Semiconductor Week (CSW) [Includes 28th International Conference on Indium Phosphide & Related Materials (IPRM) & 43rd International Symposium on Compound Semiconductors (ISCS)*, IEEE, June 2016.
- [60] C. Tan and H. Zhang, "Two-dimensional transition metal dichalcogenide nanosheet-based composites," *Chem. Soc. Rev.*, vol. 44, pp. 2713–2731, May 2015.
- [61] D. Jariwala, V. K. Sangwan, L. J. Lauhon, T. J. Marks, and M. C. Hersam, "Emerging device applications for semiconducting two-dimensional transition metal dichalcogenides," *ACS Nano*, vol. 8, no. 2, pp. 1102–1120, 2014. PMID: 24476095.
- [62] M. Chhowalla, H. S. Shin, G. Eda, L.-J. Li, K. P. Loh, and H. Zhang, "The chemistry of two-dimensional layered transition metal dichalcogenide nanosheets," *Nat. Chem.*, vol. 5, pp. 263–275, Apr. 2013.
- [63] J. A. Wilson and A. D. Yoffe, "The transition metal dichalcogenides discussion and interpretation of the observed optical, electrical and structural properties," *Adv. Phys.*, vol. 18, pp. 193–335, May 1969.
- [64] K. F. Mak, C. Lee, J. Hone, J. Shan, and T. F. Heinz, "Atomically thin MoS<sub>2</sub>: a new direct-gap semiconductor," *Phys. Rev. Lett.*, vol. 105, p. 136805, Sept. 2010.



- [65] K. C. Santosh, C. Zhang, S. Hong, R. M. Wallace, and K. Cho, "Phase stability of transition metal dichalcogenide by competing ligand field stabilization and charge density wave," *2D Mater.*, vol. 2, p. 035019, Sept. 2015.
- [66] A. Splendiani, L. Sun, Y. Zhang, T. Li, J. Kim, C.-Y. Chim, G. Galli, and F. Wang, "Emerging photoluminescence in monolayer MoS<sub>2</sub>," *Nano Lett.*, vol. 10, pp. 1271–1275, Apr. 2010.
- [67] G. Eda, H. Yamaguchi, D. Voiry, T. Fujita, M. Chen, and M. Chhowalla, "Photoluminescence from chemically exfoliated MoS<sub>2</sub>," *Nano Lett.*, vol. 11, pp. 5111–5116, Dec. 2011.
- [68] H. Terrones, F. López-Urías, and M. Terrones, "Novel hetero-layered materials with tunable direct band gaps by sandwiching different metal disulfides and diselenides," *Sci. Rep.*, vol. 3, p. 1549, 2013.
- [69] H. R. Gutiérrez, N. Perea-López, A. L. Elías, A. Berkdemir, B. Wang, R. Lv, F. López-Urías, V. H. Crespi, H. Terrones, and M. Terrones, "Extraordinary room-temperature photoluminescence in triangular WS<sub>2</sub> monolayers," *Nano Lett.*, vol. 13, pp. 3447–3454, Aug. 2013.
- [70] M. Samadi, N. Sarikhani, M. Zirak, H. Zhang, H.-L. Zhang, and A. Z. Moshfegh, "Group 6 transition metal dichalcogenide nanomaterials: synthesis, applications and future perspectives," *Nanoscale Horiz.*, vol. 3, pp. 90–204, Mar. 2018.
- [71] C. Lan, C. Li, J. C. Ho, and Y. Liu, "2D WS<sub>2</sub> : From vapor phase synthesis to device applications," *Adv. Electron. Mater.*, vol. 7, p. 2000688, July 2021.
- [72] C. Yim, K. Lee, N. McEvoy, M. O'Brien, S. Riazimehr, N. C. Berner, C. P. Cullen, and et al., "High-performance hybrid electronic devices from layered ptse<sub>2</sub> films grown at low temperature," *ACS Nano*, vol. 10, no. 10, pp. 9550–9558, 2016. PMID: 27661979.
- [73] H. Zheng, Y. Choi, F. Baniasadi, D. Hu, L. Jiao, K. Park, and C. Tao, "Intrinsic Point Defects in Ultrathin 1T-PtSe<sub>2</sub> Layers," *ArXiv e-prints*, Aug. 2018.
- [74] Y. Wang, L. Li, W. Yao, S. Song, J. T. Sun, J. Pan, X. Ren, C. Li, and et al., "Monolayer ptse<sub>2</sub>, a new semiconducting transition-metal-dichalcogenide, epitaxially grown by direct selenization of pt," *Nano Letters*, vol. 15, no. 6, pp. 4013–4018, 2015. PMID: 25996311.
- [75] A. Kandemir, B. Akbali, Z. Kahraman, S. V. Badalov, M. Ozcan, F. Iyikanat, and H. Sahin, "Structural, electronic and phononic properties of ptse<sub>2</sub>: from monolayer to bulk," *Semiconductor Science and Technology*, vol. 33, p. 085002, Jun 2018.
- [76] M. O'Brien, N. McEvoy, C. Motta, J.-Y. Zheng, N. C. Berner, J. Kotakoski, K. Elibol, T. J. Pennycook, J. C. Meyer, C. Yim, M. Abid, T. Hallam, J. F. Donegan, S. Sanvito, and G. S. Duesberg, "Raman characterization of platinum diselenide thin films," *2D Mater.*, vol. 3, p. 021004, Apr. 2016.

- [77] P. Miró, M. Ghorbani-Asl, and T. Heine, “Two dimensional materials beyond MoS<sub>2</sub>: noble-transition-metal dichalcogenides,” *Angew. Chem. Int. Ed Engl.*, vol. 53, pp. 3015–3018, Mar. 2014.
- [78] Z. Huang, W. Zhang, and W. Zhang, “Computational search for Two-Dimensional MX<sub>2</sub> semiconductors with possible high electron mobility at room temperature,” *Materials*, vol. 9, Aug. 2016.
- [79] Y. Zhao, J. Qiao, Z. Yu, P. Yu, K. Xu, S. P. Lau, W. Zhou, Z. Liu, X. Wang, W. Ji, and Y. Chai, “High-Electron-Mobility and Air-Stable 2D layered PtSe<sub>2</sub> FETs,” *Adv. Mater.*, vol. 29, Feb. 2017.
- [80] N. Rohaizad, C. C. Mayorga-Martinez, Z. Sofer, R. D. Webster, and M. Pumera, “Layered platinum dichalcogenides (PtS<sub>2</sub>, PtSe<sub>2</sub>, PtTe<sub>2</sub>) for non-enzymatic electrochemical sensor,” *Applied Materials Today*, vol. 19, p. 100606, June 2020.
- [81] Y. Zhao, J. Qiao, P. Yu, Z. Hu, Z. Lin, S. P. Lau, Z. Liu, W. Ji, and Y. Chai, “Extraordinarily strong interlayer interaction in 2d layered pts<sub>2</sub>,” *Advanced Materials*, vol. 28, pp. 2399–2407, Feb 2016.
- [82] E. Gao, S.-Z. Lin, Z. Qin, M. J. Buehler, X.-Q. Feng, and Z. Xu, “Mechanical exfoliation of two-dimensional materials,” *Journal of the Mechanics and Physics of Solids*, vol. 115, pp. 248 – 262, 2018.
- [83] G. Z. Magda, J. Petó, G. Dobrik, C. Hwang, L. P. Biró, and L. Tapasztó, “Exfoliation of large-area transition metal chalcogenide single layers,” *Scientific Reports*, vol. 5, Oct 2015.
- [84] S. B. Desai, S. R. Madhvapathy, M. Amani, and et al., “Gold-mediated exfoliation of ultralarge optoelectronically-perfect monolayers,” *Advanced Materials*, vol. 28, pp. 4053–4058, Mar 2016.
- [85] K. S. Novoselov and A. H. Castro Neto, “Two-dimensional crystals-based heterostructures: materials with tailored properties,” *Phys. Scr.*, vol. 2012, p. 014006, Jan. 2012.
- [86] J. N. Coleman, M. Lotya, A. O’Neill, and et al., “Two-dimensional nanosheets produced by liquid exfoliation of layered materials,” *Science*, vol. 331, pp. 568–571, Feb 2011.
- [87] V. Nicolosi, M. Chhowalla, M. G. Kanatzidis, M. S. Strano, and J. N. Coleman, “Liquid exfoliation of layered materials,” *Science*, vol. 340, pp. 1226419–1226419, Jun 2013.
- [88] K. R. Paton, E. Varrla, C. Backes, R. J. Smith, U. Khan, and A. e. a. O’Neill, “Scalable production of large quantities of defect-free few-layer graphene by shear exfoliation in liquids,” *Nat. Mater.*, vol. 13, pp. 624–630, June 2014.

- [89] C. Backes, R. J. Smith, N. McEvoy, and et al., “Edge and confinement effects allow in situ measurement of size and thickness of liquid-exfoliated nanosheets,” *Nat. Commun.*, vol. 5, p. 4576, Aug. 2014.
- [90] D. J. Finn, M. Lotya, G. Cunningham, R. J. Smith, and et al., “Inkjet deposition of liquid-exfoliated graphene and MoS<sub>2</sub> nanosheets for printed device applications,” *J. Mater. Chem.*, vol. 2, no. 5, pp. 925–932, 2014.
- [91] A. C. Ferrari, F. Bonaccorso, V. Fal’ko, K. S. Novoselov, and et al., “Science and technology roadmap for graphene, related two-dimensional crystals, and hybrid systems,” *Nanoscale*, vol. 7, pp. 4598–4810, Mar. 2015.
- [92] J.-H. Park and T. S. Sudarshan, *Chemical Vapour Deposition*. ASM International, 2001.
- [93] M. O’Brien, N. McEvoy, T. Hallam, H.-Y. Kim, N. C. Berner, D. Hanlon, K. Lee, J. N. Coleman, and G. S. Duesberg, “Transition metal dichalcogenide growth via close proximity precursor supply,” *Sci. Rep.*, vol. 4, p. 7374, Dec. 2014.
- [94] R. Gatensby, N. McEvoy, K. Lee, T. Hallam, and et al., “Controlled synthesis of transition metal dichalcogenide thin films for electronic applications,” *Appl. Surf. Sci.*, vol. 297, pp. 139–146, Apr. 2014.
- [95] D. Kong, H. Wang, J. J. Cha, M. Pasta, K. J. Koski, J. Yao, and Y. Cui, “Synthesis of MoS<sub>2</sub> and MoSe<sub>2</sub> films with vertically aligned layers,” *Nano Lett.*, vol. 13, pp. 1341–1347, Mar. 2013.
- [96] C. Yim, V. Passi, M. C. Lemme, G. S. Duesberg, C. Ó Coileáin, E. Pallecchi, D. Fadil, and N. McEvoy, “Electrical devices from top-down structured platinum diselenide films,” *npj 2D Materials and Applications*, vol. 2, p. 5, Feb. 2018.
- [97] S. Presolski and M. Pumera, “Covalent functionalization of MoS<sub>2</sub>,” *Mater. Today*, vol. 19, pp. 140–145, Apr. 2016.
- [98] X. Chen and A. R. McDonald, “Functionalization of Two-Dimensional Transition-Metal dichalcogenides,” *Adv. Mater.*, vol. 28, pp. 5738–5746, July 2016.
- [99] H. Kim, W. Kim, M. O’Brien, N. McEvoy, C. Yim, M. Marcia, F. Hauke, A. Hirsch, G.-T. Kim, and G. S. Duesberg, “Optimized single-layer MoS<sub>2</sub> field-effect transistors by non-covalent functionalisation,” *Nanoscale*, vol. 10, pp. 17557–17566, Sept. 2018.
- [100] K. C. Knirsch, N. C. Berner, H. C. Nerl, C. S. Cucinotta, Z. Gholamvand, N. McEvoy, Z. Wang, I. Abramovic, P. Vecera, M. Halik, S. Sanvito, G. S. Duesberg, V. Nicolosi, F. Hauke, A. Hirsch, J. N. Coleman, and C. Backes, “Basal-Plane functionalization of chemically exfoliated molybdenum disulfide by diazonium salts,” *ACS Nano*, vol. 9, pp. 6018–6030, June 2015.

- [101] A. Kumar, K. Banerjee, and P. Liljeroth, “Molecular assembly on two-dimensional materials,” *Nanotechnology*, vol. 28, p. 082001, Feb. 2017.
- [102] R. Tilmann, C. Weiß, C. P. Cullen, L. Peters, O. Hartwig, L. Höltgen, T. Stimpel-Lindner, K. C. Knirsch, N. McEvoy, A. Hirsch, and G. S. Duesberg, “Highly selective non-covalent on-chip functionalization of layered materials,” *Adv. Electron. Mater.*, p. 2000564, Jan. 2021.
- [103] D. Cornil and J. Cornil, “Work-function modification of the (111) gold surface upon deposition of self-assembled monolayers based on alkanethiol derivatives,” *J. Electron Spectrosc. Relat. Phenom.*, vol. 189, pp. 32–38, Aug. 2013.
- [104] J. C. Love, L. A. Estroff, J. K. Kriebel, R. G. Nuzzo, and G. M. Whitesides, “Self-assembled monolayers of thiolates on metals as a form of nanotechnology,” *Chem. Rev.*, vol. 105, pp. 1103–1169, Apr. 2005.
- [105] A. Ulman, “Formation and structure of Self-Assembled monolayers,” *Chem. Rev.*, vol. 96, pp. 1533–1554, June 1996.
- [106] B. Lee, Y. Chen, F. Duerr, D. Mastrogiovanni, E. Garfunkel, E. Y. Andrei, and V. Podzorov, “Modification of electronic properties of graphene with self-assembled monolayers,” *Nano Lett.*, vol. 10, pp. 2427–2432, July 2010.
- [107] T. Kawanago and S. Oda, “Utilizing self-assembled-monolayer-based gate dielectrics to fabricate molybdenum disulfide field-effect transistors,” *Appl. Phys. Lett.*, vol. 108, p. 041605, Jan. 2016.
- [108] C. M. Lieber and Y. Kim, “Nanomachining and manipulation with the atomic force microscope,” *Adv. Mater.*, vol. 5, pp. 392–394, May 1993.
- [109] Y. Kim and C. M. Lieber, “Machining oxide thin films with an atomic force microscope: pattern and object formation on the nanometer scale,” *Science*, vol. 257, pp. 375–377, July 1992.
- [110] S. S. Hong, W. Kundhikanjana, J. J. Cha, K. Lai, D. Kong, S. Meister, M. A. Kelly, Z.-X. Shen, and Y. Cui, “Ultrathin topological insulator Bi<sub>2</sub>Se<sub>3</sub> nanoribbons exfoliated by atomic force microscopy,” *Nano Lett.*, vol. 10, pp. 3118–3122, Aug. 2010.
- [111] X. Liu, K.-S. Chen, S. A. Wells, I. Balla, J. Zhu, J. D. Wood, and M. C. Hersam, “Scanning probe nanopatterning and Layer-by-Layer thinning of black phosphorus,” *Adv. Mater.*, vol. 29, Jan. 2017.
- [112] M. Donarelli, F. Perrozzi, F. Bisti, F. Paparella, V. Feyer, A. Ponzoni, M. Gonchigsuren, and L. Ottaviano, “Few layered MoS<sub>2</sub> lithography with an AFM tip: description of the technique and nanospectroscopy investigations,” *Nanoscale*, vol. 7, pp. 11453–11459, July 2015.

- [113] Z. Li, S. Yang, R. Dhall, E. Kosmowska, H. Shi, I. Chatzakis, and S. B. Cronin, "Layer control of WSe<sub>2</sub> via selective surface layer oxidation," *ACS Nano*, vol. 10, pp. 6836–6842, July 2016.
- [114] H. Zhu, X. Qin, L. Cheng, A. Azcatl, J. Kim, and R. M. Wallace, "Remote plasma oxidation and atomic layer etching of MoS<sub>2</sub>," *ACS Appl. Mater. Interfaces*, vol. 8, pp. 19119–19126, July 2016.
- [115] X. Zheng, Y. Wei, C. Deng, H. Huang, Y. Yu, G. Wang, G. Peng, Z. Zhu, Y. Zhang, T. Jiang, S. Qin, R. Zhang, and X. Zhang, "Controlled Layer-by-Layer oxidation of MoTe<sub>2</sub> via O<sub>3</sub> exposure," *ACS Appl. Mater. Interfaces*, vol. 10, pp. 30045–30050, Sept. 2018.
- [116] V. K. Nagareddy, T. J. Octon, N. J. Townsend, S. Russo, M. F. Craciun, and C. D. Wright, "Humidity-Controlled ultralow power Layer-by-Layer thinning, nanopatterning and bandgap engineering of MoTe<sub>2</sub>," *Adv. Funct. Mater.*, vol. 20, p. 1804434, Nov. 2018.
- [117] A. Castellanos-Gomez, M. Barkelid, A. M. Goossens, V. E. Calado, H. S. J. van der Zant, and G. A. Steele, "Laser-thinning of mos<sub>2</sub>: on demand generation of a single-layer semiconductor," *Nano Lett.*, vol. 12, pp. 3187–3192, June 2012.
- [118] L. Hu, X. Shan, Y. Wu, J. Zhao, and X. Lu, "Laser thinning and patterning of MoS<sub>2</sub> with Layer-by-Layer precision," *Sci. Rep.*, vol. 7, p. 15538, Nov. 2017.
- [119] W. Shockley, "A unipolar "field-effect" transistor," *Proceedings of the IRE*, vol. 40, no. 11, pp. 1365–1376, 1952.
- [120] R. G. Arns, "The other transistor: early history of the metal-oxide semiconductor field-effect transistor," *Engineering Science & Education Journal*, vol. 7, pp. 233–240, Oct. 1998.
- [121] S. M. Sze and M.-K. Lee, *Semiconductor devices: Physics and technology*. Chichester, England: John Wiley & Sons, 3 ed., Apr. 2012.
- [122] C. Buttay, "Lateral mosfet."
- [123] S. M. Sze and K. K. Ng, *Physics of Semiconductor Devices*. Wiley, 2007.
- [124] C. Kumar, S. Das, and S. Jit, "Device physics and device integration of two-dimensional heterostructures," in *2D Nanoscale Heterostructured Materials* (S. Jit and S. Das, eds.), Micro and Nano Technologies, pp. 195–214, Elsevier, 2020.
- [125] M. Z. Bellus, M. Li, S. D. Lane, F. Ceballos, Q. Cui, X. C. Zeng, and H. Zhao, "Type-I van der waals heterostructure formed by MoS<sub>2</sub> and ReS<sub>2</sub> monolayers," *Nanoscale Horiz*, vol. 2, pp. 31–36, Jan. 2017.
- [126] B. You, X. Wang, Z. Zheng, and W. Mi, "Black phosphorene/monolayer transition-metal dichalcogenides as two dimensional van der waals heterostructures: a first-principles study," *Phys. Chem. Chem. Phys.*, vol. 18, pp. 7381–7388, Mar. 2016.

- [127] W. Hu and J. Yang, “Two-dimensional van der waals heterojunctions for functional materials and devices,” *J. Mater. Chem.*, vol. 5, pp. 12289–12297, Dec. 2017.
- [128] S. Seo, S. Kim, H. Choi, J. Lee, H. Yoon, G. Piao, J.-C. Park, Y. Jung, J. Song, S. Y. Jeong, H. Park, and S. Lee, “Direct in situ growth of Centimeter-Scale Multi-Heterojunction MoS<sub>2</sub>/WS<sub>2</sub>/WSe<sub>2</sub> Thin-Film catalyst for Photo-Electrochemical hydrogen evolution,” *Adv. Sci.*, vol. 6, p. 1900301, July 2019.
- [129] C.-W. Yang, H.-L. Tang, S. Sattar, M.-H. Chiu, Y. Wan, C.-H. Chen, J. Kong, K.-W. Huang, L.-J. Li, and V. Tung, “Epitaxial growth and determination of band alignment of Bi<sub>2</sub>Te<sub>3</sub>-WSe<sub>2</sub> vertical van der waals heterojunctions,” *ACS Materials Lett.*, vol. 2, pp. 1351–1359, Oct. 2020.
- [130] S. Banerjee, L. Cao, Y. S. Ang, L. K. Ang, and P. Zhang, “Reducing contact resistance in Two-Dimensional-Material-Based electrical contacts by roughness engineering,” *Phys. Rev. Applied*, vol. 13, p. 064021, June 2020.
- [131] H. Liu, A. T. Neal, and P. D. Ye, “Channel length scaling of mos<sub>2</sub> mosfets,” *ACS Nano*, vol. 6, no. 10, pp. 8563–8569, 2012. PMID: 22957650.
- [132] M. Ghorbani-Asl, A. Kuc, P. Miró, and T. Heine, “A single-material logical junction based on 2d crystal pds<sub>2</sub>,” *Advanced Materials*, vol. 28, pp. 853–856, Dec 2015.
- [133] O. Lopez-Sanchez, D. Lembke, M. Kayci, A. Radenovic, and A. Kis, “Ultrasensitive photodetectors based on monolayer mos<sub>2</sub>,” *Nature Nanotechnology*, vol. 8, pp. 497–501, Jun 2013.
- [134] D. Krasnozhan, D. Lembke, C. Nyffeler, Y. Leblebici, and A. Kis, “Mos<sub>2</sub> transistors operating at gigahertz frequencies,” *Nano Letters*, vol. 14, pp. 5905–5911, Sep 2014.
- [135] A. Allain, J. Kang, K. Banerjee, and A. Kis, “Electrical contacts to two-dimensional semiconductors,” *Nat. Mater.*, vol. 14, pp. 1195–1205, Dec. 2015.
- [136] J. Kang, W. Liu, D. Sarkar, D. Jena, and K. Banerjee, “Computational study of metal contacts to monolayer Transition-Metal dichalcogenide semiconductors,” *Phys. Rev. X*, vol. 4, p. 031005, July 2014.
- [137] C. V. Raman and R. S. F., “A new radiation.” <http://repository.ias.ac.in/70648/1/36-PUB.pdf>, 1928. Accessed: 2021-7-23.
- [138] J. R. Ferraro, K. Nakamoto, and C. W. Brown, *Introductory Raman Spectroscopy*. Elsevier, 2 ed., 2003.
- [139] K. Sharp and F. Matschinsky, “Translation of ludwig boltzmann’s paper “on the relationship between the second fundamental theorem of the mechanical theory of heat and probability calculations regarding the conditions for thermal equilibrium” sitzungberichte der kaiserlichen

- akademie der wissenschaften. Mathematisch-Naturwissen classe. abt. II, LXXVI 1877, pp 373-435 (wien. ber. 1877, 76:373-435). reprinted in wiss. abhandlungen, vol. II, reprint 42, p. 164-223, barth, leipzig, 1909," *Entropy*, vol. 17, pp. 1971–2009, Apr. 2015.
- [140] K. Nakamoto, *Infrared and Raman Spectra of Inorganic and Coordination Compounds, Part B: Applications in Coordination, Organometallic, and Bioinorganic Chemistry*. Infrared and Raman Spectra of Inorganic and Coordination Compounds, Wiley, 2009.
- [141] T. H. Kauffmann, N. Kokanyan, and M. D. Fontana, "Use of stokes and anti-stokes raman scattering for new applications," *J. Raman Spectrosc.*, vol. 50, pp. 418–424, Mar. 2019.
- [142] X. Zhang, X.-F. Qiao, W. Shi, J.-B. Wu, D.-S. Jiang, and P.-H. Tan, "Phonon and raman scattering of two-dimensional transition metal dichalcogenides from monolayer, multilayer to bulk material," *Chemical Society Reviews*, vol. 44, no. 9, pp. 2757–2785, 2015.
- [143] N. Scheuschner, R. Gillen, M. Staiger, and J. Maultzsch, "Interlayer resonant raman modes in few-layer MoS<sub>2</sub>," *Phys. Rev. B Condens. Matter Mater. Phys.*, vol. 91, June 2015.
- [144] X. Zhang, W. P. Han, J. B. Wu, S. Milana, Y. Lu, Q. Q. Li, A. C. Ferrari, and P. H. Tan, "Raman spectroscopy of shear and layer breathing modes in multilayer MoS<sub>2</sub>," *Phys. Rev. B Condens. Matter*, vol. 87, p. 115413, Mar. 2013.
- [145] M. O'Brien, N. McEvoy, D. Hanlon, T. Hallam, J. N. Coleman, and G. S. Duesberg, "Mapping of Low-Frequency raman modes in CVD-Grown transition metal dichalcogenides: Layer number, stacking orientation and resonant effects," *Sci. Rep.*, vol. 6, p. 19476, Jan. 2016.
- [146] X. Chen, S. Zhang, L. Wang, Y.-F. Huang, H. Liu, J. Huang, N. Dong, W. Liu, I. M. Kislyakov, J. M. Nunzi, L. Zhang, and J. Wang, "Direct observation of interlayer coherent acoustic phonon dynamics in bilayer and few-layer PtSe<sub>2</sub>," *Photon. Res., PRJ*, vol. 7, pp. 1416–1424, Dec. 2019.
- [147] M. Staiger, R. Gillen, N. Scheuschner, O. Ochedowski, F. Kampmann, M. Schleberger, C. Thomsen, and J. Maultzsch, "Splitting of monolayer out-of-plane A<sub>1</sub>' Raman mode in few-layer WS<sub>2</sub>," *Phys. Rev. B Condens. Matter Mater. Phys.*, vol. 91, May 2015.
- [148] Y. Zhao, X. Luo, H. Li, J. Zhang, P. T. Araujo, C. K. Gan, J. Wu, H. Zhang, S. Y. Quek, M. S. Dresselhaus, and Q. Xiong, "Interlayer breathing and shear modes in few-trilayer MoS<sub>2</sub> and WSe<sub>2</sub>," *Nano Lett.*, vol. 13, pp. 1007–1015, Mar. 2013.
- [149] H. Li, Q. Zhang, C. C. R. Yap, B. K. Tay, T. H. T. Edwin, A. Olivier, and D. Baillargeat, "From bulk to monolayer MoS<sub>2</sub>: Evolution of raman scattering," *Adv. Funct. Mater.*, vol. 22, pp. 1385–1390, Apr. 2012.
- [150] N. Scheuschner, O. Ochedowski, M. Schleberger, and J. Maultzsch, "Resonant raman profiles and  $\mu$ -photoluminescence of atomically thin layers of molybdenum disulfide," *Phys. Status Solidi B Basic Res.*, vol. 249, pp. 2644–2647, Dec. 2012.

- [151] A. Berkdemir, H. R. Gutiérrez, A. R. Botello-Méndez, N. Perea-López, A. L. Elías, C.-I. Chia, B. Wang, V. H. Crespi, F. López-Urías, J.-C. Charlier, H. Terrones, and M. Terrones, “Identification of individual and few layers of WS<sub>2</sub> using raman spectroscopy,” *Sci. Rep.*, vol. 3, Dec. 2013.
- [152] C. S. S. Kumar, *UV-VIS and Photoluminescence Spectroscopy for Nanomaterials Characterization*. Berlin, Germany: Springer Berlin Heidelberg, 2013 ed., Mar. 2013.
- [153] Andrews D.L., Scholes G.D., Wiederrecht G.P., ed., *Comprehensive Nanoscience and Technology*, vol. 4 of *Comprehensive Nanoscience and Technology*. Academic Press, Oct. 2010.
- [154] S. Sim, J. Park, J.-G. Song, C. In, Y.-S. Lee, H. Kim, and H. Choi, “Exciton dynamics in atomically thin MoS<sub>2</sub>: Interexcitonic interaction and broadening kinetics,” *Phys. Rev. B Condens. Matter*, vol. 88, p. 075434, Aug. 2013.
- [155] G. Bassani, G. Liedl, and P. Wyder, *Encyclopedia of Condensed Matter Physics*. No. v. 1 in *Encyclopedia of Condensed Matter Physics*, Academic, 2005.
- [156] V. Senthilkumar, L. C. Tam, Y. S. Kim, Y. Sim, M.-J. Seong, and J. I. Jang, “Direct vapor phase growth process and robust photoluminescence properties of large area MoS<sub>2</sub> layers,” *Nano Res.*, vol. 7, pp. 1759–1768, Dec. 2014.
- [157] C. Klingshirn, *Semiconductor Optics*. Graduate Texts in Physics, Springer Berlin Heidelberg, 2012.
- [158] F. Cadiz, E. Courtade, C. Robert, G. Wang, Y. Shen, H. Cai, T. Taniguchi, K. Watanabe, H. Carrere, D. Lagarde, M. Manca, T. Amand, P. Renucci, S. Tongay, X. Marie, and B. Urbaszek, “Excitonic linewidth approaching the homogeneous limit in MoS<sub>2</sub>-Based van der waals heterostructures,” *Phys. Rev. X*, vol. 7, p. 021026, May 2017.
- [159] T. Verhagen, V. L. P. Guerra, G. Haider, M. Kalbac, and J. Vejpravova, “Towards the evaluation of defects in MoS<sub>2</sub> using cryogenic photoluminescence spectroscopy,” *Nanoscale*, vol. 12, pp. 3019–3028, Feb. 2020.
- [160] Y. Y. Hui, X. Liu, W. Jie, N. Y. Chan, J. Hao, Y.-T. Hsu, L.-J. Li, W. Guo, and S. P. Lau, “Exceptional tunability of band energy in a compressively strained trilayer MoS<sub>2</sub> sheet,” *ACS Nano*, vol. 7, pp. 7126–7131, Aug. 2013.
- [161] H. J. Conley, B. Wang, J. I. Ziegler, R. F. Haglund, Jr, S. T. Pantelides, and K. I. Bolotin, “Bandgap engineering of strained monolayer and bilayer MoS<sub>2</sub>,” *Nano Lett.*, vol. 13, pp. 3626–3630, Aug. 2013.
- [162] Y. Guo, B. Li, Y. Huang, S. Du, C. Sun, H. Luo, B. Liu, X. Zhou, J. Yang, J. Li, and C. Gu, “Direct bandgap engineering with local biaxial strain in few-layer MoS<sub>2</sub> bubbles,” *Nano Res.*, vol. 13, pp. 2072–2078, Aug. 2020.



- [163] Y. Lin, X. Ling, L. Yu, S. Huang, A. L. Hsu, Y.-H. Lee, J. Kong, M. S. Dresselhaus, and T. Palacios, "Dielectric screening of excitons and trions in single-layer MoS<sub>2</sub>," *Nano Lett.*, vol. 14, pp. 5569–5576, Oct. 2014.
- [164] S. Tongay, J. Suh, C. Ataca, W. Fan, A. Luce, J. S. Kang, J. Liu, C. Ko, R. Raghunathanan, J. Zhou, F. Ogletree, J. Li, J. C. Grossman, and J. Wu, "Defects activated photoluminescence in two-dimensional semiconductors: interplay between bound, charged, and free excitons," *Sci. Rep.*, vol. 3, p. 2657, 2013.
- [165] Z. Lin, B. R. Carvalho, E. Kahn, R. Lv, R. Rao, H. Terrones, M. A. Pimenta, and M. Terrones, "Defect engineering of two-dimensional transition metal dichalcogenides," *2D Mater.*, vol. 3, p. 022002, Apr. 2016.
- [166] S.-S. Chee, W.-J. Lee, Y.-R. Jo, M. K. Cho, D. Chun, H. Baik, B.-J. Kim, M.-H. Yoon, K. Lee, and M.-H. Ham, "Atomic vacancy control and elemental substitution in a monolayer molybdenum disulfide for high performance optoelectronic device arrays," *Adv. Funct. Mater.*, vol. 30, p. 1908147, Mar. 2020.
- [167] M. Buscema, G. A. Steele, H. S. J. van der Zant, and A. Castellanos-Gomez, "The effect of the substrate on the raman and photoluminescence emission of single-layer MoS<sub>2</sub>," *Nano Res.*, vol. 7, pp. 561–571, Apr. 2014.
- [168] L. Wang, Z. N. Nilsson, M. Tahir, H. Chen, and J. B. Sambur, "Influence of the substrate on the optical and photo-electrochemical properties of monolayer MoS<sub>2</sub>," *ACS Appl. Mater. Interfaces*, vol. 12, pp. 15034–15042, Apr. 2020.
- [169] M. Amani, R. A. Burke, X. Ji, P. Zhao, D.-H. Lien, P. Taheri, G. H. Ahn, D. Kirya, J. W. Ager, 3rd, E. Yablonovitch, J. Kong, M. Dubey, and A. Javey, "High luminescence efficiency in MoS<sub>2</sub> grown by chemical vapor deposition," *ACS Nano*, vol. 10, pp. 6535–6541, July 2016.
- [170] J. Tang, Z. Wei, Q. Wang, Y. Wang, B. Han, X. Li, B. Huang, M. Liao, J. Liu, N. Li, Y. Zhao, C. Shen, Y. Guo, X. Bai, P. Gao, W. Yang, L. Chen, K. Wu, R. Yang, D. Shi, and G. Zhang, "In situ oxygen doping of monolayer MoS<sub>2</sub> for novel electronics," *Small*, vol. 16, p. e2004276, Oct. 2020.
- [171] S. Mouri, Y. Miyauchi, and K. Matsuda, "Tunable photoluminescence of monolayer MoS<sub>2</sub> via chemical doping," *Nano Lett.*, vol. 13, pp. 5944–5948, Dec. 2013.
- [172] J.-K. Huang, J. Pu, C.-L. Hsu, M.-H. Chiu, Z.-Y. Juang, Y.-H. Chang, W.-H. Chang, Y. Iwasa, T. Takenobu, and L.-J. Li, "Large-area synthesis of highly crystalline WSe<sub>2</sub> monolayers and device applications," *ACS Nano*, vol. 8, pp. 923–930, Jan. 2014.
- [173] M. Bosi, "Growth and synthesis of mono and few-layers transition metal dichalcogenides by vapour techniques: a review," *RSC Advances*, vol. 5, no. 92, pp. 75500–75518, 2015.

- [174] A. Castellanos-Gomez, M. Buscema, R. Molenaar, V. Singh, L. Janssen, H. S. J. van der Zant, and G. A. Steele, "Deterministic transfer of two-dimensional materials by all-dry viscoelastic stamping," *2D Mater.*, vol. 1, p. 011002, Apr. 2014.
- [175] C. M. Efaw, T. da Silva, P. H. Davis, L. Li, E. Graugnard, and M. F. Hurley, "Toward improving ambient volta potential measurements with SKPFM for corrosion studies," *J. Electrochem. Soc.*, vol. 166, p. C3018, Jan. 2019.
- [176] M. DeJarld, P. M. Campbell, A. L. Friedman, M. Currie, R. L. Myers-Ward, A. K. Boyd, S. G. Rosenberg, S. P. Pavunny, K. M. Daniels, and D. K. Gaskill, "Surface potential and thin film quality of low work function metals on epitaxial graphene," *Sci. Rep.*, vol. 8, p. 16487, Nov. 2018.
- [177] N. E. Singh-Miller and N. Marzari, "Surface energies, work functions, and surface relaxations of low-index metallic surfaces from first principles," *Phys. Rev. B Condens. Matter*, vol. 80, p. 235407, Dec. 2009.
- [178] M. von Ardenne, "Das elektronen-rastermikroskop," *Zeitschrift für Physik*, vol. 109, pp. 553–572, Sep 1938.
- [179] G. Y. Liu, S. Xu, and Y. Qian, "Nanofabrication of self-assembled monolayers using scanning probe lithography," *Acc. Chem. Res.*, vol. 33, pp. 457–466, July 2000.
- [180] M. Woodson and J. Liu, "Functional nanostructures from surface chemistry patterning," *Phys. Chem. Chem. Phys.*, vol. 9, pp. 207–225, Jan. 2007.
- [181] L. Netzer and J. Sagiv, "A new approach to construction of artificial monolayer assemblies," *J. Am. Chem. Soc.*, vol. 105, pp. 674–676, Feb. 1983.
- [182] R. G. Nuzzo and D. L. Allara, "Adsorption of bifunctional organic disulfides on gold surfaces," *J. Am. Chem. Soc.*, vol. 105, pp. 4481–4483, June 1983.
- [183] C. D. Bain, E. B. Troughton, Y. T. Tao, J. Evall, G. M. Whitesides, and R. G. Nuzzo, "Formation of monolayer films by the spontaneous assembly of organic thiols from solution onto gold," *J. Am. Chem. Soc.*, vol. 111, pp. 321–335, Jan. 1989.
- [184] L. G. Rosa and J. Liang, "Atomic force microscope nanolithography: dip-pen, nanoshaving, nanografting, tapping mode, electrochemical and thermal nanolithography," *J. Phys. Condens. Matter*, vol. 21, p. 483001, Dec. 2009.
- [185] S. R. Burns, J. M. Gregg, and V. Nagarajan, "Nanostructuring ferroelectrics via focused ion beam methodologies," *Adv. Funct. Mater.*, vol. 26, pp. 8367–8381, Dec. 2016.
- [186] J. J. Steffes, R. A. Ristau, R. Ramesh, and B. D. Huey, "Thickness scaling of ferroelectricity in BiFeO<sub>3</sub> by tomographic atomic force microscopy," *Proc. Natl. Acad. Sci. U. S. A.*, vol. 116, pp. 2413–2418, Feb. 2019.

- [187] H. Han, Y. Kim, M. Alexe, D. Hesse, and W. Lee, "Nanostructured ferroelectrics: fabrication and structure-property relations," *Adv. Mater.*, vol. 23, pp. 4599–4613, Oct. 2011.
- [188] Nina C. Berner, Sinéad Winters, Claudia Backes, Chanyoung Yim, Kim C. Dumbgen, Izabela Kaminska, Sebastian Mackowski, Attilio A. Cafolla, Andreas Hirsch, Georg S. Duesberg, "Understanding and optimising the packing density of perylene bisimide layers on CVD-grown graphene," *Nanoscale*, Nov. 2015.
- [189] Sinéad Winters, Nina C. Berner, Rohit Mishra, Kim C. Dumbgen, Claudia Backes, Martin Hegner, Andreas Hirsch and Georg S. Duesberg, "On-surface derivatisation of aromatic molecules on graphene: the importance of packing density," *ChemComm*, Sept. 2015.
- [190] M. Singh, M. Holzinger, M. Tabrizian, S. Winters, N. C. Berner, S. Cosnier, and G. S. Duesberg, "Noncovalently functionalized monolayer graphene for sensitivity enhancement of surface plasmon resonance immunosensors," *J. Am. Chem. Soc.*, vol. 137, pp. 2800–2803, Mar. 2015.
- [191] F. Würthner, C. R. Saha-Möller, B. Fimmel, S. Ogi, P. Leowanawat, and D. Schmidt, "Perylene bisimide dye assemblies as archetype functional supramolecular materials," *Chem. Rev.*, vol. 116, pp. 962–1052, Feb. 2016.
- [192] P. A. Lewis, *Colored Organic Pigments*. Oxford: Pergamon, 2000.
- [193] M. Marcia, A. Hirsch, and F. Hauke, "Perylene-based non-covalent functionalization of 2D materials," *FlatChem*, vol. 1, pp. 89–103, Jan. 2017.
- [194] H. Huang, S. Chen, X. Gao, W. Chen, and A. T. S. Wee, "Structural and electronic properties of PTCDA thin films on epitaxial graphene," *ACS Nano*, vol. 3, pp. 3431–3436, Nov. 2009.
- [195] K. Peng, H. Zhao, X. Wu, Y. Yuan, and R. Yuan, "Ultrasensitive aptasensor based on graphene-3,4,9,10-perylenetetracarboxylic dianhydride as platform and functionalized hollow PtCo nanochains as enhancers," *Sens. Actuators B Chem.*, vol. 169, pp. 88–95, July 2012.
- [196] C. D. Schmidt, C. Böttcher, and A. Hirsch, "Synthesis and aggregation properties of water-soluble newcome-dendronized perylenetetracarboxdiimides," *European J. Org. Chem.*, vol. 2007, pp. 5497–5505, Nov. 2007.
- [197] C. Wirtz, T. Hallam, C. P. Cullen, N. C. Berner, M. O'Brien, M. Marcia, A. Hirsch, and G. S. Duesberg, "Atomic layer deposition on 2D transition metal chalcogenides: layer dependent reactivity and seeding with organic ad-layers," *Chem. Commun.*, vol. 51, no. 92, pp. 16553–16556, 2015.
- [198] C. Backes, C. D. Schmidt, K. Rosenlehner, F. Hauke, J. N. Coleman, and A. Hirsch, "Nanotube surfactant design: the versatility of water-soluble perylene bisimides," *Adv. Mater.*, vol. 22, pp. 788–802, Feb. 2010.

- [199] N. V. Kozhemyakina, J. M. Englert, G. Yang, E. Spiecker, C. D. Schmidt, F. Hauke, and A. Hirsch, "Non-covalent chemistry of graphene: electronic communication with dendronized perylene bisimides," *Adv. Mater.*, vol. 22, pp. 5483–5487, Dec. 2010.
- [200] G. Abellán, V. Lloret, U. Mundloch, M. Marcia, C. Neiss, A. Görling, M. Varela, F. Hauke, and A. Hirsch, "Noncovalent functionalization of black phosphorus," *Angew. Chem. Int. Ed Engl.*, vol. 55, pp. 14557–14562, Nov. 2016.
- [201] A. Hirsch and F. Hauke, "Post-Graphene 2D chemistry: The emerging field of molybdenum disulfide and black phosphorus functionalization," *Angew. Chem. Int. Ed Engl.*, vol. 57, pp. 4338–4354, Apr. 2018.
- [202] A. Kahn, "Fermi level, work function and vacuum level," *Materials Horizons*, vol. 3, no. 1, pp. 7–10, 2016.
- [203] M. R. Habib, W. Wang, A. Khan, Y. Khan, S. M. Obaidulla, X. Pi, and M. Xu, "Theoretical study of interfacial and electronic properties of transition metal dichalcogenides and organic molecules based van der waals heterostructures," *Adv. Theory Simul.*, vol. 3, p. 2000045, June 2020.
- [204] L. Yan, C. Punckt, I. A. Aksay, W. Mertin, and G. Bacher, "Local voltage drop in a single functionalized graphene sheet characterized by kelvin probe force microscopy," *Nano Lett.*, vol. 11, pp. 3543–3549, Sept. 2011.
- [205] Y. Li, C.-Y. Xu, B.-Y. Zhang, and L. Zhen, "Work function modulation of bilayer MoS<sub>2</sub> nanoflake by backgate electric field effect," *Appl. Phys. Lett.*, vol. 103, p. 033122, July 2013.
- [206] K. P. Puntambekar, P. V. Pesavento, and C. D. Frisbie, "Surface potential profiling and contact resistance measurements on operating pentacene thin-film transistors by kelvin probe force microscopy," *Appl. Phys. Lett.*, vol. 83, pp. 5539–5541, Dec. 2003.
- [207] S. H. Amsterdam, T. J. Marks, and M. C. Hersam, "Leveraging molecular properties to tailor Mixed-Dimensional heterostructures beyond energy level alignment," *J. Phys. Chem. Lett.*, vol. 12, pp. 4543–4557, May 2021.
- [208] M. R. Habib, H. Li, Y. Kong, T. Liang, S. M. Obaidulla, S. Xie, S. Wang, X. Ma, H. Su, and M. Xu, "Tunable photoluminescence in a van der waals heterojunction built from a MoS<sub>2</sub> monolayer and a PTCDA organic semiconductor," *Nanoscale*, vol. 10, pp. 16107–16115, Aug. 2018.
- [209] S. M. Obaidulla, M. R. Habib, Y. Khan, Y. Kong, T. Liang, and M. Xu, "Photoluminescence: MoS<sub>2</sub> and perylene derivative based type-II heterostructure: Bandgap engineering and giant photoluminescence enhancement (adv. mater. interfaces 2/2020)," *Adv. Mater. Interfaces*, vol. 7, p. 2070014, Feb. 2020.

- [210] Y. Shimizu, "Laser interference lithography for fabrication of planar scale gratings for optical metrology," *Nanomanufacturing and Metrology*, vol. 4, pp. 3–27, Mar. 2021.
- [211] F. Li, J. Qi, M. Xu, J. Xiao, Y. Xu, X. Zhang, S. Liu, and Y. Zhang, "Layer dependence and light tuning surface potential of 2D MoS<sub>2</sub> on various substrates," *Small*, vol. 13, Apr. 2017.
- [212] K. H. Kim, K. S. Kim, Y. J. Ji, I. Moon, K. Heo, D.-H. Kang, K. N. Kim, W. J. Yoo, J.-H. Park, and G. Y. Yeom, "Effect of large work function modulation of MoS<sub>2</sub> by controllable chlorine doping using a remote plasma," *J. Mater. Chem.*, vol. 8, pp. 1846–1851, Feb. 2020.
- [213] J. C. Rubim and R. F. Aroca, "The observation of high order overtones and combinations in the SERRS spectra of a perylene dye spin coated onto silver island films," *Phys. Chem. Chem. Phys.*, vol. 10, pp. 5412–5418, Sept. 2008.
- [214] N. Chiang, N. Jiang, L. R. Madison, E. A. Pozzi, M. R. Wasielewski, M. A. Ratner, M. C. Hersam, T. Seideman, G. C. Schatz, and R. P. Van Duyne, "Probing intermolecular vibrational symmetry breaking in self-assembled monolayers with ultrahigh vacuum tip-enhanced raman spectroscopy," *J. Am. Chem. Soc.*, vol. 139, pp. 18664–18669, Dec. 2017.
- [215] K. F. Mak, K. He, C. Lee, G. H. Lee, J. Hone, T. F. Heinz, and J. Shan, "Tightly bound trions in monolayer MoS<sub>2</sub>," *Nat. Mater.*, vol. 12, pp. 207–211, Mar. 2013.
- [216] A. Michail, D. Anastopoulos, N. Delikoukos, J. Parthenios, S. Grammatikopoulos, S. A. Tsirkas, N. N. Lathiotakis, O. Frank, K. Filintoglou, and K. Papagelis, "Biaxial strain engineering of CVD and exfoliated single- and bi-layer MoS<sub>2</sub> crystals," *2D Mater.*, vol. 8, p. 015023, Nov. 2020.
- [217] A. Steinhoff, J.-H. Kim, F. Jahnke, M. Rösner, D.-S. Kim, C. Lee, G. H. Han, M. S. Jeong, T. O. Wehling, and C. Gies, "Efficient excitonic photoluminescence in direct and indirect band gap monolayer MoS<sub>2</sub>," *Nano Lett.*, vol. 15, pp. 6841–6847, Oct. 2015.
- [218] H. Nan, Z. Wang, W. Wang, Z. Liang, Y. Lu, Q. Chen, D. He, P. Tan, F. Miao, X. Wang, J. Wang, and Z. Ni, "Strong photoluminescence enhancement of MoS(2) through defect engineering and oxygen bonding," *ACS Nano*, vol. 8, pp. 5738–5745, June 2014.
- [219] S. Park, N. Mutz, S. A. Kovalenko, T. Schultz, D. Shin, A. Aljarb, L.-J. Li, V. Tung, P. Amsalem, E. J. W. List-Kratochvil, J. Stähler, X. Xu, S. Blumstengel, and N. Koch, "Type-I energy level alignment at the PTCDA-Monolayer MoS<sub>2</sub> interface promotes resonance energy transfer and luminescence enhancement," *Adv. Sci.*, vol. 8, p. 2100215, June 2021.
- [220] C. Muccianti, S. L. Zachritz, A. Garland, C. N. Eads, B. H. Badada, A. Alfrey, M. R. Koehler, D. G. Mandrus, R. Binder, B. J. LeRoy, O. L. A. Monti, and J. R. Schaibley, "Coupled 2D Semiconductor–Molecular excitons with enhanced raman scattering," *J. Phys. Chem. C*, vol. 124, pp. 27637–27644, Dec. 2020.

- [221] B. G. Bush, F. W. DelRio, J. Opatkiewicz, R. Maboudian, and C. Carraro, "Effect of formation temperature and roughness on surface potential of octadecyltrichlorosilane self-assembled monolayer on silicon surfaces," *J. Phys. Chem. A*, vol. 111, pp. 12339–12343, Dec. 2007.
- [222] T. C. Leung, C. L. Kao, W. S. Su, Y. J. Feng, and C. T. Chan, "Relationship between surface dipole, work function and charge transfer: Some exceptions to an established rule," *Phys. Rev. B Condens. Matter*, vol. 68, p. 195408, Nov. 2003.
- [223] R. Schlesinger, Y. Xu, O. T. Hofmann, S. Winkler, J. Frisch, J. Niederhausen, A. Vollmer, S. Blumstengel, F. Henneberger, P. Rinke, M. Scheffler, and N. Koch, "Controlling the work function of ZnO and the energy-level alignment at the interface to organic semiconductors with a molecular electron acceptor," *Phys. Rev. B Condens. Matter*, vol. 87, p. 155311, Apr. 2013.
- [224] Z. Zhang and J. T. Yates, Jr, "Band bending in semiconductors: chemical and physical consequences at surfaces and interfaces," *Chem. Rev.*, vol. 112, pp. 5520–5551, Oct. 2012.
- [225] S. Choi, Z. Shaolin, and W. Yang, "Layer-number-dependent work function of MoS<sub>2</sub> nanoflakes," *J. Korean Phys. Soc.*, vol. 64, pp. 1550–1555, May 2014.
- [226] M. Tamulewicz, J. Kutrowska-Girzycka, K. Gajewski, J. Serafińczuk, A. Sierakowski, J. Jadczyk, L. Bryja, and T. P. Gotszalk, "Layer number dependence of the work function and optical properties of single and few layers MoS<sub>2</sub>: effect of substrate," *Nanotechnology*, vol. 30, p. 245708, June 2019.
- [227] X. Wang, J. Dan, Z. Hu, J. F. Leong, Q. Zhang, Z. Qin, S. Li, J. Lu, S. J. Pennycook, W. Sun, and C. H. Sow, "Defect heterogeneity in monolayer WS<sub>2</sub> unveiled by work function variance," *Chem. Mater.*, vol. 31, pp. 7970–7978, Oct. 2019.
- [228] V. Kaushik, M. Ahmad, K. Agarwal, D. Varandani, B. D. Belle, P. Das, and B. R. Mehta, "Charge transport in 2D MoS<sub>2</sub>, WS<sub>2</sub>, and MoS<sub>2</sub>–WS<sub>2</sub> Heterojunction-Based Field-Effect transistors: Role of ambipolarity," *J. Phys. Chem. C*, vol. 124, pp. 23368–23379, Oct. 2020.
- [229] I. Sharma and B. R. Mehta, "KPFM and CAFM based studies of MoS<sub>2</sub> (2D)/WS<sub>2</sub> heterojunction patterns fabricated using stencil mask lithography technique," *J. Alloys Compd.*, vol. 723, pp. 50–57, Nov. 2017.
- [230] H. Fang, S. Chuang, T. C. Chang, K. Takei, T. Takahashi, and A. Javey, "High-Performance single layered WSe<sub>2</sub> p-FETs with chemically doped contacts," *Nano Lett.*, vol. 12, pp. 3788–3792, July 2012.
- [231] L. Ansari, S. Monaghan, N. McEvoy, C. Ó. Coileáin, C. P. Cullen, J. Lin, R. Siris, T. Stimpel-Lindner, K. F. Burke, G. Mirabelli, R. Duffy, E. Caruso, R. E. Nagle, G. S. Duesberg, P. K. Hurley, and F. Gity, "Quantum confinement-induced semimetal-to-semiconductor evolution

- in large-area ultra-thin PtSe<sub>2</sub> films grown at 400 °C,” *npj 2D Materials and Applications*, vol. 3, p. 33, Sept. 2019.
- [232] Y. Wang, L. Li, W. Yao, S. Song, J. T. Sun, J. Pan, X. Ren, C. Li, E. Okunishi, Y.-Q. Wang, E. Wang, Y. Shao, Y. Y. Zhang, H.-T. Yang, E. F. Schwier, H. Iwasawa, K. Shimada, M. Taniguchi, Z. Cheng, S. Zhou, S. Du, S. J. Pennycook, S. T. Pantelides, and H.-J. Gao, “Monolayer PtSe<sub>2</sub>, a new semiconducting Transition-Metal-Dichalcogenide, epitaxially grown by direct selenization of Pt,” *Nano Lett.*, vol. 15, pp. 4013–4018, June 2015.
- [233] Z. Wang, Q. Li, F. Besenbacher, and M. Dong, “Facile synthesis of single crystal PtSe<sub>2</sub> nanosheets for nanoscale electronics,” *Adv. Mater.*, vol. 28, pp. 10224–10229, Dec. 2016.
- [234] X. Chia, A. Adriano, P. Lazar, Z. Sofer, J. Luxa, and M. Pumera, “Layered platinum dichalcogenides (PtS<sub>2</sub>, PtSe<sub>2</sub>, and PtTe<sub>2</sub>) electrocatalysis: Monotonic dependence on the chalcogen size,” *Adv. Funct. Mater.*, vol. 26, pp. 4306–4318, June 2016.
- [235] B. M. Szydłowska, O. Hartwig, B. Tywoniuk, T. Hartman, T. Stimpel-Lindner, Z. Sofer, N. McEvoy, G. S. Duesberg, and C. Backes, “Spectroscopic thickness and quality metrics for PtSe<sub>2</sub> layers produced by top-down and bottom-up techniques,” *2D Mater.*, vol. 7, p. 045027, Sept. 2020.
- [236] W. Zhang, J. Qin, Z. Huang, and W. Zhang, “The mechanism of layer number and strain dependent bandgap of 2D crystal PtSe<sub>2</sub>,” *J. Appl. Phys.*, vol. 122, p. 205701, Nov. 2017.
- [237] B. Cao, Z. Ye, L. Yang, L. Gou, and Z. Wang, “Recent progress in van der waals 2D PtSe<sub>2</sub>,” *Nanotechnology*, vol. 32, July 2021.
- [238] R. Kempt, A. Kuc, and T. Heine, “Two-Dimensional Noble-Metal chalcogenides and phosphochalcogenides,” *Angew. Chem. Int. Ed Engl.*, vol. 59, pp. 9242–9254, June 2020.
- [239] H. Xu, H. Zhang, Y. Liu, S. Zhang, Y. Sun, Z. Guo, Y. Sheng, X. Wang, C. Luo, X. Wu, J. Wang, W. Hu, Z. Xu, Q. Sun, P. Zhou, J. Shi, Z. Sun, D. W. Zhang, and W. Bao, “Controlled doping of wafer-scale PtSe<sub>2</sub> films for device application,” *Adv. Funct. Mater.*, vol. 29, p. 1805614, Jan. 2019.
- [240] H. Zheng, Y. Choi, F. Baniasadi, D. Hu, L. Jiao, K. Park, and C. Tao, “Visualization of point defects in ultrathin layered 1T-PtSe<sub>2</sub>,” *2D Mater.*, vol. 6, p. 041005, Sept. 2019.
- [241] P. Li, L. Li, and X. C. Zeng, “Tuning the electronic properties of monolayer and bilayer PtSe<sub>2</sub> via strain engineering,” *J. Mater. Chem.*, vol. 4, pp. 3106–3112, Apr. 2016.
- [242] S. Deng, L. Li, and Y. Zhang, “Strain modulated electronic, mechanical, and optical properties of the monolayer PdS<sub>2</sub>, PdSe<sub>2</sub>, and PtSe<sub>2</sub> for tunable devices,” *ACS Appl. Nano Mater.*, vol. 1, pp. 1932–1939, Apr. 2018.

- [243] C. Yim, N. McEvoy, S. Riazimehr, D. S. Schneider, F. Gity, S. Monaghan, P. K. Hurley, M. C. Lemme, and G. S. Duesberg, “Wide spectral photoresponse of layered platinum diselenide-based photodiodes,” *Nano Lett.*, vol. 18, pp. 1794–1800, Mar. 2018.
- [244] L. Zeng, S. Lin, Z. Lou, H. Yuan, H. Long, Y. Li, W. Lu, S. P. Lau, D. Wu, and Y. H. Tsang, “Ultrafast and sensitive photodetector based on a PtSe<sub>2</sub>/silicon nanowire array heterojunction with a multiband spectral response from 200 to 1550 nm,” *NPG Asia Materials*, vol. 10, pp. 352–362, Apr. 2018.
- [245] H. L. Zhuang and R. G. Hennig, “Computational search for Single-Layer Transition-Metal dichalcogenide photocatalysts,” *J. Phys. Chem. C*, vol. 117, pp. 20440–20445, Oct. 2013.
- [246] D. Hu, T. Zhao, X. Ping, H. Zheng, L. Xing, X. Liu, J. Zheng, L. Sun, L. Gu, C. Tao, D. Wang, and L. Jiao, “Unveiling the Layer-Dependent catalytic activity of PtSe<sub>2</sub> atomic crystals for the hydrogen evolution reaction,” *Angew. Chem. Int. Ed.*, vol. 58, pp. 6977–6981, May 2019.
- [247] S. Wagner, C. Yim, N. McEvoy, S. Kataria, V. Yokaribas, A. Kuc, S. Pindl, C.-P. Fritzen, T. Heine, G. S. Duesberg, and M. C. Lemme, “Highly sensitive electromechanical piezoresistive pressure sensors based on Large-Area layered PtSe<sub>2</sub> films,” *Nano Lett.*, vol. 18, pp. 3738–3745, June 2018.
- [248] C. S. Boland, C. Ó. Coileáin, S. Wagner, J. B. McManus, C. P. Cullen, M. C. Lemme, G. S. Duesberg, and N. McEvoy, “PtSe<sub>2</sub> grown directly on polymer foil for use as a robust piezoresistive sensor,” *2d Mater.*, vol. 6, p. 045029, Aug. 2019.
- [249] L. Pi, L. Li, K. Liu, Q. Zhang, H. Li, and T. Zhai, “Recent progress on 2D Noble-Transition-Metal dichalcogenides,” *Adv. Funct. Mater.*, vol. 1, p. 1904932, Oct. 2019.
- [250] M. Velický, G. E. Donnelly, W. R. Hendren, S. McFarland, D. Scullion, W. J. I. DeBenedetti, G. C. Correa, Y. Han, A. J. Wain, M. A. Hines, D. A. Muller, K. S. Novoselov, H. D. Abruña, R. M. Bowman, E. J. G. Santos, and F. Huang, “Mechanism of Gold-Assisted exfoliation of Centimeter-Sized Transition-Metal dichalcogenide monolayers,” *ACS Nano*, vol. 12, pp. 10463–10472, Oct. 2018.
- [251] B. Huang, L. Du, Q. Yi, L. Yang, J. Li, L. Miao, C. Zhao, and S. Wen, “Bulk-structured PtSe<sub>2</sub> for femtosecond fiber laser mode-locking,” *Opt. Express*, vol. 27, pp. 2604–2611, Feb. 2019.
- [252] Y. Huang, Y.-H. Pan, R. Yang, L.-H. Bao, L. Meng, H.-L. Luo, Y.-Q. Cai, G.-D. Liu, W.-J. Zhao, Z. Zhou, L.-M. Wu, Z.-L. Zhu, M. Huang, L.-W. Liu, L. Liu, P. Cheng, K.-H. Wu, S.-B. Tian, C.-Z. Gu, Y.-G. Shi, Y.-F. Guo, Z. G. Cheng, J.-P. Hu, L. Zhao, G.-H. Yang, E. Sutter, P. Sutter, Y.-L. Wang, W. Ji, X.-J. Zhou, and H.-J. Gao, “Universal mechanical exfoliation of large-area 2D crystals,” *Nat. Commun.*, vol. 11, p. 2453, May 2020.



- [253] G. Wang, K. Wang, N. McEvoy, Z. Bai, C. P. Cullen, C. N. Murphy, J. B. McManus, J. J. Magan, C. M. Smith, G. S. Duesberg, I. Kaminer, J. Wang, and W. J. Blau, "Ultrafast carrier dynamics and bandgap renormalization in layered PtSe<sub>2</sub>," *Small*, vol. 15, p. e1902728, Aug. 2019.
- [254] W. Jiang, X. Wang, Y. Chen, G. Wu, K. Ba, N. Xuan, Y. Sun, P. Gong, J. Bao, H. Shen, T. Lin, X. Meng, J. Wang, and Z. Sun, "Large-area high quality PtSe<sub>2</sub> thin film with versatile polarity," *InfoMat*, May 2019.
- [255] S. S. Han, J. H. Kim, C. Noh, J. H. Kim, E. Ji, J. Kwon, S. M. Yu, T.-J. Ko, E. Okogbue, K. H. Oh, H.-S. Chung, Y. Jung, G.-H. Lee, and Y. Jung, "Horizontal-to-Vertical transition of 2D layer orientation in Low-Temperature chemical vapor Deposition-Grown PtSe<sub>2</sub> and its influences on electrical properties and device applications," *ACS Appl. Mater. Interfaces*, vol. 11, pp. 13598–13607, Apr. 2019.
- [256] X. Yu, P. Yu, D. Wu, B. Singh, Q. Zeng, H. Lin, W. Zhou, J. Lin, K. Suenaga, and et al., "Atomically thin noble metal dichalcogenide: a broadband mid-infrared semiconductor," *Nature Communications*, vol. 9, Apr 2018.
- [257] J. Shi, Y. Huan, M. Hong, R. Xu, P. Yang, Z. Zhang, X. Zou, and Y. Zhang, "Chemical vapor deposition grown Large-Scale atomically thin platinum diselenide with Semimetal-Semiconductor transition," *ACS Nano*, June 2019.
- [258] J. Xie, D. Zhang, X.-Q. Yan, M. Ren, X. Zhao, F. Liu, R. Sun, X. Li, Z. Li, S. Chen, Z.-B. Liu, and J.-G. Tian, "Optical properties of chemical vapor deposition-grown PtSe<sub>2</sub> characterized by spectroscopic ellipsometry," *2D Mater.*, vol. 6, p. 035011, Apr. 2019.
- [259] M. Hilde, K. Wang, and R. Engel-Herbert, "Growth of ultrathin pt layers and selenization into PtSe<sub>2</sub> by molecular beam epitaxy," *2D Mater.*, June 2020.
- [260] Y. Yan, Y. Sun, J. Li, Z. Hu, and X. Zhao, "Controlled nanodot fabrication by rippling polycarbonate surface using an AFM diamond tip," *Nanoscale Res. Lett.*, vol. 9, p. 372, July 2014.
- [261] U. Celano, F.-C. Hsia, D. Vanhaeren, K. Paredis, T. E. M. Nordling, J. G. Buijnsters, T. Hantschel, and W. Vandervorst, "Mesoscopic physical removal of material using sliding nano-diamond contacts," *Sci. Rep.*, vol. 8, p. 2994, Feb. 2018.
- [262] M. Fazeli Jadidi, H. Ö. Özer, S. Goel, J. I. Kilpatrick, N. McEvoy, D. McCloskey, J. F. Donegan, and G. L. W. Cross, "Distribution of shallow NV centers in diamond revealed by photoluminescence spectroscopy and nanomachining," *Carbon N. Y.*, vol. 167, pp. 114–121, Oct. 2020.

- [263] R. Kappera, D. Voiry, S. E. Yalcin, B. Branch, G. Gupta, A. D. Mohite, and M. Chhowalla, “Phase-engineered low-resistance contacts for ultrathin mos<sub>2</sub> transistors,” *Nature Materials*, vol. 13, pp. 1128–1134, Aug 2014.
- [264] H. Akazawa, “Highly adhesive pt-electrode films directly deposited on SiO<sub>2</sub> by electron-cyclotron-resonance plasma sputtering,” *Surf. Coat. Technol.*, vol. 204, pp. 1836–1841, Feb. 2010.
- [265] V. Guarnieri, L. Biazzi, R. Marchiori, and A. Lago, “Platinum metallization for MEMS application. focus on coating adhesion for biomedical applications,” *Biomatter*, vol. 4, 2014.
- [266] S. Lin, Y. Liu, Z. Hu, W. Lu, C. H. Mak, L. Zeng, J. Zhao, Y. Li, and et al., “Tunable active edge sites in PtSe<sub>2</sub> films towards hydrogen evolution reaction,” *Nano Energy*, vol. 42, pp. 26–33, Dec. 2017.
- [267] O. Yıldırım, A. Borzi, C. V. Falub, H. Rohrmann, D. Jaeger, M. Rechsteiner, D. Schneider, A. Neels, H. J. Hug, and M. A. Marioni, “Tuning the microstructure of the pt layers grown on Al<sub>2</sub>O<sub>3</sub> (0001) by different sputtering methods,” *Scr. Mater.*, vol. 194, p. 113689, Mar. 2021.
- [268] K. Itaya, S. Sugawara, K. Sashikata, and N. Furuya, “In situ scanning tunneling microscopy of platinum (111) surface with the observation of monatomic steps,” *J. Vac. Sci. Technol. A*, vol. 8, pp. 515–519, Jan. 1990.
- [269] C. Lee, H. Yan, L. E. Brus, T. F. Heinz, J. Hone, and S. Ryu, “Anomalous lattice vibrations of single- and few-layer MoS<sub>2</sub>,” *ACS Nano*, vol. 4, pp. 2695–2700, May 2010.
- [270] J. Du, P. Song, F. L., and et al., “Elastic, electronic and optical properties of the two-dimensional ptx<sub>2</sub> (x = s, se, and te) monolayer,” *Applied Surface Science*, vol. 435, pp. 476–482, 2018.
- [271] Z.-Q. Xu, Y. Zhang, Z. Wang, Y. Shen, W. Huang, X. Xia, W. Yu, Y. Xue, L. Sun, C. Zheng, Y. Lu, L. Liao, and Q. Bao, “Atomically thin lateral p–n junction photodetector with large effective detection area,” *2D Mater.*, vol. 3, p. 041001, Sept. 2016.
- [272] K. Chen, X. Wan, J. Wen, W. Xie, Z. Kang, X. Zeng, H. Chen, and J.-B. Xu, “Electronic properties of MoS<sub>2</sub>-WS<sub>2</sub> heterostructures synthesized with Two-Step lateral epitaxial strategy,” *ACS Nano*, vol. 9, pp. 9868–9876, Oct. 2015.
- [273] F. R. Braakman, P. Barthelemy, C. Reichl, W. Wegscheider, and L. M. K. Vandersypen, “Long-distance coherent coupling in a quantum dot array,” *Nat. Nanotechnol.*, vol. 8, pp. 432–437, June 2013.